Seminar

Space Plasma Physics

Chairmen:

Prof. Adam Yukhimuk (MAO NASU, Ukraine)
Prof. Roman Kostik (MAO NASU, Ukraine)

GRANULATION and FIVE–MINUTE OSCILLATIONS

E. V. Khomenko, R. I. Kostik, and N. G. Shchukina

Main Astronomical Observatory, NAS of Ukraine
27 Zabolotnoho St., 03680 Kyiv, Ukraine
e-mail: kostik@mao.kiev.ua

We discuss the links between the photospheric 5–min oscillations and granulation patterns using a 30-min time series of CCD spectral images of solar granulation recorded with high spatial ($0.''5$) and temporal (9.3 s) resolution. The observed images contain Fe I 5324 Å line. Our observations and theoretical modeling lead to the similar results: (i) period of oscillations varies above granules and lanes; (ii) amplitudes of the velocity oscillations grow with the contrast of granulation. Amplitudes of the intensity oscillations are larger in intergranular lanes than in granules. Our simple model describes the basic features of the oscillations above granules and intergranular lanes. We conclude that differences in these oscillations are caused mainly by variations of the physical conditions in these structures.

INTRODUCTION

Spatial relation between the 5–min oscillations and granulation patterns is much debated in the literature. Most support theoretical suggestions made by Goldreich, Keeley, Kumar, and Murray [5]–[7], [14] that acoustic waves which comprise the observed 5–min oscillations are stochastically generated by turbulent convection just beneath the photosphere. Moreover, Brown [3] predicted that the most of the acoustic emission should come from rare localized events, where convective velocities are the highest. Goode, Gough, and Kosovichev [8] associate these localized events with expanding overshooting granules.

Recent study of the spatial relation between the solar granulation and the 5–min oscillations completed by Espagnet *et al.* [4] confirms that the strong oscillations are well isolated temporally and spatially. However, the most energetic oscillations turned out to occur only in expanding intergranular spaces with the strong downflows. This conclusion disagrees with the picture in which the oscillations are excited by expanding overshooting granules. On the other hand, analyzing G-band granulation filtergrams Hoekzema *et al.* [9]–[11] have deduced "that the photospheric 5–min oscillations are primarily global and rather insensitive to the local fine structure".

We conclude that despite considerable efforts by various researchers the issue of the links between the 5–min oscillations and granulation remains open.

OBSERVATIONS AND DATA REDUCTION

The observations were carried out with the 70-cm German Vacuum Tower Telescope at the Observatorio del Teide, Tenerife, in August 1996. The telescope and spectrograph are described by Schröter *et al.* [21]. The CCD images contain the photospheric Fe I 5324 Å line. The observed area was placed near the quiet solar disk centre. Magnetically active regions were avoided by controlling the entrance slit position using H_α and Ca II K slit–jaw images. We used CCD camera with 1024×1024 pixels, in 2×2 binning mode. A pixel size in this mode was 0.174 arcsec in the spatial direction. The dispersion of the spectra was of about 0.10 Å/mm at 6000 Å. The entrance slit width of the spectrograph was set to 80 μm, *i.e.*, 0.38 arcsec on the solar disk. Thus, each overall image corresponds to an area on the solar surface of about 0.38×89 arcsec^2. The Fe I 5324 line spectrograms were taken every 9.3 s with integration time 5.7 s. The time series covered about 31 minutes and included 200 images in total.

The reduction of CCD images followed the standard procedure. For each averaged spectral pixel row i ($i = 1 - 170$) of each image j ($j = 1 - 200$) we inferred intensity and velocity signals at 11 levels of the line profile $\delta I_l(i,j)$, (l = 0 − 10) and $\delta V_l(i,j)$, (l = 0 − 10), where $l = 0$ corresponds to the line core. The procedure was performed applying the method described by Stebbins and Goode [23].

Invited paper.

The variations in the line parameters under study are induced mainly by convective and wave motions. In order to separate granular and oscillatory components of the velocity field we constructed a diagnostic $k - \omega$ diagram.

RESULTS AND DISCUSSION

"Artificial granule", power–contrast diagram

One of the ways to investigate the links between the 5–min oscillations and granulation is to isolate an individual granule and intergranular lane and then to observe the evolution of oscillations above them. However, there are two problems:

- How to identify the same granulation structure during its lifetime?
- How to apply the methods of spectral analysis to such a short time series (granular mean lifetime is ~ 10 min according to Title *et al.* [24]?

To overcome the problem we constructed an "artificial" spectrum of granule and intergranular lane and followed its evolution in time (the method firstly applied by Kostik and Shchukina [12]). According to this approach we splitted spectral rows of each image into granular and intergranular ones using the spatially and temporally averaged continuum intensity $\bar{I}_c$ as the criterion. Having averaged separately the spectra of the rows with positive and negative contrast in each image we obtained two time sequences, one of which contained only the averaged granule spectra and the other – the averaged intergranular spectra. Following that way we introduced more refined classification of the continuum contrast differences. The bright and dark samples were splitted further into 6 contrast classes by combining the rows in the same class if its contrast exceeded some threshold. We used thresholds for the granular rows in the range $1 - 5.5\%$ and for the intergranular ones in the range from -1% to -5%.

Figure 1 displays the power–contrast $(P - I)$ diagram for the "artificial" granular pattern. Left-hand side panels in Fig. 1 represent observational results while right-hand side ones represent simulations. We will discuss the simulations in the next Subsection. Now we refer only to observations. In the diagram, the power of the central residual intensity δI_{0W} (panel a) and velocity δV_{0W} (panel c) oscillations are plotted against the normalized continuum contrast δI_c. In our observations the greatest power concentrates at two frequencies: $\omega = 3.73 \pm 0.26$ and $\omega = 3.21 \pm 0.26$ mHz (the periods are equal to 268 and 312 s, respectively). At the period $T = 268$ s there is much more power of velocity oscillations in the negative range of contrast than in the positive one. Contrary to that, at the period $T = 312$ s the power is distributed over the whole range of granulation contrast, but there is less power in the negative range. Around this period the power increases with absolute value of the contrast: strong velocity oscillations occur preferentially above the brightest granules (where the power is the maximum) and above the darkest intergranular lanes. Thus, we conclude that the powerful velocity oscillations may be found above granules as well as above intergranular lanes, but with different periods. These results disagree with Espagnet *et al.* [4] who argue that the most energetic velocity oscillations occur only above intergranules.

The power of the intensity oscillations δI_{0W} has another distribution (Fig. 1c). It increases with contrast both above granules and intergranules but the most energetic intensity oscillations are present only above intergranules. This is correct for oscillations with 268 and 312 s periods. Unfortunately, we cannot compare these results with those of Espagnet *et al.* [4] because the authors do not provide the corresponding data.

Simulation of the wave propagation in the photosphere

It seems natural that oscillations above granules and intergranular lanes are not identical because the physical conditions in these regions vary a lot. Even under assumption that oscillations at the bottom are generated with equal amplitudes, dissimilarities should occur at the top of the photosphere if they propagate through a considerably different media such as granules and intergranular lanes. Firstly, temperature is not the same in granules and intergranules. Intergranules have less steep temperature gradient and are cooler in the deeper layers, while granules become cooler in the upper layers of the atmosphere. This conclusion is supported by numerous observational studies among of which are the recent results by Rodríguez Hidalgo *et al.* [17], who applied an inversion code to high quality two-dimensional spectroscopic data and extracted information about temperature and other parameters of granular/intergranular atmospheres. Theoretical simulations of solar granulation also demonstrate the same tendency (see for example the paper by Asplund *et al.* [1]). Temperature variations act on the radiative relaxation time. The oscillations are very sensitive to the latter. Changes in temperature also modify the acoustic cut-off frequency under which the oscillations are actively damped. Secondly, differences in pressure and density affect the scale height to which an oscillatory amplitude is sensitive. And the least but not the last, oscillations propagate in a moving medium with upflows, downflows and horizontal flows. This should modify their propagation frequency and affect the phase shifts simply because of the Doppler effect.

Regarding to the aforementioned considerations, we found it reasonable to reconsider the theory of wave propagation in the solar atmosphere and to pay more attention to the effect of oscillations on a line profile. The main difference between our work and similar studies of other authors (*e.g.*, [2, 15, 16] and references therein) is that we considered wave propagation in a moving medium. In all the cited papers, the granulation component of the velocity field was neglected and only oscillatory perturbations were considered. In the present study we make an attempt to include both velocity components.

A comprehensive analysis of the propagation of the acoustic-gravity waves in a radiating fluid is fulfilled by Mihalas and Mihalas [18]. We follow this analysis and the scheme given by Noyes and Leighton [19] and then developed by Kostik [13] and Schmieder [20]. We solved analytically the hydrodynamical equations of mass, momentum and energy conservation:

$$\rho\frac{d\vec{V}}{dt} = -\vec{\nabla}P + \vec{g}\rho\,; \tag{1}$$

$$\frac{\partial\rho}{\partial t} = -\vec{\nabla}(\rho\vec{V}); \tag{2}$$

$$\frac{dQ}{dt} = c_v\frac{dT}{dt} - \frac{RT}{\rho}\frac{d\rho}{dt}, \tag{3}$$

where d/dt is the Stokes derivative, dQ/dt is the net rate of radiative energy input (per unit volume) to the gas from external sources; other notations are standard. We assumed that there are no magnetic field; viscosity and thermal conduction terms can be omitted; the effects of solar rotation are negligible; to the 0^{th} order, the atmosphere is plane parallel, horizontally homogeneous and in radiative equilibrium. The matter is described by a suitable equation of state (no effects of ionization are considered):

$$\frac{T_1}{T_0} = \frac{P_1}{P_0} - \frac{\rho_1}{\rho_0}. \tag{4}$$

The effects of radiative relaxation, the main source of dissipation for linear waves in the solar photosphere, is taken into account by using the Newtonian cooling approximation. The motion is restricted to one dimension, hence, internal gravity waves are excluded from consideration. Solution of the system of partial differential equations was obtained by approximating the atmosphere as a series of isothermal layers each of a given thickness (10 km) moving with a constant velocity. In each layer we linearized the fundamental equations with:

$$T = T_0 + T_1, \quad P = P_0 + P_1, \quad \rho = \rho_0 + \rho_1, \quad V = V_0 + V_1. \tag{5}$$

The dimensionless and linearized equations then become (to the 1^{st} order):

$$\frac{\partial W_1}{\partial t} + W_0\frac{\partial W_1}{\partial z} = -\frac{\partial}{\partial z}(R+\Theta) + 2\Theta\,; \tag{6}$$

$$\frac{\partial R}{\partial t} + W_0\frac{\partial R}{\partial z} = 2W_0R - \frac{\partial W_1}{\partial z} + 2W_1; \tag{7}$$

$$\frac{\partial\Theta}{\partial t} + W_0\frac{\partial\Theta}{\partial z} = -\frac{1}{\tau_{RR}}\Theta - (\gamma-1)\frac{\partial W_1}{\partial z}. \tag{8}$$

Here the vertical velocity W is measured in a units of acoustic velocity ($W_{0,1} = V_{0,1}/C_s$), values $\Theta = T_1/T_0$ and $R = \rho_1/\rho_0$ – in a units of the corresponding unperturbed values, distance $z = \tilde{z}/2H$ – in a units of the doubled pressure scale height $H^{-1} = -\nabla P/P$ at the given layer. The system has an exponential solution at the fixed frequency of the form:

$$W_1,\,\Theta,\,R \sim e^{z(1-k_i)}e^{-ik_r(tV_{ph}-tW_0-z)}, \tag{9}$$

where $V_{ph} = \omega/k_r$ is a phase velocity of the wave, k_r and k_i are the real and imaginary parts of the vertical wave number k_z. Only upward modes can be excited in an isothermal atmosphere perturbed from below; therefore, by selecting an upward solution of the Eqs. (6)–(8), the vertical velocity can be written as follows:

$$W_1 = V_{0w}e^{z(1-k_i)}\sin((\omega - W_0k_r)t - k_rz). \tag{10}$$

The corresponding waveform for the thermodynamic perturbations T_1/T_0 and ρ_1/ρ_0 were obtained from the polarization relations and the pressure perturbations was found from the equation of state (see Eq. (4)):

$$\frac{T_1}{T_0} = |\Theta| e^{z(1-k_i)} \sin((\omega - W_0 k_r)t - k_r z + \phi_{TV}), \tag{11}$$

$$\frac{\rho_1}{\rho_0} = |R| e^{z(1-k_i)} \sin((\omega - W_0 k_r)t - k_r z + \phi_{\rho V}). \tag{12}$$

Variations of the thermodynamical quantities (see Eqs. (10)–(12)) were introduced in the model atmosphere and then profiles of the Fe I 5324 Å line were synthesized.

Note that positive direction of the vertical axis z in our study was chosen toward to the centre on the Sun, thus, waves moving toward the observer have negative velocity. Note also that since we have a non-zero vertical velocity field, the effective frequency which we can measure is not constant now, but is modified by velocity:

$$\tilde{\omega} = \omega - W_0 k_r. \tag{13}$$

To study peculiarities of the wave propagation above granules and intergranular lanes an appropriate model atmosphere is desired. In the present study we utilized a snapshot of the 3D model atmosphere from the most recent numerical simulations by Asplund *et al.* [1]. We used simulations with resolution of $50 \times 50 \times 82$ grid-points corresponding to the physical dimension of $6.0 \times 6.0 \times 3.8$ Mm with nearly 1.0 Mm being located above the continuum optical depth unity. The simulated box includes about 15 granules. We considered the 3D snapshot as a set of 1D granular/intergranular model atmospheres. For the line profiles calculations we randomly chose a slice from the snapshot which contains 5 granules separated by intergranular lanes.

For each such a model we computed the line intensity using the formal solution of the time–dependent radiative transfer equation for the case of the moving atmosphere perturbed by oscillations. We used as input in formal radiative transfer solution NLTE departure coefficients found from the self–consistent solution of the kinetic and radiative transfer equations for the realistic iron atomic model and unperturbed granulation models. We assume that perturbations caused by wave in the atmosphere are small enough so the departure coefficients do not change in the perturbed model atmosphere. All details of our NLTE computations are described by Shchukina and Trujillo Bueno [22]. Time series of 40 profiles with the real time step of 9.3 sec, close to the observed value, were synthesized in each of the 50 models. The overall time of computations was about 1 wave period ($\sim$ 5 minutes). Initial amplitude of the wave perturbation was chosen equal to $V_0 = 100$ m s^{-1}, and two sets of the profiles were calculated, one with the initial period of the wave 312 s and another with 268 s. The value $V_0 = 100$ m s^{-1} was taken from our observations of the spatially averaged oscillations at height $H = 0$ km. We solved an inverse problem and restored oscillations of intensity and velocity at 11 levels of the computed line profiles applying the same method as for the observational data.

Figure 1b and 1d represent the $P - I$ diagram, computed using theoretical profiles. As before we separated profiles into 14 contrast classes and ascribed profile to a certain class if its continuum contrast has been higher (for granules) or lower (for lanes) than some threshold. Curves for two initial periods ($T = 268$ and 312 s) are shown.

In general, theoretical $P - I$ diagram resembles the main features of the observed diagram. This supports the conclusion by Kostik and Shchukina [12] showing that observed increase of power of oscillations above the most contrast space is not an artifact due to averaging of the spectral profiles over areas of different size, but is a real effect. We see that theory also gives a rapid increase of power of oscillations above intergranular lanes, both for intensity and, in a less degree for velocity. Above granules there are much less power for both periods of oscillations. The difference in power between two periods (268 and 312) is more or less the same both in observations and theory: oscillations with period 268 s are more powerful.

Nevertheless, there is an important difference between observed and simulated $P - I$ diagram. Observed oscillations above the low-contrast space have a very little power, it is nearly zero for period 312 s, while simulated oscillations do not exhibit the tendency.

Another important discrepancy is the rapid increase of the velocity power above granules for the period $T = 312$ s. Theory does not explain why velocity oscillates with larger period above granules than above intergranular lanes. Probably, it may be attributed to the second-order effects which are not taken into account by the linear theory we have employed.

CONCLUSIONS

The observations with high spatial ($< 0''.5$) and temporal (9.3 s) resolution and a new method have allowed us to investigate in details the local 5–min oscillations above granules and intergranules. In the upper photosphere

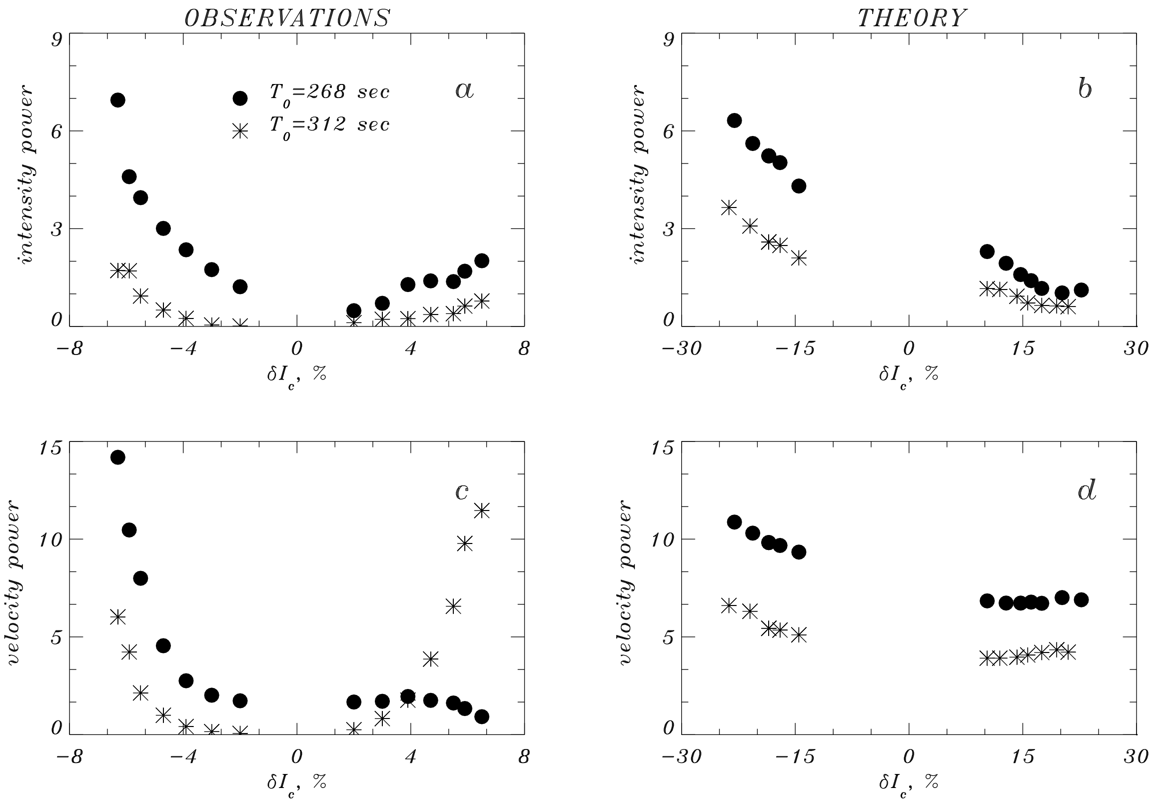

Figure 1: **a** and **b**: power of the intensity oscillations of the line core as a function of the normalized continuum contrast δI_c. **c** and **d**: the same but for velocity oscillations Results for two periods with the maximum power in a spectrum are shown. Filled circles: period 268 s; stars: 312 s. Units for intensity and velocity power are $[\delta I_{0W}/\bar{I}_c]^2$ and $[ms^{-1}]^2 \times 10^{-4}$, respectively. For details see discussion in the text

at a height $\sim$ 500 km, the average amplitudes of velocity oscillations above granules are lower than above intergranules. The main power of the velocity fluctuations concentrates at the frequencies $\omega = 3.21 \pm 0.26$ mHz ($T = 312$ s) and $\omega = 3.73 \pm 0.26$ mHz ($T = 268$ s). Power of the velocity oscillations with $T = 312$ s reaches maximum above the bright areas (granules) while power of oscillations with $T = 268$ s has maximum above the dark intergranular lanes. The main power of the intensity fluctuations concentrates only at $\omega = 3.21 \pm 0.26$ mHz, and above intergranules it is a factor of 3 higher than above granules.

Acknowledgements. Partial support by the Spanish DGICYT under project 91–0530 is gratefully acknowledged. N. G. S. would like to acknowledge the support of the Spanish Ministry of Education for a sabbatical stay at the IAC. The support provided by C. Briand and H. P. Schilling during the observations is gratefully appreciated. We would like to thank M. Vázquez, J. A. Bonet, J. Trujillo Bueno, M. Collados and their colleagues for support, interest and help in our work. Special thanks to M. Asplund for the kind permission to use 3D model atmosphere for the purposes of our study. We are grateful to A. Kosovichev for useful suggestions. We acknowledge support from the Netherlands Organization for Scientific Research (NWO). In this research, we employed in Kyiv a computer (CCD system) funded by the NWO.

REFERENCES

[1] *Asplund M., Nordlund A., Trampedach R., et al.* Line formation in solar granulation. I. Fe line shapes, shifts and asymmetries // Astron. and Astrophys.–2000.–**359**, N 2.–P. 729.

[2] *Bertello L., Caccin B.* Non–adiabatic modelling of "5–min" oscillations: effects on photospheric line profiles // Astron. and Astrophys.–1990.–**231**, N 2.–P. 509–517.

[3] *Brown T. M.* Excitation of the solar p-modes by turbulent stress // Astrophys. J.–1991.–**371**, N 1.–P. 396–403.

[4] *Espagnet O., Muller R., Roudier T., et al.* Spatial relation between the 5-minute oscillations and granular patterns // Astron. and Astrophys.–1996.–**313**, N 1.–P. 297–305.

[5] *Goldreich P., Keeley D. A.* Solar seismology. I. The stability of the solar p-modes // Astrophys. J.–1977.–**211**, N 3.–P. 934–942.

[6] *Goldreich P., Murray N., Kumar P.* Excitation of solar p-modes // Astrophys. J.–1994.–**424**, N 2.–P. 466–479.

[7] *Goldreich P., Kumar P.* The interaction of acoustic radiation with turbulence // Astrophys. J.–1988.–**326**, N 1.–P. 462–468.

[8] *Goode P. R., Gough D., Kosovichev A.* Localized excitation of solar oscillations // Astrophys. J.–1992.–**387**, N 2.–P. 707–711.

[9] *Hoekzema N. M., Brandt P. N., Rutten R. J.* Small scale topology of solar atmospheric dynamics III. Granular persistence and photospheric wave amplitudes // Astron. and Astrophys.–1998.–**333**, N 1.–P. 322–332.

[10] *Hoekzema N. M., Rutten R. J.* Small scale topology of solar atmospheric dynamics II. Granulation, K2ν grains and waves // Astron. and Astrophys.–1998.–**329**, N 2.–P. 725–734.

[11] *Hoekzema N. M., Rutten R. J., Brandt P. N.* Small scale topology of solar atmospheric dynamics I. Wave sources and wave diffraction // Astron. and Astrophys.–1998.–**329**, N 1.–P. 276–290.

[12] *Kostik R., Shchukina N.* Local 5–min oscillations above solar granules and intergranular space // Astron. Lett.–1999.–**25**, N 10.–P. 678–687.

[13] *Kostik R. I.* Influence of the running sound wave on the spectral line profiles. IV. Fe line shifts in the spectrum of the solar disc centre // Astrometriya i Astrofisica.–1974.–**23**, N 1.–P. 52–56.

[14] *Kumar P., Goldreich P.* Nonlinear interactions among solar acoustic modes // Astrophys. J.–1989.–**342**, N 2.–P. 558–575.

[15] *Marmolino C., Severino G.* Phases and amplitudes of acoustic–gravity waves. I. Upward and downward solutions // Astron. and Astrophys.–1991.–**242**, N 1.–P. 271–278.

[16] *Marmolino C., Stebbins R. T.* Wave behavior in the solar photosphere: a comparison of theory and observations // Solar Phys.–1989.–**124**, N 1.–P. 23–36.

[17] *Rodríguez Hidalgo I., Ruiz Cobo B., Collados M.* Granular and intergranular model atmospheres from inversion of solar two–dimensional spectroscopic data // Theory and tests of convection in stellar structure / Eds A. Giménez, E. F. Guinan, B. Montesinos.–ASP Conf. Ser.–1999.–**173**.–P. 313–317.

[18] *Mihalas D., Mihalas B. W.* Foundations of Radiation Hydrodynamics.–Oxford: Oxford Univ. press, 1984.–718 p.

[19] *Noyes R. W., Leighton R. W.* Velocity fields in solar atmosphere. II. The oscillatory field // Astrophys. J.–1963.–**138**, N 2.–P. 631–647.

[20] *Schmieder B.* Linear hydrodynamical equations coupled with radiative transfer in a non-isothermal atmosphere // Solar Phys.–1977.–**54**, N 1.–P. 269–288.

[21] *Schröter E. H., Soltau D., Wiehr E.* The German solar telescopes at the Observatorio del Teide // Vistas in Astronomy.–1985.–**28**, N 2.–P. 519–525.

[22] *Shchukina N. G., Trujillo Bueno J.* Fe I lines in spectra of cool stars: NLTE effects in solar-like atmosphere // Kinematics and Physics of Celestial Bodies.–1998.–**14**, N 4.–P. 315–329.

[23] *Stebbins R. T., Goode P. R.* Waves in the solar photosphere // Solar Phys.–1987.–**110**, N 1.–P. 237–253.

[24] *Title A. M., Tarbell T. D., Topka K. P., et al.* Statistical properties of solar granulation derived from the SOUP instrument on Spacelab 2 // Astrophys. J.–1989.–**336**, N 2.–P. 475–494.

KINETIC ALFVÉN TURBULENCE AND NON–THERMAL BROADENING IN SOLAR FLARES

Yu. Voitenko[1,2] and M. Goossens[2]

[1] *Main Astronomical Observatory, NAS of Ukraine*
27 Zabolotnoho St., 03680 Kyiv, Ukraine
e-mail: voitenko@mao.kiev.ua

[2] *Centre for Plasma Astrophysics, K. U. Leuven*
Celestijnenlaan 200B, 3001 Heverlee, Belgium

Recent observations of soft X-ray nonthermal line broadening and hard X-ray emission in solar flares suggest that the nonthermal broadening is due to plasma turbulence created in the energy release [1]. We develop a model of the impulsive excitation of Alfvén wave turbulence and propose the mechanism for the interruption of spectral energy fluxes in flaring loops. This interruption determines the nonthermal broadening in flares and is important for the selective heating of plasma species and for the acceleration of particles to high energies.

INTRODUCTION

Observations suggest that the bulk flare energy is carried by the ≥ 0.1 MeV proton beams at the onset of solar flares ([4], and references therein). Yohkoh observations provide an additional support for the hypothesis of magnetic reconnection operating in different kinds of solar flares [5]. Fast magnetic reconnection converts the energy of the inflowing magnetic field into the bulk kinetic energy of outflowing plasma, moving with a typical velocity equal to the Alfvén speed based on the inflow condition, $V_{(\mathrm{out})} \approx V_{A(\mathrm{in})}$. For typical coronal conditions, these outflows provide the kinetic energy flux $(0.1-10)\times 10^{11}$ erg cm^{-2} s^{-1}, carried mainly by outflowing ≥ 0.1 MeV protons. A principal question that needs to be answered is the following: how the kinetic energy that is carried by the ≥ 0.1 MeV proton beams is transformed in the corona?

A viable mechanism for the conversion of the proton-beam energy, which accounts for a strong interaction of kinetic Alfvén waves (KAWs) with a plasma, has been proposed ([6], and references therein). The theory was applied to both impulsive compact-loop flares and long-duration events. It was shown that the beam-driven instability of KAWs provides an effective mechanism for the conversion of beam kinetic energy into the energy of waves in the coronal part of just-reconnected flaring loops. Using the theory developed in [7]–[10], we discuss here the properties of the spectral fluxes of energy in the KAW turbulence.

EXCITATION OF ALFVÉN WAVE TURBULENCE IN FLARING LOOPS

In a Maxwellian background plasma, the increment of the KAW instability, driven by the V_z-shifted Maxwellian proton beam with bulk velocity V_{b0}, is [6]:

$$\gamma_k = \sqrt{\frac{\pi}{8}}\omega_k \frac{\mu^2}{K^2}\frac{T_e}{T_i}\left(g_b\frac{n_b}{n_0} + g_i - \frac{V_k}{V_{Te}} + \frac{E_0}{E_{Dr}} + \frac{E_0}{E_{ke}}\right), \tag{1}$$

where $V_k = \omega_k/k_z = V_A K$ is the wave phase velocity along $\mathbf{z} \parallel \mathbf{B}_0$, ω_k and $\mathbf{k}$ are frequency and wave vector of the excited waves, $g_\alpha = \Lambda_{0\alpha}(T_e/T_\alpha)[(V_{\alpha 0}-V_k)/V_{T\alpha}]\exp[-0.5(V_{\alpha 0}-V_k)^2/V_{T\alpha}^2]$ with $\alpha = b$ or i, $E_{ke} = k_z T_e/e$.

In addition, to Cherenkov wave-particle interaction, the effects of the beam-induced electric field E_0 are taken into account in (1). For a super-Alfvén proton beam ($V_{b0} > V_A$), the destabilization in (1) comes from beam–induced inverse Landau damping ($\sim n_b/n_0$), and beam-induced electric field E_0 ($\sim E_0/E_{Dr}$ and $\sim E_0/E_{ke}$) terms. Stabilizing effects are due to the electron Landau damping (term $\sim -V_k/V_{Te}$), and the ion Landau damping (term $\sim g_i$, $g_i < 0$).

We estimate the growth rate of the KAW instability, excited in a flaring loop by a proton beam (typical velocity $V_{b0} \leq 2V_A$, and $n_b/n_0 = 0.2$) as $\gamma_k^L/\Omega_i = 5\times 10^{-2}$. As it has been shown in the framework of quasilinear theory, the beam-driven instability of KAWs can be saturated by the velocity-space diffusion of the beam protons [6]. Here we take into account the stronger nonlinear saturation mechanism [7], giving a saturation level of the wave amplitude in the source ($k_\perp\rho_i \leq 1$) region: $B_s/B_0 = 5\times 10^{-2}$. The nonthermal plasma velocity due to waves may be calculated from the amplitude of wave magnetic field B: $V_{pl} = V_A\left(B/B_0\right)$. With the above values this gives a nonthermal plasma velocity $V_{pl} = 50$ km s^{-1} induced by the waves initially excited by beam.

THE MECHANISM OF THE SATURATION OF SPECTRAL FLUX AND NONTHERMAL BROADENING IN FLARES

The nonthermal velocities, observed as the excess line width of the soft X-ray line emission, are very high at a flare onset, $V_{nt} = 200 - 400$ km s^{-1}, and suggest that the nonthermal broadening is due to plasma turbulence created in the energy release [1]. The direction of energy cascade in the KAW turbulence is towards small k, forming a so-called inverse cascade and the inertial-range spectrum, $\sim k_z^{-1/2}k_\perp^{-2}$ [8], suggesting that the enhanced wave amplitudes in the small-$k_\perp$ domain can explain the nonthermal velocities observed in flares.

The turbulent cascade can be stopped at small $k_\perp$ by the KAW phase mixing [9], and by ion Compton scattering [10]. Here we support the idea that the spectral flux can be eventually stopped by the ion Landau damping [9], even if plasma $\beta_i \left(= V_{Ti}^2/V_A^2\right)$ is initially low, $\beta_i < 0.1$. Indeed, if initially the wave spectrum falls in the domain of strong electron Landau damping, the resulting electron heating will rise β_i to 0.2 via $e - i$ collisions at time scale $\sim 10^{-2}$ s. Then ion Landau damping come into play, and the resulting quasi-stationary dynamic equilibrium comprises: 1) the linear wave excitation at a wavenumber k_s, 2) the nonlinear saturation of the instability at a level B_s/B_0, 3) the inverse turbulent cascade induced by the three-wave resonant interaction, 4) the cascade interruption at a wavenumber $k_{\min} \left(= k_{d\perp}\right)$ by the ion Landau damping. The conditions of the equilibrium, $\gamma_k\left(k_{s\perp}\right) = \gamma_k\left(k_{d\perp}\right)$, $\gamma_k\left(k_{s\perp}\right) = \gamma_{NL}\left(k_{s\perp}\right)$, and $\gamma_{NL}\left(k_{d\perp}\right) = \gamma_k\left(k_{d\perp}\right)$, allow us to determine the energy-containing wavenumber as $k_{\perp\min} \sim 0.3k_{s\perp}$, and the amplitude of magnetic fluctuations as $B \simeq k_{s\perp}^2 k_{\perp\min}^{-2} B_s = 0.2B_0$. This estimation gives the non-thermal velocity of $V_{nt} = 200$ km s^{-1}.

SUMMARY

We investigated the mechanism of the saturation of the spectral flux in the KAW turbulence in flaring loops. This phenomenon determines the nonthermal broadening in flares and selective heating of electrons and ions. The nonlinear saturation level of the wave amplitude in the energy-containing region, $B \sim 0.2B_0$ gives the nonthermal velocity of $V_{nt} = 200$ km s^{-1}, which is typical at flare onset. The heating process undergo a transition from the preferable electron heating at the initial stage of turbulence to the ion heating at the developed stage.

Acknowledgements. Research supported by KUL through grant FWO G.0335.98, and by Ukrainian FFR grant 2.4/1003.

REFERENCES

[1] *Alexander D., Harra-Murnion L. K., Khan J. I., Matthews S. A.* Relative timing of soft X-Ray nonthermal line broadening and hard X-Ray emission in solar flares // Astrophys. J.–1998.–**494**.–P. 235–244.

[2] *Harra-Murnion L. K., Akita K., Watanabe T.* Investigating the nonthermal velocity of small GOES-class flares observed by YOHKOH // Astrophys. J.–1997.–**479**.–P. 464–478.

[3] *Masuda S., Kosugi T., Hara H., et al.* Hard X-Ray Sources and the Primary Energy-Release Site in Solar Flares // Publs Astron. Soc. Jap.–1995.–**47**.–P. 677–687.

[4] *Simnett G. M.* Protons in Flares // Space Sci. Rev.–1995.–**73**.–P. 387–400.

[5] *Shibata K., Masuda S., Shimojo M., et al.* Hot-Plasma Ejections Associated with Compact-Loop Solar Flares // Astrophys. J.–1995.–**451L**.–P. 83–86.

[6] *Voitenko Yu. M.* Excitation of kinetic Alfven waves in a flaring loop // Solar Phys.–1998.–**182**.–P. 411–430.

[7] *Voitenko Yu. M.* Three-wave coupling and parametric decay of kinetic Alfvén waves // J. Plasma Phys.–1998.–**60**.–P. 497 –515.

[8] *Voitenko Yu. M.* Three-wave coupling and weak turbulence of kinetic Alfven waves // J. Plasma Phys.–1998.–**60**.–P. 515–527.

[9] *Voitenko Yu. M., Goossens M* . Turbulent dynamics of kinetic Alfvén waves in a transient flare loop // Magnetic Fields and Solar Processes: Proc. 9th European Meeting on Solar Physics, Florence, Italy, 12–18 September 1999 // ESA SP-448, 1999.–P. 735–740.

[10] *Voitenko Yu. M., Goossens M.* Turbulent dynamics of kinetic Alfvén waves // Physica Scripta.–2000.–**T84**.–P. 194–196.

VELOCITY FIELD IN A SMALL SOLAR FLARE

N. N. Kondrashova, M. N. Pasechnik

Astronomical Observatory, Taras Shevchenko National University
3 Observatorna St., 04053 Kyiv-53, Ukraine
e-mail: kondr@aoku.freenet.kiev.ua

The temporal variations of the line-of-sight velocities have been revealed in a small flare during its main phase. The measurements were made in 34 Fraunhofer lines formed in different photospheric layers. The downflow was observed in the photosphere 4 min after the chromospheric flare peak with the maximum velocity followed 12 min later. The largest velocity variations (up to 1.6 km/s) occurred in the layer 180–220 km. An enhancement of 5-min velocity oscillations was found.

INTRODUCTION

Fisher [3], Somov *et al.* [5], Livshits *et al.* [4] predicted the formation of the chromospheric condensation during impulsive phase of a solar flare. The condensation propagates from the upper into the lower solar atmospheric layers. The radial velocities of the downflow derived in [1, 2] from the Balmer lines were about 30 km/s, 20 km/s from the CaII K line, and 10 km/s from the NA–D_2 line. The velocity diminished with the depth. It is interesting to study the variations of the motion velocities at the photospheric level. In this paper we present the results of the investigation of the matter of the motion changes in the active complex Mc Math 16025+16030 during the main phase of small flare.

OBSERVATIONAL DATA

The flare under the study was of importance sf, it occurred on May 24, 1979 near the solar disk center at 12:56 UT and ended at 13:29 UT, the intensity maximum of the H_α line was reached at 13:02 UT. The spectral observations were made with the solar horizontal telescope ATsU–5 of the Main Astronomical Observatory, of the NAS of Ukraine. The first spectrogram was taken at 13:03.4 UT and the last one – at 13:27.8 UT. Fourteen spectrograms were received with about 1.5–min time intervals. The spectral regions $\lambda\lambda$ 541–543, 588–593, 629–633, 653–659 nm chosen for the investigation included 34 Fraunhofer lines FeI, TiI, CrI, SiI, NiI, CaI, CrII, TiII, and the H_α line. The lines are formed in photospheric layers from 100 to 500 km, they have different intensities and excitation potentials. Besides, we used the spectrum of the quiet photosphere for the comparison. Both the quiet photosphere region and flare kernel area were at the same distance from the disk center. Photometric sections of the spectra were made at the sites of the intensity maximum of the H_α line.

THE LINE–OF–SIGHT VELOCITY VARIATIONS

The line shifts in the AC spectra were determined with respect to their positions in the spectra of the quiet photosphere using telluric lines. In the AC spectra the lines are red–shifted. The line–of–sight velocity changes derived from Doppler shifts of the line core centers in the AC spectra. The largest measurement error was 0.17 km/s. The downflow was observed in the photosphere and chromosphere, its velocity changed both in height and time during the flare. The downward chromospheric motion of about 6 km/s is found from the H_α line obtained at the first observational moment. The downward velocity decreased to 4 km/s during this flare phase.

The velocity deviations reached 0.8 km/s in the upper layers (300–500 km) of the photosphere in the beginning of the observations, 1–4 min after intensity maximum of the H_α line. By the end of the flare they had diminished till 0.35 km/s. The variations of the line–of–sight velocity in the lower layers increased from 0.4 km/s to 0.9 km/s during this time interval. Such changes may be caused by the spread of the flare disturbance from the upper to lower photospheric layers. Possibly, this disturbance is the photosphere response to the passage of the chromospheric condensation and propagation of waves.

In the middle photosphere there was the layer with especially sharp velocity changes (up to 1.6 km/s) at the heights of 180–220 km. This layer is the transition region between the photospheric zones with convective and wave energy transfer.

The variations of the line–of–sight velocities had an oscillatory character with the period of a few minutes in the middle and lower layers. The amplitude of the oscillations was various at different levels: in the upper layers – about 0.6 km/s, in lower ones – about 0.8 km/s, and in layer 180 – 220 km – 1.4 km/s. It is known that the velocity amplitude of 5–min oscillations for the quiet photosphere does not exceed 0.3 km/s. In active regions its value is still less, therefore, it is possible to admit that the increase of the velocity oscillation amplitude obtained is due to influence of the flare disturbance.

REFERENCES

[1] *Cauzzi G., Falchi A., Falciani R., et al.* Coordinated observations of solar activity phenomena II. The velocity field pattern in an elementary flare // Astron. and Astrophys.–1996.–**306**, N 2.–P. 625–637.

[2] *Falchi A., Falciani R., Smaldone L. A.* Analysis of the optical spectra of the solar flares. VI. Velocity field in the 13 June 1980 flare area // Astron. and Astrophys.–1992.–**256**, N 1.–P. 255–263.

[3] *Fisher G. H.* Dynamics of flare-driven chromospheric condensation // Astrophys. J.–1989.–**346**, N 2.–P. 1019–1029.

[4] *Livshits M. A., Badalyan O. G., Kosovichev A. G., et al.* The optical continuum of solar and stellar flares // Solar Phys.–1981.–**73**, N 2.–P. 269–288.

[5] *Somov B. V., Sermulina B. J., Spector A. R.* Hydrodynamic response of the solar chromosphere to an elementary flare burst II. Thermal model // Solar Phys.–1982.–**81**, N 2.–P. 281–292.

STATE OF PLASMA AND MOTIONS IN CHROMOSPHERIC AND PHOTOSPHERIC PARTS OF THE FLARE H_α LOOP

K. V. Alikaeva and S. N. Chornogor

Main Astronomical Observatory, NAS of Ukraine
27 Zabolotnoho St., 03680 Kyiv, Ukraine
e-mail: alikaeva@mao.kiev.ua, kotenko@mao.kiev.ua

The velocity field and the matter state at the chromospheric and photospheric levels in the course of flare development were investigated. To study the physical parameters of the matter in the flare, we used the chromospheric H_α line and some Fraunhofer lines formed at different levels in the photosphere. The observations at the Peak Terskol allowed us to determine the velocities and physical conditions in different parts of the flare H_α loops. The blue shift of the H_α line was recorded only at the impulsive phase and only at the top of the loop. The velocities decrease during one minute and their sign changes at the H_α maximum. Positive line–of–sight velocities were found both in the photosphere and chromosphere at the footpoint of a flaring loop. The velocities drop from 23 km/s in the chromosphere to 0.7 km/s in the middle photosphere. Such motion type points to the flare H_α loop lifting during impulsive phase and downward motion of a matter along the loop branch.
The simulation reveals a condensation arised in the temperature minimum region during impulsive phase at the base of the flare loop. This condensation moves downward. The temperature excess in the flare H_α maximum was about 1000 K and magnetic field strength was 250 G.

INTRODUCTION

The spectral investigations of a flare velocity field allow us to check reliability of theoretical flare models. The spectral line profiles formed in the low-temperature layers of the flare atmosphere, their Doppler shifts, asymmetry give us information about properties of non-thermal particle beams and the hydrodynamical processes in the lower layers of the flare atmosphere (Fisher, 1990; Canfield *et al.*, 1990; Falchi, Qui and Cauzzi, 1997). Unfortunately, the velocity field at the photospheric levels are poorly studied. The preflare increasing of blue shifts of some photospheric lines have been reported in some papers (Rust, 1973; Redjuk, 1985; Falchi, Falchiani and Smaldone, 1992). The ascending motions of the photospheric matter in the impulsive phase were recorded by some authors (Harvey and Harvey, 1976; Redjuk, 1985; Cauzzi *et al.*, 1996). But in the gradual phase only descending motions with velocities of 1-3 km/s were observed in the photosphere (Janssen and White, 1970; Redjuk, 1985; Cauzzi *et al.*, 1996). The observational data on solar flares stored during the last decades show that all the layers of the solar atmosphere take part in flare process. It may be taking into account when the realistic hydrodynamical models are built. Unfortunately, the theoretical models of the hydrodynamical response ignore the photospheric layers of the flare atmosphere and semiempirical models are scanty and they describe the state of the high levels of the photosphere only.

OBSERVATIONS

We study here the velocity field and state of the matter at the chromospheric and photospheric levels in different parts of the flare H_α loop of the faint solar flare sf/c5 on August 2, 1990 (flare beginning – 05:45 UT, max – 05:49 UT, end – 06:03 UT). The photographic spectral observations were carried out at the Horizontal Solar Telescope at the Peak Terskol (h = 3200 m) of the Main Astronomical Observatory of the NASU. The observations period involved the flare H_α maximum and gradual phase. The H_α images of the active region were recorded with TV-camera. The flare was seen as some H_α loops near the spot-leader. The spectrograph slit crossed the east branches of two loops including the regions near the loop tops and their bases.

The photometry was made with an automatic digital two-coordinate microphotometer. The spatial resolution along the slit is of $2''\!.3$ and spectral resolution is of 1 pm for H_α and 0.5 pm for Fraunhofer lines. The spectrograms demonstrate that the knot with a central reversal were located near the flare kernels with H_α emissions at the line centre.

1. LINE–OF–SIGHT VELOCITIES

The chromospheric H_α line and some Fraunhofer lines formed in the high and middle photosphere ($200 < h < 450$ km) were used for determination of the line-of-sight (LOS) velocities in the flare atmosphere. The line shifts were measured with respect to telluric lines. Thus, the LOS velocities were obtained for different moments of the flare evolution and for different photometric sections. The LOS velocities were corrected for the Earth's rotation and revolution around the Sun.

Fig. 1 shows the LOS velocities in the chromosphere (a) and photosphere (b) during the flare for the loop top (dashed line) and base (solid line).

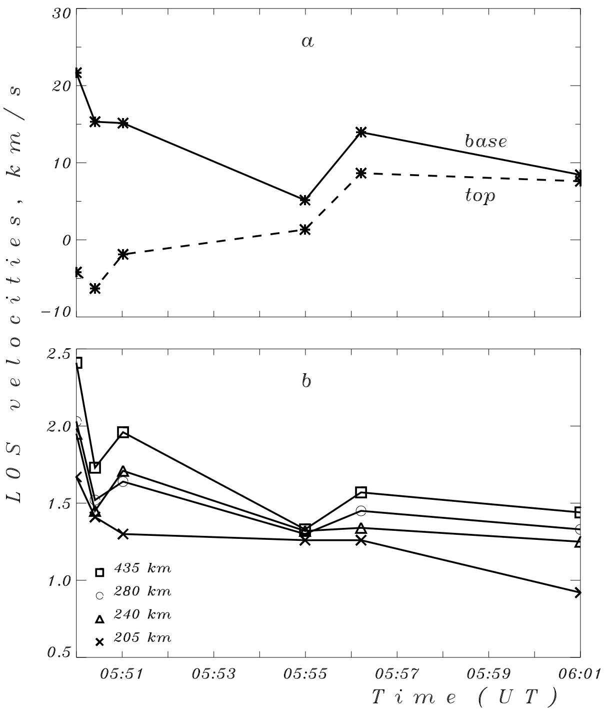

Figure 1: LOS velocities in the chromosphere (a) and photosphere (b) during the flare

In the chromosphere the ascending motions with velocities up to –7 km/s were observed at the top of the loop and during the impulsive phase only. In our opinion, the blue shift of the H_α line is due to upward motion of the loop. This assumption is confirmed by H_α images. In the gradual phase the downward motions of a matter with velocities less than 10 km/s were observed (Fig. 1a). At the loop base the LOS velocities were positive through the all period of flare observation. The maximum velocity was at the H_α maximum at the outer edge of the loop base.

An analogous result was obtained by Falchi *et al.* (1992, 1997) from their study of the velocity field in the high photosphere. Our results are in accordance with the data of Canfield *et al.* (1992) as well. They revealed that H_α red shifts coincide with footpoints of the loop, but not the loop top feature.

In our case the character of the chromospheric velocity field may serve as confirmation of the gradual magnetic reconnection (Forbes and Acton, 1996). Since the velocities did not exceed 30 km/s we consider that the particle beam energy was $< 10^{10}$ erg/(cm^2 s) (Fisher, Canfield and McClymont, 1985).

Fig. 1b shows the LOS velocities at different heights in the photosphere at the base of a flaring loop for different moments of the observation. All the velocities were positive. This points out to the downward motions of the photospheric matter. As in the chromosphere the maximum velocities were at the outer edge of the loop base. The velocities decrease with depth. These variations of the velocities are possible if the flare disturbance propagates from the high layers to the bottom.

2. SEMIEMPIRICAL PHOTOSPHERIC SIMULATIONS

We calculated the semiempirical models of the photospheric part of the flare loop as the distributions of temperature (T), electron (P_e) and gas (P_g) pressure, LOS velocities (v) and longitudinal component of the magnetic field ($H_\parallel$) with optical depth τ_5. The LTE inversion code SIR (Ruiz Cobo, del Toro Iniesta, 1992) allow us to obtain the thermodynamic and magnetic properties of the structures by fitting the whole shape of the observed line profiles.

The dependence T, P_e, P_g, and $H_{\|}$ on $\log \tau_5$ in the impulsive phase are shown in Fig. 2 for the flare loop base. As one can see the distributions of physical parameters reveal some inhomogeneities at the level $-4 < \tau < -1.5$. The temperature excess relatively to VAL–F model equals to 1000 K at the flare H_α maximum. The gas pressure of this condensation is higher than that in the undisturbed atmosphere by two orders. Besides, there are regions of a low pressure. The electron pressure shows the similar picture. The magnetic field strength was up to 250 G. The other peculiarity of these models is a gradual displacement of the condensations to the lower layers. This fact gives an evidence on disturbance penetrating into the photosphere from above.

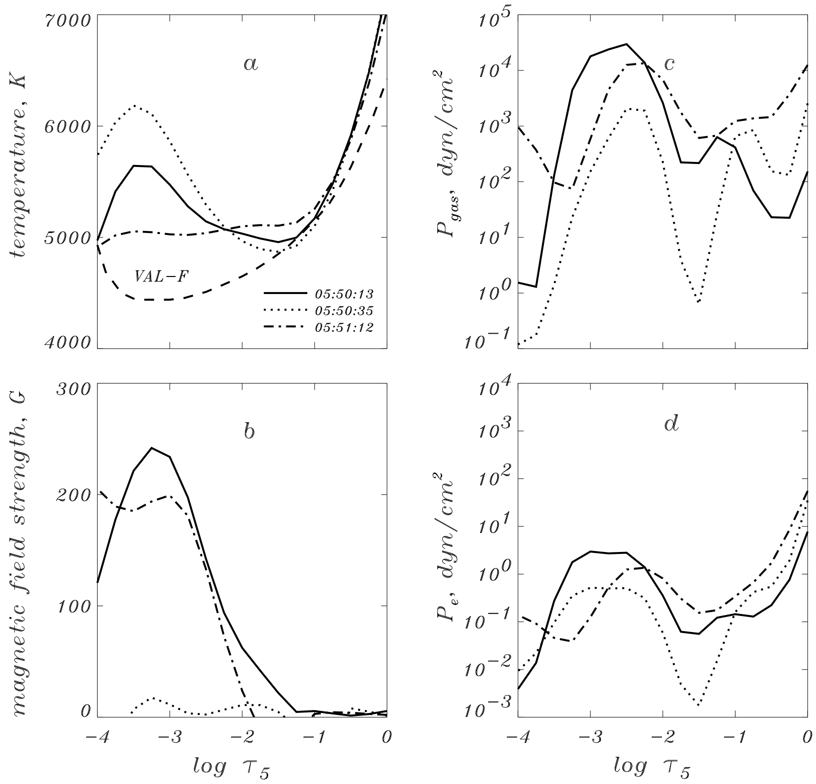

Figure 2: The distributions of temperature (a), longitudinal component of the magnetic field (b), gas (c) and electron (d) pressure with optical depth τ_5 for the flare loop base

The hydrodynamical flare models predicts the formation of the condensation in the impulsive phase moving from the corona to the chromosphere and dissipate there. Fisher, Canfield and McClymont (1985) identify this condensation with a shock wave. According to our study this condensation can penetrate to the photosphere.

CONCLUSIONS

- The upward motions of the chromospheric matter with velocities up to –7 km/s were detected at the loop top at the impulsive phase of the flare only. These motions are due to the loop lifting.
- The change of the velocity sign took place 1 min after the H_α maximum.
- The downward motions were observed both in the chromosphere and photosphere at the loop base during the whole flare. The maximum values of the velocity refer to the outer base edge.
- The downward velocities of the matter varied with height from 23 km/s in the chromosphere to 0.7 km/s in the middle photosphere.
- The model of magnetic reconnection of Forbes and Acton (1996) is the most appropriate for our case.
- A common feature of semiempirical photospheric models is the presence of inhomogeneous layers. At the impulsive phase these inhomogeneities move downward.
- This disturbance of the flare photosphere may be of a wave nature.

REFERENCES

[1] *Canfield R. C., Kiplinger A. L., Penn M. J., Wulser J. P.* // Astrophys. J.–1990.–**363**.–P. 318.

[2] *Canfield R. C., Hudson H. S., Leka K. D., et al.* // Publs Astron. Soc. Jap.–1992.–**44**.–P. 111.

[3] *Cauzzi G., Falchi A., Falciani R., Smaldone L. A.* // Astron. and Astrophys.–1996.–**306**.–P. 625.

[4] *Falchi A., Falciani R., Smaldone L. A.* // Astron. and Astrophys.–1992.–**256**.–P. 255.

[5] *Falchi A., Qiu J., Cauzzi G.* // Astron. and Astrophys.–1997.–**328**.–P. 371.

[6] *Fisher G. H., Canfield R. C., McClymont A. N.* // Astrophys. J.–1985.–**289**.–P. 414.

[7] *Fisher G. H.* // Astrophys. J.–1989.–**346**.–P. 1019.

[8] *Forbes T. G., Acton L. W.* // Astrophys. J.–1996.–**459**.–P. 330.

[9] *Harvey K. L., Harvey J. W.* // Solar Phys.–1976.–**47**.–P. 233.

[10] *Janssen T. J., White K. P.* // Solar Phys.–1970.–**11**.–P. 299.

[11] *Redjuk T. I.* // Solnech. Dannye.–1985.–**11**.–P. 87. (in Russian).

[12] *Ruiz Cobo B., del Toro Iniesta J. C.* // Astrophys. J.–1992.–**398**.–P. 375.

[13] *Rust D. M.* // Solar Phys.–1973.–**33**.–P. 205.

PHENOMENON OF THE SUPERSTRONG MAGNETIC FIELDS IN SOLAR FLARES: OBSERVATIONS AND THEORY

V. G. Lozitsky[1] **and A. A. Soloviev**[2]

[1]*Astronomical Observatory, Taras Shevchenko National University*
3 Observatorna St., 04053 Kyiv-53, Ukraine
e-mail: lozitsky@aoku.freenet.kiev.ua

[2]*Kalmyk State University*
11 Pushkine St., Elista, Kalmykia, Russia
e-mail: solov@adm.kalmsu.ru

The spectral effects in Stokes $I \pm V$ and $I \pm Q$ profiles caused likely by superstrong magnetic fields were discovered in several solar flares observed on the Echelle spectrograph of the Astronomical Observatory of the Taras Shevchenko National University of Kyiv. These effects indicate on the magnetic field strength from 1 to 9 T, magnetic flux of about 10^{12} Wb, and life time from 3 to 20 min. The superstrong fields occur at the branch of magnetic structures with rapid evolution on the diagram "magnetic flux – life time" by Golovko [1]. One of the possible MHD models of such fields is a spherical magnetic vortex [5]. This model has two sets of intermittent discrete states, force-free and singular, and provides an evidence on unlimited high strengths for a short time of vortex evolution.

INTRODUCTION

The first observational results on the problem of superstrong magnetic fields in flares based on the Stokes $I \pm V$ profiles analysis were published in 1993 [2]. The careful verification of the following spectral effects was made in 1998 [3], and it was based on the larger number of observational data as well as on the Stokes $I \pm Q$ profiles. The main conclusion from these investigations is that the phenomenon is real and perhaps arises as a result of the magnetic field amplification at the peak of solar flares. Some observational evidences on existence of such an amplification ("magnetic collapse") was directly observed in the solar flare [3, 4].

In this paper we present a short report about some observational data on this problem obtained after 1998 and some new theoretical ideas.

OBSERVATIONS

Three types of spectral perturbations like Zeeman effect arised in a case of superstrong magnetic fields were detected in several solar flares [3]. One of such perturbations in the Fe I 543.45 nm line is presented in Fig. 1. Due to the very low Lande factor of this line (g = –0.014), similar spectral effects are possible only in a case of magnetic field strength of about a few tesla. The specific effects were observed also in the Fe I 512.37 (g = –0.013) and Balmer lines.

During July 2000 some interesting solar flares were observed on the Echelle spectrograph of the solar telescope of the Astronomical Observatory of the Taras Shevchenko National University of Kyiv. One of such flares, of July 19, 2000 had coordinates 14°S, 15° E, and the peak of metallic emission nearly 7:20 UT.

The preliminary investigation of the Stokes $I \pm V$ profiles of the Fe I 543.45 nm line in the flare of July 19, 2000 shows that some spectral manifestations to a superstrong field exist in this flare as well. However, due to the emission, the intensity in the flare of July 19 is much less than that in the flare of June 16, 1989, and an additional study is necessary to make more certain conclusion.

At present we can point to the following characteristics of the observational features with superstrong fields: the magnetic field strength from 1 to 9 T, both the horizontal and vertical scales of about 10^3 km (including the range of the upper photosphere, temperature minimum zone and low chromosphere), typical life time from 3 to 20 min, vertical magnetic field gradient of about 1–10 mT/km, magnetic flux of 10^{12} Wb. It is important to note that the field strengths are strongest at the flare peak rather than in the flash phase. The superstrong fields occur near the branch of magnetic structures with rapid evolution on the diagram "magnetic flux – life time" by Golovko [1].

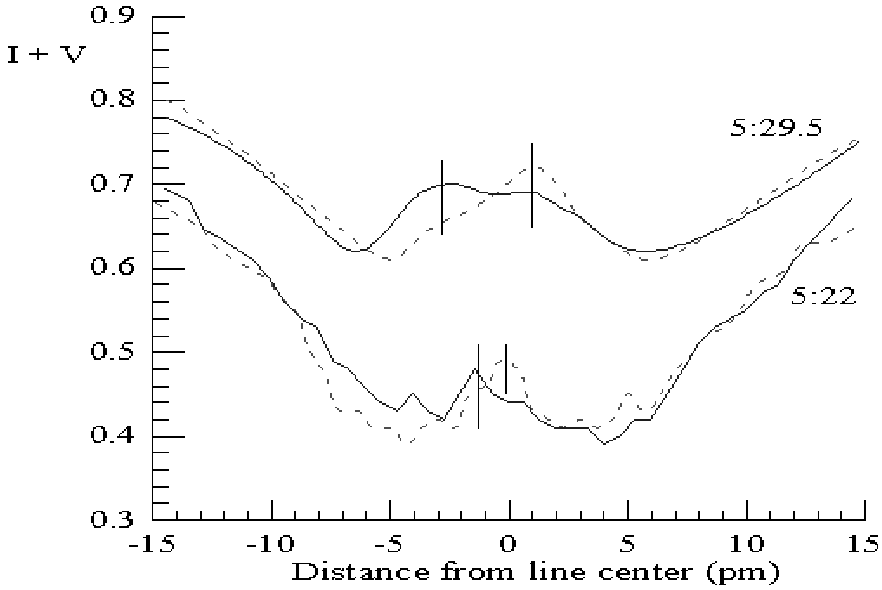

Figure 1: Observed Stokes $I \pm V$ profiles for Fe I 543.45 nm line (g = –0.014) in solar 2B-flare of June 16, 1989: 5:22 UT – the flash phase, 5:29.5 UT – the flare peak. One can see the very narrow ($\approx 3-5$ pm) emission peaks in the line core which are *shifted mutually along wavelengths*, and have *the opposite asymmetry.* These pecularities could evidence on the superstrong magnetic fields in the flare, about of 2.5 T for the flash phase and 9 T for the flare peak

THEORY

One of the possible MHD models of such fields is a spherical magnetic vortex [5]. This model has two sets of intermittent discrete states, the force-free and singular one. Two possible mechanisms could lead to the loss of the system's equilibrium: relatively slow Ohmic dissipation, and external perturbations rotating one of the inner magnetic tores by 180 degrees, and producing neutral current sheets inside the spheroid. The energetic and temporal estimates for this process are in agreement with observations.

REFERENCES

[1] *Golovko A. A.* Solar Maximum Analysis (Addit. Issue).–Novosibirsk: Nauka, 1988.–274 p.

[2] *Lozitsky V. G.* Superstrong magnetic fields in flares // Kinematics and Physics of Celestial Bodies.–1993.–**9**, N 3.–P. 23–32.

[3] *Lozitsky V. G.* Observations of magnetic fields with strengths of several tesla in solar flares // Kinematics and Physics of Celestial Bodies.–1998.–**14**, N 5.–P. 401–414.

[4] *Lozitsky V. G., Baranovsky E. A., Lozitska N. I., Leiko U. M.* Observations of magnetic field evolution in a solar flare // Solar Phys.–2000.–**191**, N 2.–P. 171–183.

[5] *Soloviev A. A.* The spherical magnetic fortex as an element of solar activity // Astron. Zh.–1998.–**75**, N 5.–P. 783–791. (in Russian).

NONLINEAR THREE–WAVE INTERACTION OF KINETIC ALFVÉN WAVES IN THE CORONAL LOOPS

P. P. Malovichko

Main Astronomical Observatory, NAS of Ukraine
27 Zabolotnoho St., 03680 Kyiv, Ukraine
e-mail: malovich@mao.kiev.ua

The interaction of kinetic Alfvén waves (KAW) with particle is very effective and essentially depend on the transversal length of the waves, which propagate in the coronal loops. Therefore, it is very important to know how the Alfvén wave spectrum is formed. In this work the resonance interaction of three Alfvén waves is shown to be one of the most important mechanism of such a spectrum formation. This interaction is very efficient when kinetic effects have considerable influence on the Alfvén wave dispersion. For some waves (with sufficiently small transverse wave lengths) the rate of transformation of one wave into another may even reach the frequency of initial wave. The results obtained may be used for the interpretation of the low frequency waves spectra observed in the solar atmosphere and explanation of the particle acceleration and coronal loops heating mechanisms.

INTRODUCTION

The basic dynamic processes in the photosphere-coronal plasma occur as wave processes. The photosphere is permanently disturbed being continuous source of waves propagating in the upper atmosphere. However, the sound and magneto-sound waves are known to undergo a strong refraction in the chromosphere, which prevents their emerge in the corona. Thus, to explain processes occurring in the coronal plasma, the Alfvén waves leaving freely the photosphere through the open magnetic force lines are the most suitable. Besides, such waves can be generated in the corona, for example in flaring coronal loops [1]. When propagating in the chromosphere and corona, the Alfvén waves can essentially change the spectrum owing to their nonlinear interaction with particles of plasma [2, 3]. Really, as follows from the two-fluid hydrodynamics [4], the nonlinear interaction of Alfvén waves appears very large and the characteristic time of interaction can be of an order of frequencies of interacting waves. It is necessary to note that the hydrodynamics does not give absolutely exact results, as apparent from comparison of the dispersion of kinetic Alfvén waves obtained in the hydrodynamics and kinetics.

From hydrodynamics for Alfvén waves we have

$$\omega^2 = (k_z v_A)^2 \left[1 + \left(1 + \frac{T_e}{T_i}\right) z_i\right], \tag{1}$$

where $z_i = (k_\perp v_{Ti}/\omega_{Bi})^2$, ω is the frequency of the wave, k_z, $k_\perp$ are the longitudinal and transverse wave vectors, v_A is the Alfvén velocity, v_{Ti} is the thermal velocity of ions, T_e, T_i are the electron and ion temperatures, ω_{Bi} is the ion cyclotron frequency.

From the kinetic equations for Alfvén waves we have [2]

$$\omega^2 = (k_z v_A)^2 \left[1 + \left(\frac{3}{4} + \frac{T_e}{T_i}\right) z_i\right], \quad z_i << 1,$$
$$\omega^2 = (k_z v_A)^2 \left[1 + \frac{T_e}{T_i}\right] z_i, \quad z_i >> 1. \tag{2}$$

It is apparent that dispersions well coincide only for rather large values of cross wave vectors. Besides, the complete dispersion of kinetic Alfvén waves obtained in the kinetic approximation contains the modified Bessel function [2, 3]

$$\omega^2 = (k_z v_A)^2 \left[\frac{z_i}{1 - A_0(z_i)} + \frac{T_e}{T_i}\right], \tag{3}$$

which in the hydrodynamics fails to be obtained. In (3) $A_0(z) = I_0(z)\exp(-z)$, $I_0(z)$ is the zero-order modified Bessel function. The greatest difference in dispersion is observed at a finite ratio of the Larmor radius to the wave length. That is the most interesting part of the spectrum, where the interaction between waves, as well as the interaction of waves with particles intensively occur. The kinetic approach is more exact because all quantities including the tensor of pressure are calculated instead of being chosen from the equation of state or otherwise.

NONLINEAR INTERACTION OF KINETIC ALFVÉN WAVES (KINETIC APPROACH)

Interaction of Alfvén waves in the kinetic approximation was considered in [5]. In this work, two potential approximations were carried out. In present work, such approximations were not made. The complete set of Maxwell and Vlasov kinetic equations was used. The system of three nonlinear equations describing nonlinear three wave interactions of kinetic Alfvén waves and taking into account of polarization of fields and currents was obtained

$$\begin{aligned}
\frac{dB_{\perp k}}{dt} &= \frac{1}{2}\omega_{Bi}\frac{v_A}{v_{Ti}}\int dk_2 dk_1 \delta(k-k_2-k_1)\frac{\mathbf{k}_{\perp 1}\times\mathbf{k}_{\perp 2}}{k_{\perp 1}k_{\perp 2}}\frac{1}{z_i^{1/2}}B_{\perp k_1}\frac{B_{\perp k_2}}{B_0} \\
&\quad [z_i(D_1-D_2)+D(z_{i1}-z_{i2})+DD_1D_2(A_{01}-A_{02})]\,, \\
\frac{dB_{\perp k_1}}{dt} &= -\frac{1}{2}\omega_{Bi}\frac{v_A}{v_{Ti}}\int dk_2 dk \delta(k-k_2-k_1)\frac{\mathbf{k}_{\perp 1}\times\mathbf{k}_{\perp 2}}{k_{\perp 1}k_{\perp 2}}\frac{1}{z_i^{1/2}}B_{\perp k}\frac{B_{\perp k_2}}{B_0} \\
&\quad [z_{i1}(D-D_2)+D_1(z_i-z_{i2})+DD_1D_2(A_0-A_{02})]\,, \\
\frac{dB_{\perp k_2}}{dt} &= -\frac{1}{2}\omega_{Bi}\frac{v_A}{v_{Ti}}\int dk_1 dk \delta(k-k_2-k_1)\frac{\mathbf{k}_{\perp 1}\times\mathbf{k}_{\perp 2}}{k_{\perp 1}k_{\perp 2}}\frac{1}{z_i^{1/2}}B_{\perp k}\frac{B_{\perp k_1}}{B_0} \\
&\quad [z_{i2}(D_1-D)+D_2(z_{i1}-z_i)+DD_1D_2(A_{01}-A_0)]\,,
\end{aligned} \tag{4}$$

where $D_n = \dfrac{k_{zn}v_A}{\omega_n}\dfrac{z_{in}}{1-A_0(z_{in})}$, $z_{in} = (k_{\perp n}v_{Ti}/\omega_{Bi})^2$, $\omega = \omega_1+\omega_2$, $\mathbf{k} = \mathbf{k}_1+\mathbf{k}_2$.

As one can see, contrary to [5], the nonlinear interaction of waves depends on the modified Bessel functions. For the real events and phenomena occurred in the chromosphere-coronal plasma with participation of Alfvén waves, Eq. (4) will give more exact result in the spectral region where both the waves coupling and waves interaction with particles are the most intensive.

As Eq. (4) shows, the nonlinear interaction of Alfvén waves in the solar atmosphere occur very actively and the spectra of waves can significantly vary from the photosphere to the corona. Therefore, in concrete models of heating and acceleration of particles by kinetic Alfvén waves it is necessary to take into account nonlinear interaction of Alfvén waves and to calculate the form of a spectrum obtained as a result of such interaction.

REFERENCES

[1] *Voitenko Yu. M.* Excitation of kinetic Alfvén waves in a flaring loop // Solar Phys.–1998.–**182**.–P. 411–430.

[2] *Hasegawa A., Chen L.* Kinetic processes in plasma heating by resonant mode conversion of Alfvén waves // Phys. Fluids.–1976.–**19**.–P. 1924–1934.

[3] *Voitenko Yu. M., Koutz S. V., Malovichko P. P., et al.* Kinetic properties of Alfvén waves.–Kyiv, 1990.–(Preprint / NASU. Bogolyubov Institute for Theoretical Physics). ITF-90-75P.

[4] *Volokitin A. S., Dubinin E. M.* The turbulence of Alfvén waves in the polar magnetosphere of the Earth // Planet. and Space Sci.–1989.–**37**, N 77.–P. 761–765.

[5] *Voitenko Yu. M.* Three-wave coupling and parametric decay of kinetic Alfvén waves // J. Plasma Phys.–1998.–**60**, N 2.–P. 497–514.

ANOMALOUS DECREASE OF THE TURBULENT VELOCITIES IN SOLAR MAGNETOPLASMA WITH STRONG AND SMALL–SCALE MAGNETIC FIELDS

V. G. Lozitsky[1], **M. Yu. Gordovsky**[2], **N. I. Lozitska**[1], **and E. Golbraikh**[3]

[1]*Astronomical Observatory, Taras Shevchenko National University*
3 Observatorna St., 04053 Kyiv-53, Ukraine
e-mail: lozitsky@aoku.freenet.kiev.ua

[2]*Physical Department, Taras Shevchenko National University*
6 Glushkova St., 03022 Kyiv, Ukraine

[3]*Ben-Gurion University of the Negev, Post Box 653*
Beer-Sheva 84105, Israel
e-mail: golbref@bgumail.bgu.ac.il

The extremely narrow metallic emissions were observed in several solar flares of 1989, 1991 and 2000. Our analysis is based on the Stokes $I \pm V$ and $I \pm Q$ spectra obtained using the Echelle spectrograph of the Astronomical Observatory of the Taras Shevchenko National University of Kyiv. The careful data reduction for excluding the instrumental broadening effect shows that the intrinsic half width of the emission peaks in the Fe I lines was in the range from 1–2 to 10 pm. The extraordinary narrow peaks (nearly 1.5 pm) are inherent in 5–10 percents of a total number of observed profiles, mainly in the case of very weak flare emissions. The obtained data point out to some specific process like the "frozening" of plasma motions in the strong and small-scale magnetic fields.

INTRODUCTION

In this paper we present a very short description of some new results related to phenomenon of anomalous narrow flare emission in the metallic lines. This phenomenon was preliminary studied by Lozitsky, Lozitska and Gordovsky [1] on a base of two solar flares (namely on June 16, 1989 and July 25, 1991) observed with the Echelle spectrograph of the horizontal solar telescope of the Astronomical Observatory of the Taras Shevchenko National University of Kyiv. Detail description of this instrument and the Stokes $I \pm V$ and $I \pm Q$ observations are presented in [2].

OBSERVATIONAL DATA

We have investigated the flare of June 16, 1989 in more details. Two spectral lines, Fe I 5434.5 Å and Fe I 5446.9 Å with Lande factors – 0.014 and 1.25 were studied. The first line with Lande factor of near zero is the most suitable to determine turbulent velocities.

It was found that the observed half width of the emission peaks in cores of the Fe I 5434.5 Å line, $\Delta\lambda_{1/2}$, depends on the peak intensity I measured as their heights above Fraunhofer profile (Fig. 1). One can see that the regression linear dependence gives the value $\Delta\lambda_{1/2} \approx 3.4$ pm for $I = 0$, that is practically equal to the instrumental profile width (3.0 pm). It means that the true half width of the pure emission could be more less than 3.4 pm.

Similar narrow emissions were observed also in 2N flare of July 19, 2000. This flare had coordinates 14°S, 15°E, and peak of metallic emission nearly 7:20 UT.

To obtain the true profiles of spectral lines we used two different methods (see [1]) including the Fourier-regularization technique. Our reduction of the observed profiles shown that majority of the pure emission peaks in Fe I lines were 5–6 pm wide. The upper limit of the half width is of about 10 pm, but the lower – in the range 1–2 pm. Possible errors of the reduction are of about $\pm(0.5 - 1)$ pm, and depend mainly on the accuracy of the instrumental profile and method of interpretation of emission peak intensity. It is necessary to point out that the reduction procedures do not exclude an unlimited narrow profile like the delta-function. This problem needs, however, a special study and could be resolved in the future.

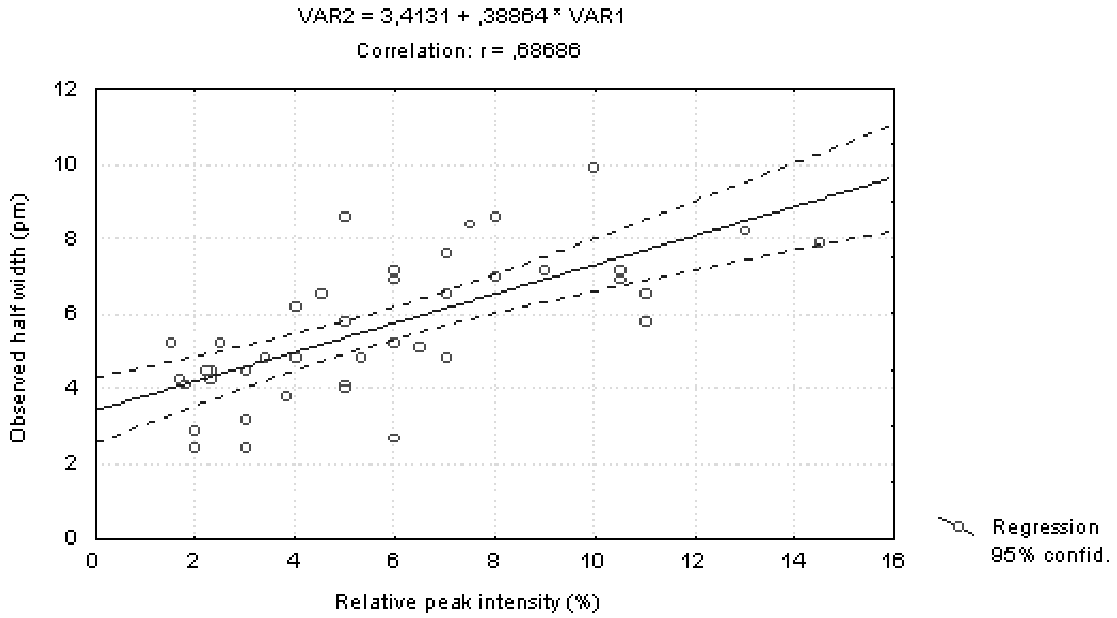

Figure 1: Observed half width of the emission peaks in cores of Fe I 5434.5 Å versus peak intensity measured as their heights above the Fraunhofer profile in the flare of June 16, 1989

WHY DO THE VERY NARROW EMISSION PEAKS ARISE?

It is obviously that such very narrow profiles (1–2 pm) indicate formally to the very low turbulent velocities ξ and temperatures T in flares. If $\xi = 0$, then T is *several times less than that in the undisturbed atmosphere* [1]. It may be assumed that some specific process like the "frozening" of motions occurs in flares. So long as magnetic fields in flares have subtelescopic structure [1, 2], such a process could be especially strong inside the small-scale magnetic fluxtubes with kG strengths.

As to possible theoretical interpretation, there is a sharp drop of the magnetic Reynold's number (a drastic increase in the Joule dissipation) in the reconnection zone [3]. Then the local growth of the magnetic field combined with this effect leads to the intense turbulence suppression, as observed, for instance, in laboratory MHD flows in the external magnetic field [4]. Simultaneously, owing to turbulent energy transformation into heat, the temperature increases in the reconnection zone and the additional ionization occurs. Plasma rejected from the diffusion zone along magnetic field lines recombines in the process of cooling, which leads to the formation of the emission lines. However, in this case the motion of plasma particles can considerably differ from the thermal ones. Thus, we can assume that the Joule dissipation in the diffusion zone, turbulence suppression, and change in the velocity distribution law in the process of magnetic field reconnection at the burst origin leads to the formation of anomalously narrow emissions in spectral lines.

REFERENCES

[1] *Lozitsky V. G., Lozitska N. I., Gordovsky M. Yu.* Observations of the anomalous narrow emissions in metallic spectral lines in solar flares // Visnyk Kyiv Univ., Astronomia.–1999.–**35**.–P. 17–21.

[2] *Lozitsky V. G., Baranovsky E. A., Lozitska N. I., Leiko U. M.* Observations of magnetic field evolution in a solar flare // Solar Phys.–2000.–**191**, N 2.–P. 171–183.

[3] *Parker E. N.* Cosmical Magnetic Fields.–Oxford: Clarendon Press, 1979.–607 p.

[4] *Krause F., Radler K.-H.* Mean-Field Magnetohydrodynamics and Dynamo Theory.–Berlin: Academic-Verlag, 1980.–269 p.

ZONAL LATITUDE STRUCTURE OF THE SUN'S GLOBAL MAGNETIC FIELD EXCITED BY TURBULENT DYNAMO MECHANISM

V. N. Kryvodubskyj

Astronomical Observatory, Taras Shevchenko National University
3 Observatorna St., 04053 Kyiv-53, Ukraine
e-mail: krivod@aoku.freenet.kiev.ua

This study is performed on the base of the turbulent dynamo model allowed newer helioseismic measurements of the Sun's inner rotation. It is shown that the physical conditions in the deep layers of the solar convection zone in the near-pole domain are favourable for exciting of quadrupole mode of the poloidal magnetic field near maximum phase of the 23rd solar cycle.

Magnetographic observations of the poloidal field of the Sun evidence that this field may be generally described by simple magnetic dipole with antisymmetric polarity relatively to the equator. In this case the synoptic maps of the polarity distribution of large-scale surface (background) magnetic field manifest the two latitudinal zones with opposed magnetic polarity on both side of equator. However, both poles of the polar magnetic field had the same polarity during last four solar activity maximums. To interpret this observed magnetic anomaly some investigators consider the quadrupole mode, which is symmetric relative to equatorial plane, to predominate in the poloidal field at this time. Then the maps of magnetic polarity distribution must display four latitudinal zones, and two zones of opposite signs in each hemispheres. Here we try to reveal the possibility of exciting the quadrupole mode of the poloidal field in the Sun's deep layers in the frame of the main magnetic field theory with allowance for newer helioseismic measurements of the inner rotation rate.

According to the dynamo model the combination of the differential rotation and helical (hyrotropic) turbulence in the solar convection zone (SCZ) near the tachocline (a region of strong shear of the angular velocity at the base of the SCZ) produces the toroidal and poloidal components of the Sun's global magnetic field ($\alpha\Omega$-dynamo mechanism). Parker has suggested the solution of dynamo equations for global magnetic components in the form of migratory dynamo waves. Using the boundary conditions, he reduced the dynamo problem to the solution of the dispersion relations that describe the character of the dynamo-effect. Excitation thresholds of multipole modes are determined by eigenvalues of the dispersion relations, *i.e.*, numbers $K\lambda$ (K is the wave number of the dynamo wave, λ is the characteristic scale of the dynamo region). Parker [1] found by model calculation that the excitation thresholds of the periodic dipole and quadrupole modes are rather close. The wave number is determined by physical parameters of the SCZ, $K = (\alpha G/{\nu_T}^2)^{1/3}$ (α is the helicity parameter of turbulent convection, $G = r\partial\Omega/\partial r$ is the measure of the radial differential rotation $\partial\Omega/\partial r$ at the distance r from the Sun's centre, ν_T is the turbulent viscosity) and defines the scale of the magnetic field change. The direction of the dynamo-wave migration depends on a sign of the wave number. The magnetic wave travels equatorwards when $K < 0$, and polewards when $K > 0$.

Since the excitation thresholds of the periodic dipole and quadrupole modes are rather close then it is possible that the quadrupole may be excited when physical parameters (α, ν_T, $\partial\Omega/\partial r$) being changed in a some regions of the SCZ. Recently, helioseismic measurements [2, 3] have shown a strong dependence of the differential rotation on heliolatitude and depth in the SCZ. The inner regular velocity field is naturally divided in each hemisphere on two domains of the fast (near-equator domain) and slow (near-pole domain) rotation, with opposite sign of $\partial\Omega/\partial r$ in each domain. The angular velocity decreases with depth ($\partial\Omega/\partial r > 0$) in the near-equator domain, and increases ($\partial\Omega/\partial r < 0$) in the near-pole domain.

We calculated numbers $K\lambda$ for the SCZ model by Stix [5] (on the depth 175,000 km) using our estimation of helicity parameter [4] and the values of the radial gradient of angular velocity obtained from newer helioseismic measurements near the maximum phase of the 23rd solar cycle (May 1995 – November 1999) [3]. It was found that the calculated value $K\lambda$ is to be about -7 at low latitudes $\theta = 0^\circ - 40^\circ$ in domain-1 (where $\alpha < 0$ and $\partial\Omega/\partial r > 0$) near tachocline. The value obtained is close to the eigenvalue of -7.43 by Parker [1] which is necessary for dipole exciting. The radial gradient of angular velocity changes its sign on opposite at the latitudes higher then 50° so the value $K\lambda$ also changes its sign in the near-pole domain-2 ($\alpha < 0$ and $\partial\Omega/\partial r < 0$): here $K\lambda$ amounts to $\approx +8$ that is close to eigenvalue $+7.43$ necessary for quadrupole exciting.

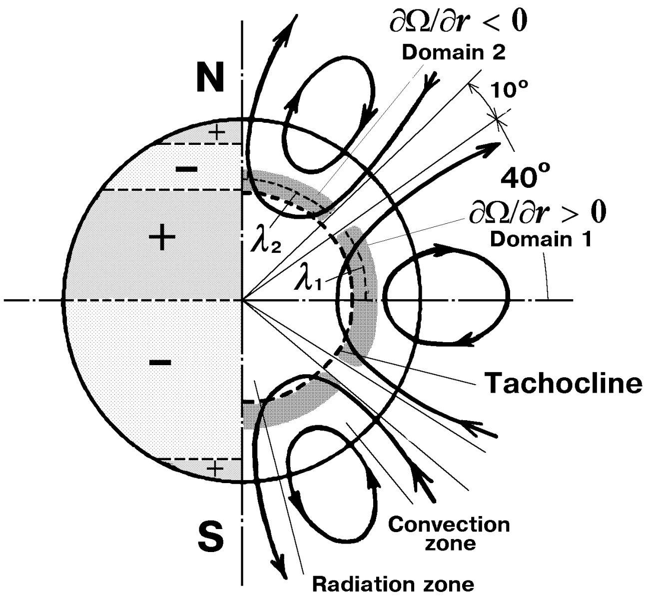

Figure 1: Dipole and quadrupole modes of the poloidal magnetic field excited by $\alpha\Omega$-dynamo mechanism in the SCZ near tachcline near maximum phase of 23rd solar cycle. Right hemisphere: force lines of the dipole ($\theta^* < 40°$) and quadrupole ($\theta^* > 50°$); left hemisphere: corresponding latitudional zones with positive (+) and negative (–) polarities of observed large-scale surface (background) magnetic field

Thus, during rising phase of the 23rd solar cycle the turbulent dynamo mechanism in the near-equator domain in the vicinity of tachocline produces the dipole mode of the poloidal field (migrated equatorwards since $K < 0$); while near-pole domain conditions are more favourable for exciting the quadrupole mode (migrated polewards, $K > 0$). As a result, the maps of polarity distributions of the observed large-scale phothosheric magnetic field in the northern hemisphere display three latitudinal zones with intermittent polarity, and two latitudinal zones in the southern hemisphere. In this case the both near-polar zones should have the same magnetic signs. This gives a possibility to explain the surface polar field magnetic symmetry relative to equator at the solar cycle maximum.

REFERENCES

[1] *Parker E. N.* The generation of magnetic fields in astrophysical bodies. IV. The solar and terrestrial dynamos // Astrophys. J.–1971.–**164**.–P. 491–510.

[2] *Tomczyk S., Schou J., Thompson M. J.* Measurement of the rotation rate in the deep solar interior // Astrophys. J. Lett.–1995.–**448**, N 1.–P. L57–L60.

[3] *Howe R., Christensen-Dalsgaard J., Hill F., et al.* Dynamic variations at the base of the solar convection zone // Science.–2000.–**287**.–P. 2456–2460.

[4] *Krivodubskyj V. N.* Rotational anisotropy and magnetic quenching of gyrotropic turbulence in the solar convective zone // Astron. Rep.–1998.–**42**, N 1.–P. 122–126.

[5] *Stix M.* The Sun.–Berlin, 1989.–200 p.

CALCULATION OF DAMPING CONSTANT OF FRAUNHOFER LINES IN THE SOLAR ATMOSPHERE

L. Yankiv-Vitkovska

Department of Astrophysycs, Ivan Franko National University of Lviv, Lviv, Ukraine
e-mail: `vita@astro.franko.lviv.ua`

Reliable data on spectral lines damping are required to define chemical content of stellar atmospheres. We propose explicit expressions for the damping constant, which take into account several mechanisms influencing the extension of spectral lines. Considering inelastic collisions, we calculate the damping constant for some spectral lines under various temperatures. Using the most correct and empirically tested method for investigations of spectral lines we calculate the damping constant for spectral lines of iron group in the solar atmosphere.

The problem of the damping constant emanates from deficiency of reliable theoretical results, which according to opinion of many authors is related to computational complications. A theoretical value of the damping constant does not always coincide with the value determined from the observed spectra profiles. This is the case even for the solar atmosphere. Furthermore, for the conditions close to the solar atmosphere the damping constant is calculated theoretically only for several lines. The corresponding value lays within the interval $(1.1\ldots1.9)\gamma_6$, where γ_6 is the classical (Unsold) approximation for van der Waals interaction. Results of laboratory measurements appear to be even more inconsiderable in number and unreliable since it is practically impossible to reproduce in a laboratory the conditions prevailing in the solar atmosphere. Specifically, it is difficult to carry out an experiment with hydrogen as a basic agent of van der Waals collisions in conditions of the solar atmosphere. However, the results of laboratory investigations yield a correction factor for γ_6 only a bit greater than 1. Many attempts of empirical studies of Fraunhofer's lines damping constant were made in order to verify and improve theoretical and laboratory results.

Recently, modern devices have allowed an improvement of the precision of the observed data; there appeared more accurate laboratory measurements of atomic parameters and interaction constants and more adequate models of the solar atmosphere have been devised. However, no convenient formulae have been introduced so far which provide theoretical estimation of the damping constant by account of all the mechanisms bringing about the extension of spectral lines profiles. A problem of explicit calculation of a whole profile when only a few mechanisms act is apparently not simple, and also calls for separate researches. The misarranged empirical methods and inconsistency of the observed data with theoretical calculations are considered as an inability of theory to provide the quantitative description of profiles of Fraunhofer's lines, or as an unreliability of the damping constant theoretical computations.

Starting from the first principles for expressions for the damping constant, a series of mechanisms is found, which lead to its increase in comparison with Weisskopf-Lindholm damping for van der Waals interatomic interactions [1].

As it is known, in order to obtain trustworthy conclusions about nature and structure of space objects, the analysis of star radiation requires the detailed study of mechanisms of interaction between radiation and atomic systems. Atmospheres of the majority of stars consist preliminary of hydrogen and helium, while the quantity of atoms of other elements is of few orders less. Certain amount of atoms and molecules are on various ionization levels due to interactions with radiation and among themselves. The full description of star atmospheres needs a simultaneous solution of the transfer equation and the equations determining occupations of atoms quantum states. Within the approach of one-photon transitions a central role in the description is played by the light absorption coefficient.

The profile of the so-called absorption coefficient in a line, that is its dependence on light frequency, as well as the profile of atom spectral line are formed by a series of mechanisms. Among the mechanisms which are responsible for the full profile the colliding mechanism is determinative for the spectral line wing and leads to the formation of the Lorentz profile.

The Lorentz profile is characterized mainly by the damping constant γ, which determines the profile width. The value and temperature dependence of the constant are of particular importance for star spectra analysis. To adjust the observed profiles of Fraunhofer's lines with theoretically calculated profiles, the damping constant obtained from the Weisskopf-Lindholm theory is often increased artificially. In some cases the (required) magnification is unnaturally large, which is interpreted as theory inability to give a quantitative description of profiles of Fraunhofer's lines. In our opinion this is an incorrect point; it is necessary to carry out a detailed investigation of quantities obtained from the first principles and characterizing profiles of atomic spectral lines.

The damping constant γ and the frequency shift Δ of radiation of an atom interacting with other particles according to mechanisms responsible for the Lorentz constituent of a spectral line:

$$I(\omega) = \frac{\gamma}{2\pi} \frac{1}{(\omega - \omega_0 - \Delta)^2 + (\gamma/2)^2} \tag{1}$$

are connected with scattering cross-section σ by the following equation:

$$\gamma/2 - i\Delta = \frac{N}{V} < v\sigma >, \tag{2}$$

where

$$\sigma = \int\limits_0^\infty (1 - e^{i\delta}) 2\pi\rho d\rho. \tag{3}$$

In the above formula ρ denotes aiming distance, while complex phase reads

$$\delta = \eta + i\Gamma, \tag{4}$$

where real part η is equal to the difference between shifts of atomic phases, among which the transitions of frequency ω_0 occur. This phase shift is caused by the shift of atomic energy levels as a result of interaction among atoms and perturbing particles. Let us consider for simplicity of records N particles of one sort embedded in volume V. Moreover, this is just the case which occurs in star atmospheres, since basically atoms of hydrogen are the perturbing particles there. The value of 2Γ is equal to the total probability of atom transition from states, between which transition of frequency ω_0 takes place, to all other states. The quantity Γ causes an additional extension of spectral lines, the so-called extension caused by elastic collisions. Natural or radiation width of an atomic spectral line is not taken into account. The quantity v means atom velocity relatively to a perturbing particle; brackets in Eq. (2) stay for averaging over velocities.

The computations are performed in assumption that quasi-classical approximation is fulfilled, when a real part of the phase reads:

$$\eta = -\frac{1}{\hbar} \int\limits_{-\infty}^{\infty} \Delta E(t) dt. \tag{5}$$

Here ΔE is the correction to atom energy, caused by its interaction with a perturbing particle, t is the time.

We consider a rare particles system similar to star atmosphere. In this case the contribution to η will be determined mainly by interactions between particles in large distances. Then the potential energy $U(R)$ consists of interactions between their multipole momenta and decreases with the distance R according to a power law:

$$U(R) = -\hbar \sum_{l \geq 0} \frac{C_{n+2l}}{R^{n+2l}}, \tag{6}$$

where n determines the type of interaction, $\hbar$ is Planck constant.

Considering the Maxwell distribution over velocities, the dependence of a damping constant on temperature is obtained within the Weisspopf-Lindholm approximation. The corresponding expression reads:

$$\gamma_0 = \frac{N}{V} 4\sqrt{\pi} \left(\frac{2T}{M}\right)^{\frac{n-3}{2(n-1)}} \Gamma\left(\frac{2n-3}{n-1}\right) \Gamma\left(\frac{n-3}{n-1}\right) \left[\frac{\Gamma(1/2)\Gamma(\frac{n-1}{2})}{\Gamma(n/2)} C_n\right]^{\frac{2}{n-1}} \times$$
$$(1+p^2)^{\frac{1}{n-1}} \cos\left[\frac{2}{n-1} \operatorname{arctg} \frac{1}{p}\right], \tag{7}$$

where M is the reduced atom mass, T is the temperature in atomic units, $\Gamma(x)$ is Euler's gamma-function.

In the case $n = 6$, $p = 0$, the van der Waals damping constant is obtained within the Weisspopf-Lindholm approximation:

$$\gamma_{WL} = 7.901 \frac{N}{V} C_6^{2/5} \left(\frac{8T}{\pi M} \right)^{3/10}, \tag{8}$$

where p is the parameter of inelastic collisions, $0 \leq p \leq 1$.

The value of γ_0 for $p \neq 0$ and $p = 0$, in particular, reads:

$$\gamma_0/\gamma_{WL} = (1+p^2)^{\frac{1}{n-1}} \frac{\cos\left(\frac{2}{n-1}\mathrm{arctg}\frac{1}{p}\right)}{\cos\frac{\pi}{n-1}}. \tag{9}$$

The ratio is greater than 1. Therefore, account of inelastic collisions increases the damping constant and the increase is considerable.

In order to estimate the contribution of post van der Waals interactions, let us write the expansion of the Eq. (9) in powers of temperature:

$$\gamma/\gamma_0 = 1 + \sum_{k \geq 1} A_k (T/T_0)^{\frac{k}{n-1}}, \tag{10}$$

where coefficients A_k are determined from constants of post van der Waals interactions.

The repulsion forces are also found to contribute into the damping constant. The contribution is estimated approximately as follows: $\gamma > N\pi a_0^2 < v > /V = N2\pi a_0^2 (8T/\pi M)^{1/2}/V$, where a_0 is the scattering length which is of atomic diameter order.

Let us make a quantitative estimate of inelastic collisions contribution to γ. In the case of van der Waals interactions ($n = 6$) for the maximal contribution of inelastic collisions ($p = 1$), elementary calculations yield: $\gamma_0(p = 1)/\gamma_{WL} = 1.3504$. This estimate of inelastic collisions contribution can partially improve the artificial increase mentioned above of the damping constant inherent in analysis of star spectra.

Let us estimate numerically the values of A_k. Consider an example of sodium atom in the solar atmosphere, where hydrogen atoms at the temperature of $T = 1000$ K serve as perturbing particles. Thus, for the Na-H system we find: $A_1 = 0.452, A_2 = 0.295, \gamma/\gamma_0 > 1.2$. Even such not so high temperature in the star atmosphere scale causes significant increase of γ. For $T = 6420$ K, $\gamma/\gamma_0 > 1.32$.

The contribution of repulsion forces for the discussed above Na-H system for $a > 2.6$ Å yields $\Delta A_1 > 0.595$, which results in $\gamma/\gamma_{WL} > 1.92$ for $T = 1000$ K. For $T = 6420$ K, $\gamma/\gamma_{WL} = 2.206$.

By means of the proposed explicit expressions for the damping constant, one can make a numerical estimation of the constant for various temperatures in the solar photosphere attached to various values of inelastic collisions parameter. Computations, performed on the base of different methods of the damping constant investigations [2] are well-consistent with our theoretical computations.

Thus, our new results are consistent with the data of the other authors. They can be used for explanation of experimental studies of Fraunhofer's lines, in particular, for determination of chemical elements content in the solar atmosphere. The theoretical method proposed for the damping constant calculations can be generalized for the case of star atmospheres.

REFERENCES

[1] *Vakarchuk I. O., Rykalyuk R. E., Yankiv-Vitkovska L. M.* // JPS.–1998.–**2**, N 1.

[2] *Yankiv-Vitkovska L.* // Visnyk of Lviv Univ. Physical Ser.–1999.–N 32.

WAVE PROPAGATION IN THE SOLAR ATMOSPHERE

E. V. Khomenko

Main Astronomical Observatory, NAS of Ukraine
27 Zabolotnoho St., 03680 Kyiv, Ukraine
e-mail: khomenko@mao.kiev.ua

The theory of a wave propagation in the solar atmosphere has been applied to study peculiarities in the wave behaviour above granules and intergranular lanes. We introduced oscillations into a 3D snapshot of the theoretical time dependent solar model atmosphere. NLTE synthesis of the two solar lines was performed: the relatively strong Fe I 5324 Å which is formed over all the photosphere and a weaker Ni I 6768 Å line. The latter is widely used in helioseismology. We compared our modeling with the high spatial resolution observations obtained from the ground using VTT on Tenerife and from space using SOHO/MDI. We conclude that many differences in oscillations above granules and lanes can be induced by variations of the physical conditions in these structures.

MODEL OF OSCILLATIONS

We solved analytically the standard hydrodynamical equations of mass, momentum and energy conservation under assumptions that there are no magnetic field; viscosity and thermal conduction terms can be omitted; the effects of solar rotation are negligible; to the 0^{th} order the atmosphere is plane parallel, horizontally homogeneous and in radiative equilibrium. The matter is described by equation of state neglecting ionization effects. The effects of radiative relaxation are taken into account by using the Newtonian cooling approximation. The motion is restricted to one dimension. Solution of the system of partial differential equations was obtained by approximating the atmosphere as a series of isothermal layers each of a given thickness (10 km) moving with a constant velocity. In each layer we linearized the fundamental equations with:

$$T = T_0 + T_1, \quad P = P_0 + P_1, \quad \rho = \rho_0 + \rho_1, \quad V = V_0 + V_1, \tag{1}$$

where T_0, P_0, ρ_0 are unperturbed model temperature, pressure and density and V_0 is convective velocity. The system has an exponential solution at the fixed frequency of the form of a plane wave.

$$V_1,\, T_1,\, \rho_1 \;\sim\; e^{z(1\pm k_i)} e^{\pm i k_r (\pm t V_{ph} - t V_0 - z)}, \tag{2}$$

where $V_{ph} = \omega / k_r$ is the phase velocity of the wave, k_r and k_i are the real and imaginary parts of the vertical wave number k_z. Upward and downward solutions were selected by choosing the corresponding sign of k_r and k_i.

A wave crossing the boundary between the layers experiences a partial reflection due to the discontinuity of atmospheric parameters. At the interface between two layers the conditions of total pressure and total velocity continuity take place. These conditions lead to the expression for reflection and transmission coefficients in the form [2]:

$$\tilde{R} = \frac{V_r}{V_i} = \frac{(C_t - C_i) + g/\omega(\rho_u - \rho_l)}{(C_r - C_r) - g/\omega(\rho_u - \rho_l)}, \tag{3}$$

$$\tilde{T} = \frac{V_t}{V_i} = \frac{(C_r - C_i)}{(C_r - C_r) - g/\omega(\rho_u - \rho_l)}, \tag{4}$$

where C is the complex proportionality coefficient between velocity and pressure perturbations; subscripts i, r and t denotes respectively the incident, reflected and transmitted waves; ρ_u and ρ_l are densities of the upper and lower layer. We calculated the $\tilde{R}$ and $\tilde{T}$ for all the 102 boundaries in our model. The resulted velocity perturbation was computed as a superposition of all the reflected waves and transmitted wave. The waveforms for the thermodynamic perturbations T_1/T_0 and ρ_1/ρ_0 and P_1/P_0 were obtained from the polarization relations.

Variations of the thermodynamical quantities were introduced into the model atmosphere and then profiles of the Fe I 5324 Å and Ni I 6768 Å lines were synthesized. In the present study we utilize a snapshot of the 3D model atmosphere from the most recent numerical simulations by Asplund *et al.* [1]. We use the interpolation from the original simulated box which has physical dimensions of $6.0 \times 6.0 \times 3.8$ Mm with nearly 1.0 Mm being located above the continuum optical depth unity. For the line profiles calculations we chose one slice from the snapshot and extracted a set of 50 1D granular and intergranular models by taking the height-variation of the thermodynamical quantities at the selected gridpoints of the slice.

We computed the line intensity using the formal solution of the time–dependent radiative transfer equation for the case of the moving atmosphere perturbed by oscillations. Line profiles were synthesized using NLTE departure coefficients found for each of the 50 models from the self–consistent solution of the kinetic and radiative transfer equations [3]. Time series of Fe I 5324 Å and Ni I 6768 Å line profiles were synthesized with the overall computational time of 1 wave period ($\sim$ 5 minutes). Initial amplitude of the wave perturbation was chosen equal to $V_0 = 100$ m s^{-1} at height 0 km, with the period being 270 s.

Then we restored velocity and intensity oscillations at 11 levels of the computed Fe I line profiles applying the method described by Stebbins and Goode [5]. For the case of Ni I line profile series we computed MDI velocity and intensity oscillations in the way described by Scherrer *et al.* [4].

OBSERVATIONS

We compared the results of our computations with the high spatial resolution observations obtained both from the ground with VTT on Tenerife and from space with SOHO/MDI.

The ground observations were carried out with the 70-cm German VTT at the Observatorio del Teide, Tenerife, in August 1996. The CCD images contain the photospheric line Fe I 5324 Å. The observed area (0.38×89 arcsec^2) was placed near the quiet solar disk centre. The spectrograms were taken every 9.3 s during 31 minutes. The spatial resolution of this observations was about 0.5 arcsec.

For our study we have used also the 58 min of the filtragrams from the "Line Profile Study" campaign on October 11, 1999 taken in the high resolution mode of MDI with 0.625 arcsec/pixel. The observed area was 160×160 arcsec^2 large, virtually quiet and placed near the disc center. We constructed a proxy for velocity, line and continuum intensity signals using the filtragrams.

CONCLUSIONS

The main results of our study are the following:

(i) amplitudes of velocity and intensity oscillations change with granulation contrast at all height layers of the photosphere. At average, the amplitudes are larger above the dark intergranular lanes.

(ii) velocity–intensity phase shift above the lanes is 30 degrees lower than above granules.

(iii) velocity oscillations at the lower layers of the atmosphere lead oscillations at the upper layers in intergranular lanes. In granules the phase shift is nearly zero.

We summarize that many differences in oscillations above granules and intergranular lanes can be reproduced with the help of the wave propagation theory. Even if all the initial and boundary conditions are equal at $H = 0$, oscillations above granules and intergranular lanes turn out to have different amplitudes and phases at the upper layers of the photosphere. This changes are caused by modulation of the propagating wave by the variations in the physical conditions in these structures.

Acknowledgements. We would like to thank R. Kostik for the helpful discussions. Special thanks to M. Asplund for the kind permission to use 3D model atmosphere for the purposes of our study. We are grateful to A. Kosovichev for the help with MDI data processing and useful suggestions.

REFERENCES

[1] *Asplund M., Nordlund A., Trampedach R., et al.* Line formation in solar granulation. I. Fe line shapes, shifts and asymmetries // Astron. and Astrophys.–2000.–**359**, N 2.–P. 729.

[2] *Marmolino C., Severino G., Deubner F.-L., et al.* Phases and amplitudes of acoustic–gravity waves. II. The effect of reflection // Astron. and Astrophys.–1993.–**278**, N 2.–P. 617–626.

[3] *Shchukina N. G., Trujillo Bueno J.* The iron line formation problem in 3D hydrodynamical models of solar-like photospheres // Astrophys. J.–2001.–**550**, N 2.–P. 970–987.

[4] *Scherrer P. H., Bogart R. S., Hoeksema J. T., et al.* The solar oscillations investigation – michelson doppler imager // Solar Phys.–1995.–**162**, N 1.–P. 129–188.

[5] *Stebbins R. T., Goode P. R.* Waves in the solar photosphere // Solar Phys.–1987.–**110**, N 1.–P. 237–253.

REFLECTION AND SCATTERING OF ACOUSTIC WAVES IN THE SOLAR ATMOSPHERE

S. N. Osipov

Main Astronomical Observatory, NAS of Ukraine
27 Zabolotnoho St., 03680 Kyiv, Ukraine
e-mail: osipov@mao.kiev.ua

The reflection and transmission complex coefficients for various heights are calculated for MACKKL model of the solar atmosphere for approximation of the isothermal solar atmosphere stratified by gravitation. The anomalous behaviour of amplitude and phase of reflected and transmitted waves along acoustic cut-off frequency line in height-frequency diagram and reflection phase jump at temperature minimum height are shown. The simulation of primary upward velocity wave and superposition fields of velocities of the reflected and scattered waves at different layers are carried out. For the chromosphere the superposed reflected and scattered velocity fields demonstrate the negative phase dependence as the primary upward velocity wave.

INTRODUCTION

The reflection of acoustic waves was considered for the first time by Mein and Mein [4] to account for standing waves pattern in the solar chromosphere. The reflection conditions for the isothermal atmosphere were analyzed in [3, 2]. At the discontinuity between uniform temperature layers the wave motion must satisfy pressure and velocity continuities. The frequency dependence of reflection coefficients have been studied by a number of authors (*e.g.*, [2, 5]). However, the height dependence of reflection and transmission are known more worse. Moreover, the effects of compound superposition of waves reflected at different heights were not studied. Our goal was, therefore, to study the amplitude and phase behaviour of downward reflected wave fields.

REFLECTION COEFFICIENTS AND REFLECTED WAVES SIMULATION

We have computed the reflection (R) and transmission (T) complex coefficients for various heights for the MACKKL model of the solar atmosphere [1] by using equations derived in [2]. The vertical wavenumber k_z and radiative decay time were calculated according to [6] and [7], respectively.

The reflection and transmission coefficients demonstrate the anomalous behaviour of the amplitude and phase at acoustic cut-off frequency. The reflection phase jump at the temperature minimum height is confirmed. There is a difference in the above coefficients for various directions of propagation.

The analytic form for the simulation of monochromatic plane stationary wave propagation is known (*e.g.*, [3]). Such an expression for a wave reflected at the fixed height is known as well [2]. We consider the superposition of waves partially reflected at different heights. Therefore, the downward velocity can be written as

$$V_z^{dn} = V_z^{up} \int_z^{\infty} R_z^{up} \prod_z^{z_r} \left(T_z^{dn} T_z^{up}\right) \exp\left(-2i \int_z^{z_r} k_z dz\right) dz_r, \tag{1}$$

where V_z^{up} is the complex velocity amplitude of the primary upward wave, z is the height of the atmosphere, index up and dn refer to the velocity, reflection and transmission of the upward and downward propagation, respectively.

Moreover, we insert the waves scattering in our speculations. It is necessary to account for the waves, changing the direction of propagation without phase modification. As the first approximation we considered isotropic scattering without height dependence. The approach is very rough, but in such a way we can estimate scattering effects. Eq. (1) adopts to

$$V_z^{dn} = V_z^{up} \int_z^{\infty} G(1 - \frac{5}{6}S)^{2(n_{z_r} - n_z)} \prod_z^{z_r} \left(T_z^{dn} T_z^{up}\right) \exp\left(-2i \int_z^{z_r} k_z dz\right) dz_r, \tag{2}$$

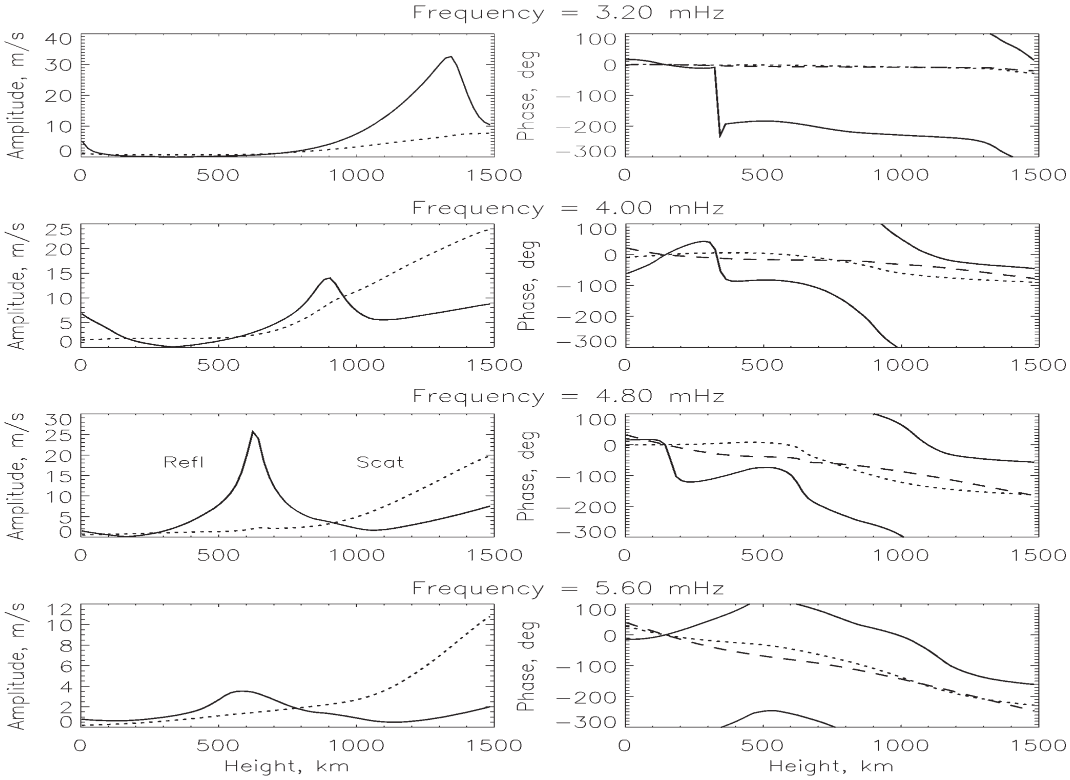

Figure 1: The height dependence of the amplitudes and phases of downward reflected and scattered velocity waves. Solid lines refer to reflected waves, dotted lines to scattered waves and dashed curves to primary upward waves

where G corresponds to R_z^{up} for the reflected waves and corresponds $S/6$ for the scattered waves, S is the scattering coefficient.

Results of numerical simulations are shown in Figure 1. For the chromosphere the superposed reflected and scattered downward velocity fields demonstrate the tendency of negative phase dependence as a primary upward velocity wave V_z^{up}. It is rather unexpectedly because a single wave reflected at any fixed height demonstrates a positive downward phase course. This result may be explained by strong damping of downward waves. Therefore, the reflected wave field phase behaviour is designated by phase of a primary wave at the little higher heights. For the photosphere the phases of the reflected waves are more intricate.

The reflected waves amplitudes has a sharp maxima at layers below the acoustic cut-off frequency heights. The location of the reflected waves phase jump generated at the temperature minimum is reduced with frequency and occurs at heights from 150 to 350 km. The reflected waves amplitudes at these heights are insignificant. The scattered waves mask this jump and prevent the phase jump being observed.

REFERENCES

[1] *Maltby P., Avrett E. H., Carlsson M., et al.* A new sunspot umbral model and its variation with the solar cycle // Astrophys. J.–1986.–**306**, N 1.–P. 284-303.

[2] *Marmolino C., Severino G., Deubner F.-L., et al.* Phases and amplitudes of acoustic-gravity waves II. The effects of reflection // Astron. and Astrophys.–1993.–**278**.–P. 617–626.

[3] *Mihalas D. and Mihalas B. W.* Foundation of Radiation Hydrodynamics.–New York: Oxford Univ., 1984.

[4] *Mein N., Mein P.* Velocity waves in the quiet solar chromosphere // Solar Phys.–1976.–**49**.–P. 231–248.

[5] *Kumar P.* Excitation and Damping of Solar Acoustic Oscillation // Solar Convection and Oscillations and their Relationship / Eds Pijpers F. P., *et al.*–New York, 1997.–P. 161–169.

[6] *Souffrin P.* Hydrodynamics of an Atmosphere Disturbed by a Subjacent Turbulent Convective Zone // Ann. Astrophys.–1966.–**29**.–P. 55–101.

[7] *Spiegel E. A.* The Smoothing of temperature Fluctuations by Radiative Transfer // Astrophys. J.–1957.–**126**.–P. 202–207.

A METHOD FOR DETERMINATION OF ELECTRON CONCENTRATION IN DENSE SPACE PLASMA

E. R. Venglinsky

Astronomical Observatory, Taras Shevchenko National University
3 Observatorna St., 04053 Kyiv-53, Ukraine

A method for determination of the intensity distribution of the recombination emission on the Balmer series limit versus logarithm of the electronic concentration $\log n_e$ is presented. Both the Stark and Doppler effects are taken into account. The core of the correspond integral equation is tabulated in a compact form for the wide range of $\log n_e$ (from 9 to 15) and the most probable velocities of hydrogen atoms (from 0 to 3000 km/s).

The spectral range of the Balmer series limit is highly attractive to plasma diagnostics. Is was shown that observed distribution of intensity in the Balmer precontinuum provides an opportunity for determination of the electron concentration inhomogeneity [1]. The Balmer precontinuum intensity is meant to be an interpolated curve through points of minimum intensities between the high Balmer members. The method proposed by [1] is not quite correct and overestimates the values of the electron concentration by factor 3 [2]. In this paper the redetermine plasma diagnostics is presented.

One can obtain the differential distribution of the recombination emission at the Balmer series limit, $I_{c,2}$ with respect to logarithm of the electron concentration, $\log n_e$, solved numerically equation

$$I(\lambda) = \int \varphi(\lambda, \log n_e, \xi)\, I'_{c,2}\, d\log n_e, \tag{1}$$

where $I(\lambda)$ – observed precontinuum intensity, λ – the wavelength of electromagnetic radiation, ξ – the most probable velocity of hydrogen atoms, $\varphi(\lambda, \log n_e, \xi)$ – precontinuums calculated for fixed values of n_e. These precontinuums were calculated as a result of overlapping of the hydrogen line wings broaden by the Stark and Doppler effects. Since the Doppler effect is negligible in the line wings, the constant value of ξ is assumed for a whole object. ξ is determined from low members of Balmer series. The special choice of coordinates allows to tabulate the function $\varphi(\lambda, \log n_e, \xi)$ in a compact form.

Let us consider the precontinuum as a function of parameter $x = \log(\lambda - \lambda_{c,2})$, where $\lambda_{c,2}$ is the limit of the Balmer series (in Angstroms). Take the value $\bar{x}$ equal to x which satisfies the condition $I(\bar{x}) = I_{c,2}/2$, where the precontinuum intensity, $I(x)$, equals the half of intensity at the series limit. Then if spectral lines are broaden by the Doppler effect only

$$\bar{x}(\xi) = -3.1367 + 0.67 \log \xi, \tag{2}$$

where ξ is in cm/s.

Table 1: Profiles of precontinuums

$x - \bar{x}$	α					$x - \bar{x}$	α				
	0.5	0.2	0	–0.2	–0.5		0.5	0.2	0	–0.2	–0.5
–0.20	1.00	1.00	1.00	0.99	0.99	0.08	0.22	0.20	0.19	0.18	0.18
–0.16	1.00	1.00	0.99	0.97	0.96	0.12	0.15	0.13	0.11	0.09	0.09
–0.12	1.00	0.99	0.94	0.92	0.91	0.16	0.10	0.09	0.06	0.04	0.03
–0.08	0.95	0.89	0.84	0.82	0.81	0.20	0.07	0.06	0.04	0.02	0.01
–0.04	0.75	0.71	0.68	0.67	0.67	0.30	0.03	0.02	0.01	0.01	0.00
0	0.50	0.50	0.50	0.50	0.50	0.40	0.01	0.01	0.01	0.00	0.00
0.04	0.33	0.33	0.33	0.33	0.33	0.60	0.00	0.00	0.00	0.00	0.00

For the Stark effect

$$\bar{x}(n_e) = -1.827 + 0.265 \log n_e. \qquad (3)$$

The precontinuum profiles depend on the parameter $\alpha = \bar{x}(n_e) - \bar{x}(\xi)$. We calculated these dependencies and presented them in Table 1.

The calculations including both the Stark and Doppler effects are presented in Table 2. To determine the value $\bar{x}(n_e, \xi)$ the dependence of $\beta = \bar{x}(n_e, \xi) - \bar{x}(\xi)$ on α is given in Table 2 as well.

Table 2: Dependence of parameter β on α

α	β	α	β	α	β	α	β
0.6	0.602	0.3	0.316	0.0	0.090	–0.3	0.011
0.5	0.504	0.2	0.229	–0.1	0.048	–0.4	0.005
0.4	0.409	0.1	0.152	–0.2	0.024	–0.5	0.002

Tables 1 and 2 together with Eqs. (2)–(3) allow to obtain the functions $\varphi(\lambda, \log n_e, \xi)$ for a numerical solution of Eq. (1) in wide the range of values n_e (from 10^9 up to 10^{15} cm^{-3}) and ξ (from 0 up to 3000 km/s).

REFERENCES

[1] *Kurochka L. N.* Registration of macro- and microinhomogeneities of plasma density in astrophysical objects // Kinematics and Physics of Celestial Bodies.–1991.–**7**, N 4.–P. 25–29.

[2] *Venglinskij E. R.* Determination of a electron concentration inhomogeneity in the quiet solar prominence // Kinematics and Physics of Celestial Bodies.–1997.–**13**, N 3.–P. 47–50.

THE SUN AMONG THE STARS

I. E. Vasiljeva

Main Astronomical Observatory, NAS of Ukraine
27 Zabolotnoho St., 03680 Kyiv, Ukraine
e-mail: vasil@mao.kiev.ua

Various methods have been used in the observation, analysis and interpretation of solar analogue candidates. These are photometric observations in various photometric bands, spectrophotometric observations, method of synthetic photometry (in order to obtain magnitudes, color indices and other photometric data). We present the results of a comparative study of the Sun and the stars using all of these methods. The 4183 stars were involved into analysis. As a result we have presented a new list of candidates into solar analogues.

COMPARATIVE STUDY

- Determination of Sun's colour indexes in photometric systems *UBV, uvby, UVBRI, Vilnius, DDO.*
- Selection of stars having solar-like colour indexes in stated above photometric systems.

Sun's colour indexes were determined by method of synthetic photometry.

$$CI_{1-2} = -2.5 \log \frac{\int I(\lambda)\phi_1(\lambda)d\lambda}{\int I(\lambda)\phi_2(\lambda)d\lambda} + K_{1-2},$$

where CI – colour indexes; $I(\lambda)$ – energy distribution in star/solar spectrum; $\phi_n(\lambda)$ – filter n transmission curve; K_{1-2} – normalization factor.

Method of synthetic photometry more than once was applied for Sun's colour indexes determination in photometric systems *UBV, WBVR, Vilnius UPXYZVS.* But for all these systems, the 5 nm spectral resolution for stars used for the calibration is expliciently insufficient. The errors caused by insufficient spectral resolution are shown in Fig. 1.

We use energy distributions presented in [1] for stars with spectral resolution of 0.45 nm and in [2, 3, 4, 5] for the Sun with the same resolution. As the data used for given energy distribution in stellar spectra are presented for 351—742.7 nm wavelength range, it imposes limitation on filters in use.

Results of determination of pseudo-observed Sun's colour indexes in different photometric systems are presented in Table 1. Stars having colour indexes similar to solar ones were selected from photometric catalogues in each photometric systems. The final list (Table 2) have included stars presented in no less than in four such samplings.

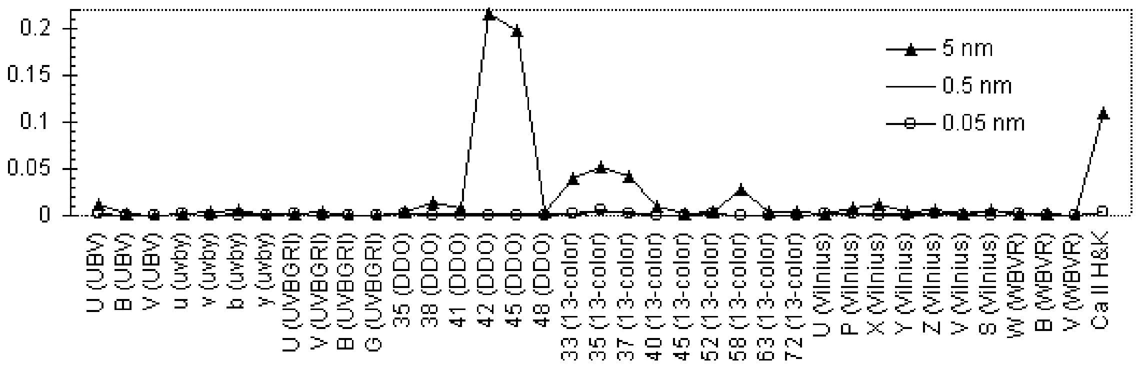

Figure 1: Errors caused by insufficient spectral resolution

Table 1: Color indices for the Sun

	[2]	[3]	[4, 5]
$B-V(UBV)$	0.654	0.684	0.653
$b-y(uvby)$	0.405	0.433	0.417
$m1(uvby)$	0.210	0.211	0.206
$C4548(DDO)$	1.017	1.018	1.012
$C4245(DDO)$	0.636	0.663	0.647
$C4142(DDO)$	0.006	0.029	0.024
$V-R(UBVRI)$	0.589	0.570	0.548
$P-X(Vilnius)$	0.684	0.659	0.644
$Y-Z(Vilnius)$	0.336	0.348	0.335
$Z-V(Vilnius)$	0.218	0.231	0.229
$V-S(Vilnius)$	0.594	0.580	0.552

Table 2: Selected stars

HD	Sp	[6]	HD	Sp	[6]	HD	Sp	[6]	HD	Sp	[6]
1461	G0V-G5V	+	26756			111812	G0III	+	181655		+
1835	G2V	+	27685	G4V—G7V	+	112257	G2III—G2V	+	186408	G2V—G3V	+
3628	G2V		28068	G1V—G5V	+	114613	dG3	+	186427	G2V—G5V	+
6582	G0IV-G8V		28099	G8V	+	115617	G5V—G6V	+	187923	G0V—G2V	+
10700	G8V-VI		28992	G5V		117176	G2.5V—G5V	+	190771	G2V—G5IV	
11397	G6IV-V		29621	G5V	+	126053	G1V—G2V	+	195564		+
13783	G8V		30246	G5V	+	135101	G5V	+	199960		+
20619		+	30495	G2V	+	140538	G5V	+	212330		+
20630	G5V	+	34411	G0IV—G2V	+	146233	G1V—G2V	+	216777	G6V	
20766	G2V	+	53705	G3V	+	157347	G5IV—G5V	+	217014	G2.5IV—G5V	+
20794	G5V—G8V	+	65583	G8V		159222	G2V—G5V	+	222143		
24341	G1V		102365	G5V	+	160691	G5V	+			
26736	G3V	+	111395	G5V—G7V		161239	G2III—G0IV				

Stars from Hardop list [6] are marked with crosses. Stars from the list [6] previously considered (such as HD 34411, HD 53705, HD 111395, HD 117176, HD 126053) were excluded as ones not obeying the selection criteria.

SUMMARY

The separate Sun's colour indexes were determined in five photometric systems *UBV, uvby, UVBRI, Vilnius, DDO.*

Stars having solar-like colour indexes in stated above photometric systems were taken from photometric catalogues.

Taking into account that such a list comprises stars of different spectral classification, we suggest that it is necessary to tighten a photometric selection criteria for stars, which are candidates in solar analogues.

REFERENCES

[1] *Jacoby G. H., Hunter D. A., Christian C. A.* A Library of Stellar Spectra // Astrophys. J. Suppl. Ser.–1984.–**56**.–P. 278.

[2] *Arvesen J. C., Griffin R. N. Jr., Pearson B. D. Jr.* Determination of Extraterrestrial Solar Spectral Irradiance from a Research Aircraft // Appl. Opt.–1969.–**8**.–P. 2215–2232.

[3] *Neckel H., Labs D.* The solar radiation between 3300 and 12500 A // Solar Phys.–1984.–**90**.–P. 205–258.

[4] *Burlov-Vasiljev K. A., Gurtovenko E. A., Matvejev Yu. B.* New absolute measurements of the solar spectrum 310-685 nm // Solar Phys.–1995.–**157**.–P. 51–75.

[5] *Burlov-Vasiljev K. A., Matvejev Yu. B., Vasiljeva I. E.* New measurements of the Solar Disk-Center Spectral Intensity in the Near IR from 645 nm to 1070 nm // Solar Phys.–1998.–**177**.–P. 25–40.

[6] *Hardorp J.* The Sun among the stars // Astron. and Astrophys.–1982.–**105**.–P. 120–132.

RADIO EMISSIONS OF THE SUN–LIKE STARS

E. P. Abranin[1], I. Yu. Alekseev[2], L. L. Bazelyan[1], A. I. Brazhenko[3], R. E. Gershberg[2], V. N. Lisachenko[1], V. N. Mel'nik[1], N. I. Shakhovskaya[2]

[1] *Institute of Radio Astronomy, NAS of Ukraine*
4 Chervonopraporna St., 61002 Kharkiv-2, Ukraine
e-mail: melnik@ira.kharkov.ua

[2] *Crimean Astrophysical Observatory, Ministry of Ukraine for Education and Science*
Naukove, 98409 Crimea, Ukraine

[3] *Poltavskaya Gravimetrical Observatory, NAS of Ukraine*
Poltava, Ukraine

The results of flare star observations at UTR-2 are presented. The brightness temperatures of radio bursts observed are found and their possible radiation mechanisms are discussed.

For the first time, the decameter radio emission from a flare of red dwarf star V371 Orion has been detected at 19.7 MHz by Slee *et al.* [1]. It was observed at the beginning of the flare and had flux 23000 Jy that corresponded to the very high brightness temperature $10^{20}\,K$ (for comparison, the Sun maximum brightness temperatures of sporadic radio emissions are $T_b < 10^{16}\,K$). This fact gave rise to doubts.

In this paper we present the results of the observations and their analysis of dMe flare stars at 20 and 25 MHz frequencies. The observations were carried out episodically from 1986 to 1998 with UTR-2 radiotelescope [2, 3]. They were accompanied by photometric patrol in U–band at AZT-11 telescope of the Crimean Astrophysical Observatory. The photometric data of the other observatories were used in same cases as well. Durations of observations for each star were in the range from 4 to 6 successive hours and were a little larger than the rotational period of a star. To discriminate against terrestrial interferences the DKM radio observations were carried out simultaneously by two separate beams at two different frequencies in ON/OFF regime. Besides, spectral and temporal features of signals, polarity of radiotelescope response and correlation DKM radio bursts with optical flares were taken into account.

In 1986–1989 the efforts to detect sporadic DKM bursts from the flare star EV Lac were made by means of radiometers with temporal resolution of ≈ 5 s. From time to time single short bursts and groups of such bursts were observed. On September 12, 1986 and September 13, 1986 the rate of appearance of the bursts was about twice or three times higher than that for free optical flare intervals. It is significant that there were three flares with apparent U–magnitude 0.5–0.75 mag on September 12, 1986 and one powerful flare with 2.8 mag on September 13, 1986. Later the two two-channel radiometers with the temporal resolution of 0.2 s were used for observations of short bursts at 20 MHz and 25 MHz. On September 1–2, 1992 the four groups of short bursts from EV Lac star were observed [3]. Durations of the bursts were < 1 s and their flux densities were in the range $250 - 900$ Jy. All these events were accompanied by optical flares and observed on the decay phase of the flare.

As to other six stars only one burst from YZ CMi was detected for 210 hours of observations. The burst was observed 2.5 minutes before optical flare in the B–band detected at the Stephanio Observatory (Greece). Observations were conducted during 2 hours and 44 minutes simultaneously in the optical and radio bands and these events were the only ones detected. The probability of accidental coincidence of radio burst and optical flare is very low. So, we conclude that the burst had a stellar origin. It should be noted that although optical stellar flares usually precede radio bursts by some minutes opposite situations they have been detected as well.

The very high brightness temperatures of the stellar bursts found at DKM range, $T_b = (1-6) \times 10^{18}\,K$, need coherent mechanism of radiation, plasma or electron cyclotron maser emissions [4].

Electron cyclotron maser emission can be observed on the condition that the optical depth of the region with negative absorption is $\tau > 1$ and high gyroresonance layers are transparent. Assuming the electron density $n_e = 10^{12}$ cm^{-3}, the magnetic field in the footpoints of a magnetic loop where radio emission coming from is equal to 4 G and the radiation occurs at the third harmonic of Larmor frequency with the brightness temperature $10^{19}\,K$. The estimations show that absorption in the fourth gyroresonance layer is very strong (the optical depth is $\tau = 30$). Thus, the brightness temperature of leaving emission will be much lower than that observed.

For plasma mechanism of radio emission the high brightness temperature can be explained under condition that the efficiency of the conversion of the plasma waves into electromagnetic waves is maximum, the velocity of the electron beam equals to 10^{10} cm/s and electron beam density is $n_b/n = 10^{-4}$.

So, we conclude that the most probable mechanism of radio emission for bursts from flare stars at decameter wavelengths is the plasma one.

Acknowledgements. This work was made possible in part due to INTAS (grants N 96-0183 and N 97-1964).

REFERENCES

[1] *Slee O. B., Solomon L. H., Patson G. E.* Radio emission from flare star V371 Orion's // Nature.–1963.–**199**, N 4897.–P. 991–994.

[2] *Abranin E. P., Alekseev I. Yu., Avgoloupis S., et. al.* Coordinated observations of the red dwarf flare star EV Lac in 1994 and 1995 // Astron. and Astrophys. Transactions.–1998.–**17**.–P. 221–262.

[3] *Abranin E. P., Bazelyan L. L., Mel'nik V. N.* On a decameter radioemission of flare star EV Lac // Ann Geo. Res. (Space and Planet. Sci.).–1994.–**12**, Part III, Supp. III.–P. 686.

[4] *Mel'nik V. N.* On the cyclotron maser mechanism of the decametric emission from flare stars // Kinematics and Physics of Celestial Bodies.–1994.–**10**, N 5.–P. 63–65.

MULTIDIMENSIONAL RADIATION TRANSFER IN THE INHOMOGENEOUS STELLAR ATMOSPHERES

M. I. Stodilka

Astronomical Observatory, Ivan Franko National University of Lviv, Lviv, Ukraine
e-mail: sun@astro.franko.lviv.ua

We solved 2D non-equilibrium radiation transfer problem for different atmosphere models. 2D NLTE radiation transfer problem is solved by using multigrid techniques. On the each grid the solution is found by the accelerated Λ–iteration method. For the formal solution of the radiation transfer problem the short characteristics method is used; we also used the linear convergence improvement procedure. The solution convergence is fast for all the atmosphere models that were tested. We considered influence of NLTE effects on the Fe I equivalent width spatial variations over granular intergranular layers in the solar atmosphere.

PROBLEM DEFINITION

Stellar atmosphere is a totality of different nonuniformities (granulation, spots, *etc.*), therefore, it is impossible to describe radiation transfer in the limits of the one dimensional model. The problem may be solved by the differential methods. But these methods are not well in the case of the model atom with a great number of levels. In such cases the iterative methods are to be used that deal with an approximate operator, but give exact solutions. Our approach is based on the complex method elaborated by Bueno and Auer for multilevel 3D problem [1].

Let us consider 2D plane parallel model of the atmosphere. All the parameters are given in the knots of 2D grid. Using the radiation transfer equation provided a known source function one can find after some algebra relationship between intensities at different points of the atmosphere:

$$I_\nu = I_{\nu 0}\exp(-\Delta\tau_\nu) + S_\nu(1-\exp(-\Delta\tau_\nu)) + \Delta S_\nu/\Delta\tau_\nu * (1-(\Delta\tau_\nu+1)\exp(-\Delta\tau_\nu)), \tag{1}$$

where $I_{\nu 0}$ is the initial intensity, $\Delta\tau_\nu$ is the optical depth between these points, S_ν is the source function.

The radiation transfer equation connects intensity with level populations $\mathbf{n}$ which satisfy statistical equilibrium equations. The equations may be written in a matrix form:

$$\mathbf{A}\mathbf{n} = \mathbf{b}. \tag{2}$$

Matrix $\mathbf{A}$ is generated by radiative and collisional transitions. All the elements of the vector $\mathbf{b}$ with the exception of the last are equal to zero. Then the solution of both equations is:

$$J_\nu = \Lambda_\nu S_\nu, \tag{3}$$

J_ν is an averaged intensity. It is a simple Λ–iteration procedure. Its convergence is slow. To improve convergence we shall represent Λ–operator as a sum of explicit and approximate operators. In a latter operator representation the line core photons leave the transfer and the solution convergence is faster. It is an accelerated Λ–iteration. Then for the intensity we obtain:

$$J_\nu^{(n)} = J_\nu^{(n-1/2)} + a_\nu S_\nu^{(n)} - a_\nu S_\nu^{(n-1)}, \tag{4}$$

where n is a number of iterations; $J_\nu^{(n-1/2)} = \Lambda_\nu S_\nu^{(n-1)}$; a_ν are the coefficients, obtained from Equation (1). For the multilevel problem Equations (4) are inserted into Equations (2). The system of equations becomes linear:

$$\mathbf{A}^*\mathbf{n} = \mathbf{b}. \tag{5}$$

Equations (5) are preconditioned. The iteration procedure convergence is linear; calculations require many iterations. Number of iterations is much less when the acceleration procedure is used. We used Ng acceleration.

The radiation transfer problem is solved by using multigrid techniques. This approach guarantees the convergence to the true solution since long periodical oscillations of the solution are filtered and the convergence becomes essentially improved. The solution on each grid is found by the accelerated Λ–iteration. For the formal solution of the radiation transfer equation the short characteristics method is used; we also used the linear convergence improvement procedure.

RESULTS

We tested our program using different plane-parallel atmosphere models: a) uniform solar models: HSRA, VAL; b) Maltby solar spot model, which corresponds spectral class K0 star; c) nonuniform: quasistationary single scale and non-stationary multiscale solar granulation models. As these comprehensive tests showed the convergence of the solution is fast enough and the described techniques allow to study inhomogeneous astrophysical plasma.

In this paper we present some results of the Fe I lines spatial variations calculations for non-stationary solar granulation [2] using the above mentioned techniques. The Fe I lines calculation is made for 21-level model of the atom, which consists of 18 Fe I levels, two Fe II lower levels and the ground Fe III level. We took into account doppler shifts of the absorbtion coefficient profiles along ray propagation, so profiles are asymmetric and spread by nonthermal velocities.

We shall consider results just only for one weak line λ 671.032 nm. For the line the largest discrepancy between LTE and NLTE equivalent widths exists. The line has a small EPL and is formed in the deep atmosphere layers. In Figs. 1a, 1b we show dependence of equivalent widths (NLTE and LTE) from continuum intensity (normalized by its middle value) for 19 minutes sequence of 38 models; a spatial smearing is not accounted. As we see, in the granular NLTE effects (due to photoionizations and bound-bound transitions) sufficiently

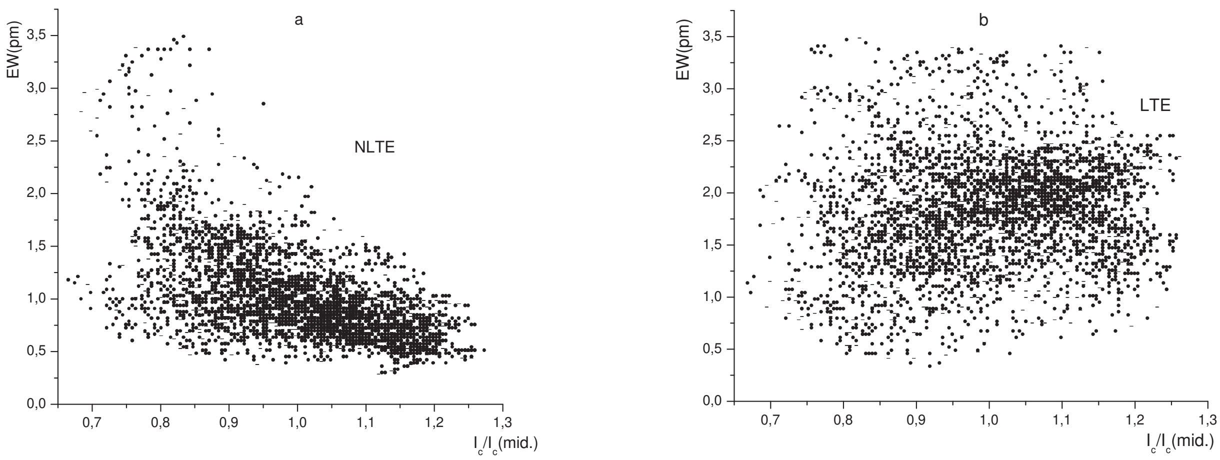

Figure 1: Dependence of equivalent widths from intensity for λ 671.032 nm Fe I

decrease equivalent widths. In the region of low continuum intensity the equivalent width variability increases, that's because of line spread by descending flows and adiabatic gas rarefication. In the LTE conditions the Fe I equivalent widths get stronger in the granular and are weaker in the intergranular regions, while in the more realistic nonequilibrium conditions that dependence has a small negative slope. The upper cooler layers over bright granular regions are more ionized by UV radiation than the hotter intergranular layers, so Fe I levels are more depleted in the granular, lines are formed deeper and have smaller equivalent widths. NLTE effects smooth spatial fluctuations of equivalent widths. In Fig. 1a one can see separation of the dependence into two branches in the intergranular region. Such a separation is determined by the overdone interaction of descending flows in 2D models. The other lines show the similar dependences.

REFERENCES

[1] *Auer L., Fabiani Bendicho P., Trujillo Bueno J., et al.* Multidimensional radiative transfer with multilevel atoms: I. ALI method with preconditioning of the rate equations // Astron. and Astrophys.–1994.–**292**, N 1.–P. 599–615.

[2] *Gadun A. S., Solanki S. K., Johannesson A.* Two-dimensional simulation of solar granulation: description of technique and comparison with observations // Astron. and Astrophys.–1999.–**350**, N 3.–P. 1018–1034.

STATION OF OPERATIVE FORECAST OF SOLAR ACTIVITY USING RADIO OBSERVATIONS: NEW PROJECT

L. I. Tsvetkov, M. M. Posdnjakov, M. A. Mironov

Crimean Astrophysical Observatory, RT-22, Katsiveli, 98688 Crimea, Ukraine
e-mail: tsvetkov@rad.crimea.ua

The project goal:

1. Solar flares diagnostics.
2. Research of global oscillations of the Sun.

The RT-22 CrAO is an unique Ukrainian radio telescope used for the observations of the Sun, galactic and extragalactic sources of space radiation in the spectral range of 2–35 mm. A monitoring of the solar activity together with of space weather observations is possible only in an alert regime, as the RT-22 CrAO participates in the European VLBI and the majority of the time is assigned to the observations under the astrophysical and geodynamic programs.

With a purpose of the monitoring of the solar activity by radio methods the small radio telescopes intended for daily measurements of the solar radio emission in cm- and mm-ranges are necessary. The choice of a range is stipulated by the circumstance that sources of outbursts occur in the solar chromosphere where the centimeter and millimeter radiation is generated.

In previous years the RT-22 CrAO participated in the international programs on the solar activity research. The new outcomes on study of global oscillations of the Sun, on diagnostics of solar flares, under the definition of physical conditions in the activity complex are obtained.

The helioseismological researches are extremely important for developing a model of the interior structure of the Sun. New measurements of the global oscillations spectrum of the Sun by radio astronomical methods carried out in the laboratory of the radio astronomy of CrAO, testify to comparability on an exactitude of a wireless and optical methods.

The research of the global oscillations of the Sun concern to the basic trends of a science and have an applied value.

Now it is evident that the upgrading of the receivers intended for the observations of the radio radiation of the Sun is necessary. A life expectancy of these receivers is calculated to be twenty years.

Essence of the project:

1. The RT-22 CrAO radio telescope in the multiwaves regime can be equipped with a package of reception modules at 17.0, 15.4, 13.3, 10.6, 8.6, 5.8 GHz frequencies.
2. The RT-2 solar centimeter radio telescope can be equipped with reception modules at 5.8, 10.6, 15.0 GHz frequencies.
3. The RT-1 solar millimeter radio telescope can be equipped with receivers at 30, 45, 90 or (22, 36, 45) GHz frequencies.
4. The extension of the frequency range of the RT-3 radio telescope receivers using two radiometers at 2.85 and 2.5 GHz.

Novelty: the realization of this radio astronomical project will allow Ukraine to enter adequately into the Solar Observation Optical Network.

Perspectives of the project realization:

The RT-22 CrAO is arranged with the perfect control system permitting to realize all the necessary conditions for solar observations. The assembly of an antenna with diameter of 2.5 m is completed in 2000 year. Laboratory of the radio astronomy of the CrAO arranges a precision parabolic mirror by the diameter of 90 cm and rotary device from a package of a Siberian Solar Radio Telescope. There are some institutes in Ukraine where the microwave amplifiers for these radio astronomical complex can be made.

SPECIFIC OF A ROTATION OF THE SOLAR MEAN MAGNETIC FIELD DURING CYCLE 21 AND 22

U. M. Leyko

Astronomical Observatory, Taras Shevchenko National University
3 Observatorna St., 04053 Kyiv-53, Ukraine
e-mail: leiko@aoku.freenet.kiev.ua

Taking into consideration Severny' idea on magnetic asymmetry the two time series for N(+) and S(−) components have been derived from time series of Stanford measurements of the solar mean magnetic field, cycle 21 and 22. Separative investigation of N(+) and S(−) component spectra furnishes more correct explanation of the origin of the spectrum peaks of time series of the solar mean magnetic field measurements and definition of the features of the largescale magnetic structures rotation. Pronounced differences of the power and form of the peaks in spectra of both cycles point out to the different space–time organization of the largescale magnetic structures during each cycle. The difference of N(+) and S(−) component spectra within each cycle is caused by magnetic asymmetry.

The rotation of the solar largescale magnetic field is a vital problem of present-day solar physics. The first investigations have revealed faster magnetic structure rotation than that of photospheric plasma at all latitudes except equator [1]. It was obtained two periods, 27^d and 28^d–29^d, of rotation of the largescale magnetic structures at latitude zone near equator [2]. Sun-as-a-star measurements of the solar magnetic field (the solar mean magnetic field, SMMF) were begun by Severny *et al.* in 1968 at the Crimean Astrophysical Observatory and two rotation periods $26\overset{d}{.}8$ and $27\overset{d}{.}6$ were obtained. These periods were interpreted by Syverny as rotation periods of N(+) and S(−) largescale magnetic structure [3].

Taking into consideration Severny' idea on magnetic asymmetry the curve of Stanford SMMF measurements, cycles 21 and 22, have been inspected and brought out its asymmetric about the line of zero value of the magnetic field. The SMMF time series seems to be a sum of two independent time series. These are series of the plus SMMF values (N(+) component of SMMF) and minus SMMF values (S(−) component of SMMF). Therefore, it is necessary to investigate each of these series separately. Two series of such a length as original one were formed as following. In original series the minus values were replaced by zero and derived the series of N(+) component. Replacing the plus values by zero the series of S(−) component are derived. For further investigation of series the spectral analysis method was applied. The results are shown in Fig. 1.

There are power spectra of SMMF, cycle 21 and 22, of whole (original) series (top panel), of S(−) component series (middle panel and N(+) component series (bottom panel) in 13^d–15^d and 25^d–31^d period range in Fig. 1. Significant distinctions between the spectra of whole series manifestate the features of SMMF rotation during each cycle. The 21 and 22 cycles spectra are different from each other by number of peaks, their power and form thus it points out to the different space–time organization of magnetic structures during timescale in each cycle. One can say that there were five latitude zones of the predominant concentration of the largescale magnetic structures for cycle 21 and three such zones for cycle 22.

It is known the higher latitude of the largescale magnetic structure the a magnetograf signal is smaller. For this reason and in consequence of differential rotation the power of rotation period decreases with the increasing of a value of its period. This rule is observed for spectrum peaks of the 22 cycle both for whole series and components series. But spectrum peaks of cycle 21 don't follow this rule. Two powerful peaks in spectrum of S(−) component point out to S(−) structures concentrated mainly at two latitude zones during 21 cycle. The powers of these peaks are approximately equal. This is an evidence of predominant S(−) magnetic structures concentration at the latitude zone rotated with $28\overset{d}{.}2$ period. In spectrum of N(+) component $26\overset{d}{.}93$ peak is exceptional one. Therefore, the zone of predominant concentration of N(+) structures had $26\overset{d}{.}93$ rotation period. These conclusions are in a good agreement with results of [4]. During the 22 cycle all three spectra are alike. The peaks of both component have the same periods, but their form is different. Magnetic asymmetry had another character during cycle 22.

The very powerful peaks of $10\overset{y}{.}27$ (21 cycle) and $8\overset{y}{.}7$ appeared in long period range of the spectrum of N(+) and S(−) components. The value of this peaks is the same for both component during one cycle, but their

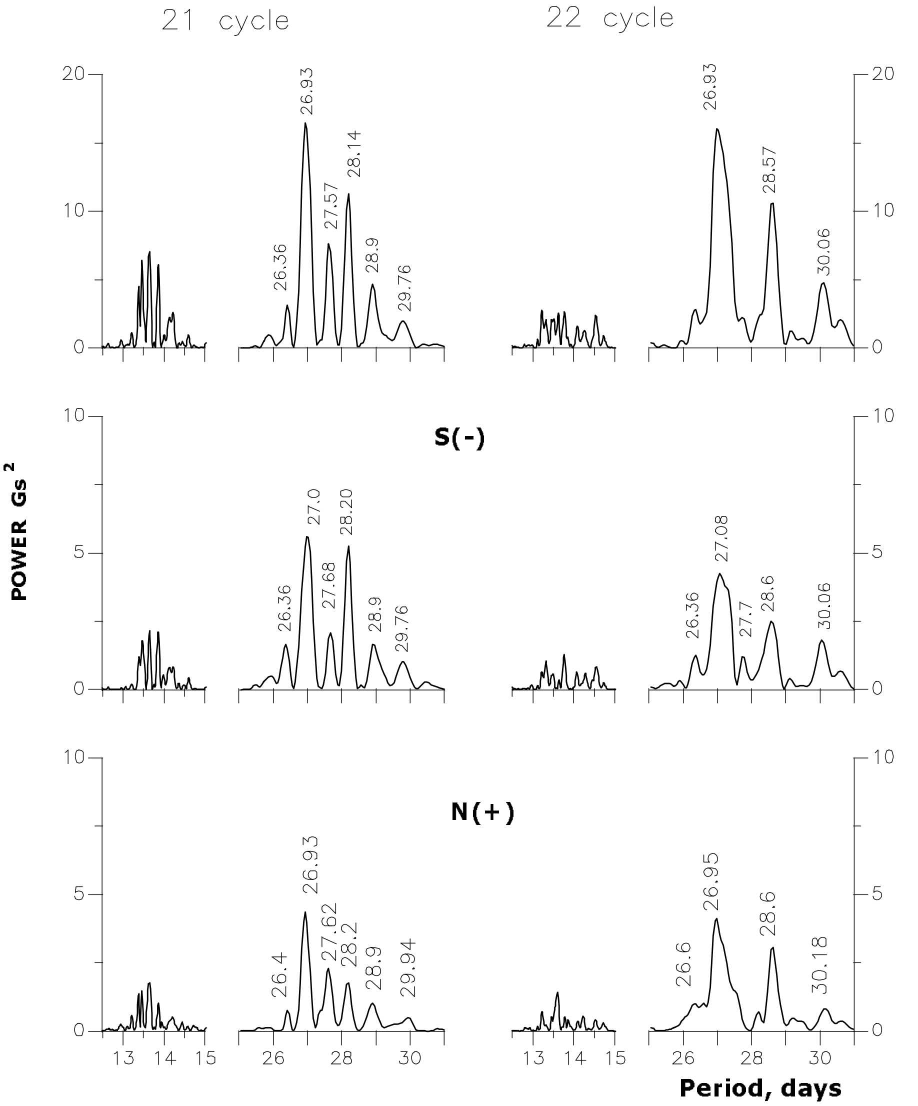

Figure 1: The spectrums of the solar mean magnetic field, 21 and 22 cycle

powers are different. These peaks are very weak in the spectra of whole series of both cycles.

Separative investigation of N(+) and S(−) component spectra furnishes more correct explanation of an origin of the spectrum peaks of time series of SMMF measurements and defines the features of the magnetic field rotation.The number and form of the spectrum peaks are caused by space-time organization of the largescale magnetic structures. Both cycles spectra are characteristically different in number of peaks, their power, a form and value of the rotation period pointing to the different space–time organization of largescale magnetic structures during each cycle. The difference of N(+) and S(−) component spectra within each cycle is caused by magnetic asymmetry.

REFERENCES

[1] *Wilcox J. M., Howard R.* Differential rotation of the photosheric magnetic field // Solar Phys.–1970.–**13**, N 2.–P. 251–260.

[2] *Bumba V.* The largescale magnetic fields on the Sun // The problem of the solar activity.–1979.–P. 50–74.

[3] *Severny A. B.* The polar fields and time fluctuations of the general magnetic field of the Sun // Solar magnetic fields: IAU Symposium N 43 / Ed. R. Howard.–Dordreht, 1971.–P. 675–693.

[4] *Antonucci E., Hoeksema J. T., Scherer P. H.* Rotation of the photospheric magnetic fields: a north–south asymmetry // Astrophys. J.–1990.–**360**, N 1.–P. 296–304.

RESULTS OF ASTRONOMICAL AND ECOLOGICAL OBSERVATIONS DURING THE TOTAL SOLAR ECLIPSE AUGUST 11, 1999

K. I. Churyumov, V. G. Ivanchuk, Yu. V. Dubrovsky, V. I. Solonenko

Astronomical Observatory, Taras Shevchenko National University
3 Observatorna St., 04053 Kyiv-53, Ukraine
e-mail: klim@aoku.freenet.kiev.ua

We present some results of astronomical and ecological observations during the total solar eclipse Aug. 11, 1999.

The solar corona Aug. 11, 1999 was observed close to the maximum phase of the 11-year solar activity (SA) cycle and had the maximum shape. It consists of the numerous powerful and thin rays with mainly radial orientation, as well as of a considerable number of big and bright prominences (Fig. 1). It is necessary to note that the angle of divergence of the East-fan of rays is bigger than that of the West-fan. There is an evidence of a significant E/W asymmetry of the solar corona. The brightness distribution shows the solar corona near the spherical-symmetrical shape. Only near the South pole there is a less bright region, where the polar coronal hole occurs. This fact and some others circumstances point to the noticeable N/S asymmetry of the solar corona. The high-latitude rays of the N–hemisphere (especially in the NE sector) are inclined in the direction of the N–pole and

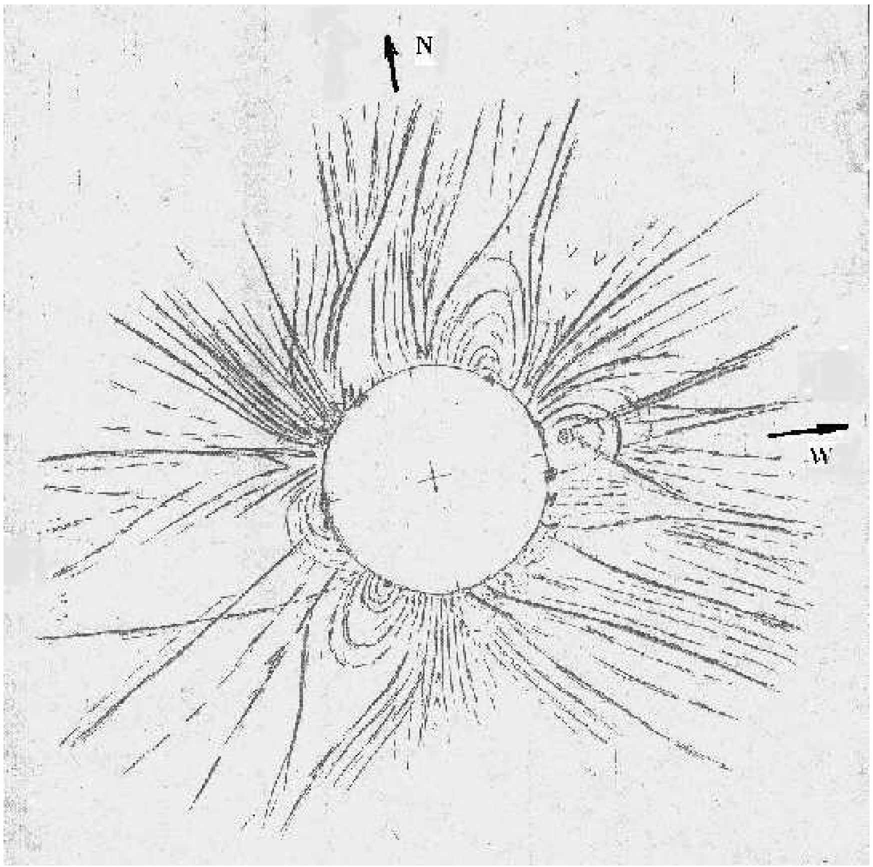

Figure 1: The structural drawing of the solar corona Aug. 11, 1999

the high-latitude rays in the SW–sector of the South hemisphere are inclined in the direction of the solar equator. All this shows that the N–hemisphere is more active than the S–hemisphere. It means that the N–hemisphere has developed its maximum shape. We note that the sunspot activity in the N–hemisphere for all the branch of rise of SA including 1999 $\Sigma W_N/\Sigma W_S = 1.15$ is considerably higher than for the S–hemisphere. According to our forecast [1] the 23rd cycle must be characterized by domination of the spot activity and threefold polarity reversing for the S–hemisphere. It follows that the maximum of the present 23rd cycle of SA will take place in the N–hemisphere in the middle of 2000 and in the S–hemisphere the maximum of SA will take place probably in the middle of 2001. A rather interesting peculiarity of the solar corona Aug. 11, 1999 is the existence of a sabre-like thin double ray on the NE–limb (at PA $= 50°$). It is close to the peculiar center of "repulsion" for the fan of rays of the E–limb. Similar rays also existed in certain coronas over the outburst active regions of the Sun and were connected with the phenomena of the transient of the coronal plasma of the "ray-type". Therefore, probably both this ray and the sharp divergence of the rays on the E corona are connected with the existence of the transient ejection. In the region of the NW–quadrant and near the W–equator on the best mages of the corona a rather sharp transequatorial arc is detected. We think that it is tied with development of the coronal mass ejection (CME) detected by the cosmic coronograph C2 of Lasco SOHO Aug. 11/12, 1999. The CME velocity in the inner corona was very low (12 km/s) and in the outer corona the CME velocity was moderate ($170 - 200$ km/s). Comparison of the Aug. 11, 1999 solar corona structure with the model of the corona magnetic field shows their good similarity *to the Micic–Linker model.*

Ecological observations (Bulgaria, Mount Charakman) show that the behaviour of birds began to change 24 min before the second contact T_2. 4 min before T_2 all swallows flew to their nesting-places and 2 min before T_2 the sound activity of insects began to decrease and at the time of T_2 ceased.

With some delay the rate of fall of the air temperature reflected decreasing illumination. After the third contact it was $6° - 7°$ C. 4 min after T_3 (11:42 UT) the first sounds of insects were heard and 11 min after T_3 the first swallows appeared. Full restoration of the sound ground of insects took place 20 min later T_3 and a usual distribution of birds for the locality took place 60 min after T_3. Change of birds and insects activity which was close to the total eclipse phase is mainly determined by the illumination factor (coefficients of correlation are 0.93 and 0.66). Probably, the behaviour of animals is determined by breach of the normal photoperiod and awareness of a sudden danger in the eclipse conditions [2].

REFERENCES

[1] *Ivanchuk V., Babiy V.* // Inform. Bull. UAA.–1998.–N 12.–P. 30.

[2] *Churyumov K., Ivanchuk V., Dubrovs'ky Yu.* The solar corona in the objective // Visnyk of National Academy of Sciences of Ukraine.–1999.–N 9.–P. 53–56.

THE TOTAL SOLAR ECLIPSE PHOTOELECTRIC OBSERVATIONS FOR THE SUN'S DIAMETER DETERMINATION

V. Danylevsky

Astronomical Observatory, Taras Shevchenko National University
3 Observatorna St., 04053 Kyiv-53, Ukraine
e-mail: vdan@observ.univ.kiev.ua

The solar eclipse observations allow to trace the solar diameter in time scales of years to hundreds of years. There are solar diameter values obtained near edges of the path of the total eclipses from visual and videotapes observations. However, it is necessary to use the model of the solar atmosphere with the solar optical diameter measurement in order to obtain correct diameter values. Visual eclipse observations technique does not allow to do it, whereas photoelectric total solar eclipse observations allow to do it by the use of the solar limb intensity model. The 1991 and 1999 total solar eclipses were observed by photoelectric method. An estimation of the solar visible disk semidiameter was done from the data 1991 eclipse observations, and for distance 1 AU it was equal to (959.70 ± 0.12) arcs. The data of the August 11, 1999 eclipse observations are in processing and there is a hope to obtain the solar disk semidiameter with error less than ±0.1 arcs.

The solar eclipse observations allow to trace the solar diameter in a time scale of years to hundreds of years. It is important both for estimations of the effect of the possible variations in a solar luminosity on the earth climatic changes and for computations of solar convective zone models. There are data obtained near edges of the path of a total eclipse from visual and videotapes observations [6]. These data series cover about three centuries but contain 10 values of the solar semidiameter only (9 of them were obtained in 20th century). These data as well as some new published results obtained by other techniques show a possibility of the solar diameter variations, and separately, these variations may be associated with the cycle of the solar activity [10, 14]. But the atmospherical effects such as seeing and blurring have an influence on the ground-based solar diameter measurements, whereas the solar diameter values obtained from the solar eclipse observations do not depend on these atmospherical effects. Besides, these results are especially important because their accuracy may be increased if the Sun's and Moon's ephemeris and lunar limb profile data are improved. However, as it was shown in [1] it is necessary to use the model of the solar atmosphere (as a model of the solar limb intensity distribution) with the solar optical diameter measurement in order to obtain correct diameter values. But the visual eclipse observations technique does not allow to model the solar limb intensity distribution.

Photoelectric observations of the total solar eclipses were performed earlier for determining some geodetic parameters and solar limb brightening [7, 11, 12]. These observations consisted in the registering of the photometer signals, which are proportional to solar crescent light, together with respective instants of a time. Also it has been shown how the observed solar crescent luminosity at any instant depends on the semidiameters and angular separations of the centres of the Sun's and Moon's visible disks at that instant and solar limb brightening function as well [7, 9, 11].

For the first time, the photoelectric observations of the July 11, 1991 total solar eclipse were performed in Baia California Sur, Mexico, by Ukrainian scientists [8] to determine the Sun's angular diameter. Special photometers, designed in the Astronomical Observatory of the Taras Shevchenko National University of Kyiv, were used [2]. The observations were performed at three sites within the path of the total eclipse near its northern edge and at one site near centre of the path of the total eclipse. At the northern edge the observers were located along the line approximately normal to the edge with intervals of about 1.5–2 km. Analysis of the observational data [3] showed that the chromosphere light and the lunar limb shape irregularities influenced significantly on the light curves of the eclipses. To determine the solar disk semidiameter from these observational data, a theoretical light curve was described by an integral equation similar to the Kopal's equation and fitted with the least squares method to each observational light curve, and the solar disk semidiameter was one of the best-fit parameters. The theoretical light curve includes the Moon's limb irregularities corrections, but it is supposed that the solar limb is sharply delineated and the intensity function at the limb is linear, and the chromosphere light was taken into account partially only. Nevertheless, the solar angular semidiameter averaged from four values is equal to (959.70 ± 0.12) arcs and it is in a good agreement with the standard value and with data obtained visually and with video techniques near the edges of the path of the total eclipses [4, 5].

For the second time, the photoelectric observations of the total solar eclipse were performed on August 11, 1999 in Romania by the expedition of the Taras Shevchenko National University in Kyiv [13]. The observations were completed at six sites: at three sites near northern edge and at three sites near southern edge of the path of the total eclipse within its. The observers were located along the line approximately normal to the edges with intervals from of about 2 km to about 5 km. These observations consisted in registration of the photometer signals from the full Sun's disk before the 1st and after the 4th contacts, and signals from the solar crescent light including a total phase, together with respective instants of a time. To perform these observations the photometers were improved. Specifically, they were upgraded to measure the brightness of the sky near the Sun's apparent disk (the solar aureole brightness). The measurements of a solar light and sky brightness are necessary to reduce an influence of both individual parameters of photometer and atmospheric extinction at the observational sites on the observational light curves. Unfortunately, this kind of a measurement was not performed during 1991 eclipse observations. Besides, photometer's time scale was adjusted to UTC scale. The time interval was equal to 1/1024 s and errors of timing the data were not more than 0.5 s in UTC scale.

It was necessary to determine coordinates of the observational sites with errors not more than of about ± 1 arcs. During 1999 eclipse they were determined by GPS personal navigator with adequate accuracy, but during 1991 eclipse they were determined with errors of about 0.1 arcmin [8]. The data of the August 11, 1999 eclipse observations are in processing and we hope to obtain the solar disk semidiameter with error less than ± 0.1 arcs.

REFERENCES

[1] *Brown T. M., Christensen-Dalsgaard J.* Accurate Determination of the Solar Photospheric Radius // Astrophys. Lett.–1998.–**500**, N 2.–P. L195–L198.

[2] *Buzduga Yu. A., Okulov S. M., Kleshchonok V. V.* The Expeditionary Photometer for Observation of Solar Eclipse // Visnyk Kyivskoho Universytetu. Astronomia.–1992.–**6**.–P. 92–95.

[3] *Danylevsky V. O.* The 1991 July 11 solar eclipse photoelectric observations data processing and light curves analysis // Visnyk Kyivskoho Universytetu. Astronomia.–1999.–**35**.–P. 51–59.

[4] *Danylevsky V. O.* The solar diameter determination from data of the 1991 July 11 solar eclipse photoelectric observation // Contr. Astron. Obs. Skalnate Pleso.–1999.–**28**, N 3.–P. 201–209.–(Proceedings of the 1999 solar eclipse workshop).

[5] *Danylevsky V. O.* Preliminary results of the solar diameter determination from data of the 1991 July 11 solar eclipse observations // Visnyk Kyivskoho Universytetu. Astronomia.–1999.–**35**.–P. 59–65.

[6] *Fiala A. D., Dunham D. W., Sofia S.* Variation of the solar diameter from solar eclipse observations, 1715 – 1991 // Solar Phys.–1994.–**152**.–P. 97–104.

[7] *Goldstein A. A.* On the reduction of photoelectric observations of a total solar eclipse // Georgetown College Observatory.–1954.–**Monograph 3**.–P. 1–108.

[8] *Gurtovenko E. A., Tel'nyuk-Adamchuk V. V., Okulov S. M. et al.* Observation of solar eclipse on 11 July 1991 in Mexico for solar diameter determination // Astron. Tsirk.–1991.–N 1550.–P. 29–30.

[9] *Kopal Z.* The distribution of brightness at the extreme limb of the sun // Astrophys. J.–1946.–**104**.–P. 60–74.

[10] *Noel F.* Variations of the apparent solar semidiameter observed with the astrolabe of Santiago // Astron. and Astrophys.–1997.–**325**.–P. 825–827.

[11] *Osawa K.* Distribution of the brightness at the extreme limb of the sun observed at the solar eclipse on May 9, 1948 // Ann. Tokyo Astron. Observ. Second Ser.–1951.–**3**, N 2.–P. 53–85.

[12] *Rosen W. A., Poss H. L.* Solar limb brightening at the extreme limb from photoelectric eclipse observations // Solar Phys.–1982.–**78**.– P.17–37.

[13] *Tel'nyuk-Adamchuk V. V., Efimenko V. M., Danylevsky V. O. et al.* Observing of total solar eclipse on August 11, 1999 by scientific expedition of Kyiv University // Visnyk Kyivskoho Universytetu. Astronomia.–2000.–**36**.–P. 41–47.

[14] *Yoshizawa M.* Solar-radius variations over a solar cycle observed with the Tokyo photoelectric meridian circle // Dynamics and Astrometry of Natural and Artificial Celestial Bodies / Eds I. M. Wytryszczak, J. H. Lieske, R. A. Feldman.–Netherlands: Kluwer Acad. Publ., 1997.–P. 551–556.

RADIO EMISSION OF THE SUN AT DECAMETER WAVELENGTHS

E. P. Abranin, L. L. Bazelyan, V. N. Mel'nik

Institute of Radio Astronomy, NAS of Ukraine
4 Chervonopraporna St., 61002 Kharkiv-2, Ukraine
e-mail: melnik@ira.kharkov.ua

Radio astronomical study of the solar corona and radio emission of the Sun at decameter wavelengths (12 – 30 m) have been carried out in Ukraine at the largest decameter UTR-2 radio telescope since 1972. The aims of this study are thermal and sporadic radio emission of the Sun and the scattering of radiation by the solar corona. The main aims of the theoretical research is to study various properties of the radio emission of the Sun. The particular interest of this study is construction of physical models for solar Type III bursts. The drift rate, observed time profile, brightness temperature of F– and H–components, *etc.* are explained in the framework of these models.

The scattering properties of the solar corona in the range from $5\,R_\odot$ to $25\,R_\odot$, the thermal emission of the quiet Sun, as well as the local sources of Slowly Varying Component (SVC) of the solar radio emission and sporadic decameter radio emission of the Sun are investigated with UTR-2. The principal results can be formulated as follows:

1. The extended radio sources occultation by the corona was observed by Bazelyan *et al.* [7]. For the first time the two dimensional images of these sources were obtained. The angular width of the observed power spectrum at $\lambda > 10$ m increases with λ, somewhat less rapidly than λ^2. This fact can be explained in a non-uniformity solar corona [7, 8].

2. Two-dimensional brightness distribution of the quiet Sun is observed within decameter wavelengths for the first time. It is shown that variations of these distributions have a solar origin [3].

3. Observations of the quiet Sun [1] and the extended radio sources better agree with a corona model with radial prolongated structures.

4. The enhanced radio emission of the quiet Sun is usually observed for tens of minutes after intensive Type III bursts. In our opinion this is an effect of isotropization of one-dimensional Langmuir waves generated by electron streams [11].

5. In spite of some reports there is no convincing evidence for the existence of local SVC sources at decameter wavelengths [6].

6. Observations of Type IIIb-III bursts at 25, 12.5, and 6.25 MHz support a fundamental–harmonic burst pairs interpretation [5].

7. Observations of solar storms of Type III bursts show that

a) the F–harmonic takes place when the emitting region is at the disc center and

b) the H–harmonic is realized [2] when the region is near the limb.

8. Deceleration of fast electron streams responsible for Type III bursts has been investigated at decameter wavelengths. This phenomenon is due to a collissionless mechanism [10].

9. Diffusive stria bursts and their chains of Type IIIb have been searched for. It can be shown after observations of stria burst position that they are superposition of ordinary H–harmonic stria bursts and their echoes [9].

Type III bursts are the most bright manifestation of a solar sporadic radio emission in the wide frequency range from $100 - 300$ MHz to $20 - 30$ kHz with the most pronounced peculiarities at decameter wavelengths ($10 - 25$ MHz). The fast electrons propagating along magnetic field lines with velocities about 0.3 c are considered to be responsible for their radio emission. To the last time there is no satisfactory Type III burst theory for lack of theory of the electron propagation through the coronal plasma [15]. Recently, the gas-dynamic theory of propagation of electron beams in plasma was proposed [13, 14]. According to this theory fast electrons move in coronal plasma as a beam-plasma structure that consists of electrons and Langmuir waves. The structure velocity is constant that explains an invariability of drift velocity of Type III bursts. The nonlinear processes ($l + i = l + i$) of scattering Langmuir waves on plasma ions are turned out to limit the maximum velocity of beam-plasma structure that equals to approximately 0.3 c. This is the cause of Type III burst drift velocity. Langmuir waves of beam-plasma structure taking into account in processes ($l + i = t + i$) and ($l + l = t$) give emission at fundamental and harmonic frequencies. In these cases the brightness temperatures of radio emission of beam-plasma structure T_{bps} are equal to $10^{13}\,K$ and $10^{15}\,K$, respectively. As Type III burst seems to consist of large number of separate microbursts for the brightness temperature of the burst we have $T_{III} = fT_{bps}$, where f is the filling factor [16]. For $f = 10^{-2} - 10^{-3}$ [16], at decameter wavelengths we derived values $10^{11} - 10^{12}\,K$ closed to the observed ones. So, the gas-dynamic theory of electron propagation in plasma allows to explain the main properties of Type III bursts [12].

Acknowledgements. This work was partially supported by INTAS (grant N 96-0183 and N 97-1964).

REFERENCES

[1] *Abranin E. P., Bazelyan L. L., Bistrov M. V., et al.* Quasiperiodic fluctuations of solar radio emission at decameter wavelengths // Pis'ma Astron. Zh.–1978.–**4**.–P. 559–567.

[2] *Abranin E. P., Bazelyan L. L., Rapoport V. O., Tsybko Ya. G.* Variations of Type III burst parameters during a decametric solar storm // Solar Phys.–1980.–**66**.–P. 333–341.

[3] *Abranin E. P., Bazelyan L. L.* The structure of Type II supernova remnant G160.5 +2.8(HB-9) observed at $\lambda = 12$ m // Astrophys. and Space Sci.–1982.–**83**.–P. 299–306.

[4] *Abranin E. P., Bazelyan L. L., Tsybko Ya. G.* Harmonic relation of Type IIIb-III solar radio bursts in 6.25, 12.5 and 25 MHz octaves // Solar Phys.–1984.–**91**.–P. 377–389.

[5] *Abranin E. P., Bazelyan L. L.* Decameter radiation of the quiet Sun // Preprint IRE.–1986.–**304**.–42 p.

[6] *Bazelyan L. L.* A search for local sources of the s-component at decameter wavelengths // Solar Phys.–1987.–**112**.–P. 107–112.

[7] *Bazelyan L. L., Braude S. Ya., Megn A. V.* Scattering of the decametric wavelength radiation of the Crab Nebula by the Solar corona // Astron. Zh.–1970.–**47**.–P. 188–197.

[8] *Bazelyan L. L., Sinitsin* Scattering of radio waves from cosmic sources in the solar corona // Solar Phys.–1971.–**17**.–P. 129–142.

[9] *Bazelyan L. L., Goncharov N. Yu., Zaitsev V. V., et al.* Frequency and time splitting of decameter solar radio bursts. II. Chains // Solar Phys.–1974.–**39**.–P. 223–235.

[10] *Bazelyan L. L., Goncharov N. Yu., Zaitsev V. V., et al.* Colissionless deceleration of fast electron streams in the solar coronal plasma // Solar Phys.–1977.–**52**.–P. 141–153.

[11] *Bazelyan L. L., Mel'nik V. N.* Post-burst increase of brightness temperature of the Sun at decameter wavelengths // Kinematics and Physics of Celestial Bodies.–1990.–**6**, N 6,–P. 87–89.

[12] *Mel'nik V. N.* Properties of Type III bursts in gas-dynamic model of propagation of electron beams in plasma // Kinematics and Physics of Celestial Bodies.–1991.–**7**, N 3.–P. 59–68.

[13] *Mel'nik V. N.* Gas-dynamic description of electron flux flying off in plasma // Ukr. Fiz. Zh.–1990.–**35**, N 6.–P. 871–877.

[14] *Mel'nik V. N., Lapshin V. I., Kontar E. P.* Propagation of a monoenergetic electron beam in the solar corona // Solar Phys.–1999.–**184**, N 2.–P. 353–362.

[15] *Melrose D. B.* Particle beams in the solar atmosphere // Solar Phys.–1990.–**130**.–P. 3–18.

[16] *Melrose D. B., Dulk G. A.* Implications of Liouville's Theorem on the Apparent Brightness Temperatures of Solar Radio Bursts // Solar Phys.–1988.–**116**.–P. 141–156.

NONLINEAR INTERACTION OF MHD WAVES AND SOLAR CORONA HEATING

A. K. Yukhimuk[1], **V. M. Fedun**[2], **E. K. Sirenko**[1], **Yu. M. Voitenko**[1,3], **A. D. Voytsekhovskaya**[1]

[1] *Main Astronomical Observatory, NAS of Ukraine*
27 Zabolotnoho St., 03680 Kyiv, Ukraine
e-mail: yukhimuk@mao.kiev.ua, sirenko@mao.kiev.ua

[2] *Department of Astronomy and Space Plasma Physics, Taras Shevchenko National University*
6 Glushkova, 03022 Kyiv, Ukraine
e-mail: fedun@astrophys.ups.kiev.ua/fedun@mao.kiev.ua

[3] *Centre for Plasma Astrophysics, K.U.Leuven, Belgium*
e-mail: Yuriy.Voytenko@wis.kuleuven.ac.be

The nonlinear parametric interaction of Alfvén waves with magnetosonic and ion-acoustic waves is considered on the basis of two-fluid magnetohydrodynamics. A nonlinear dispersion relation describing three-wave interaction, instability growth rate have been calculated and estimated. The analysis of theoretical results shows that kinetic effects in the Alfvén waves (the finite ion Larmour radius) are essential for the parametric interactions of waves.
Nonlinear parametric processes studied in the paper could take place in the solar coronal loops, where plasma parameter is small. The products of the decay – magnetosonic and ion-acoustic waves, can effectively heat the coronal plasma owing to rapid dissipation.

INTRODUCTION

Magnetohydrodynamic waves play an important role in the dynamics of the Earth magnetosphere, solar wind and atmosphere of the Sun. The long-period geomagnetic pulsations observed in the Earth's magnetosphere have been considered as MHD Alfvén waves (Nishida, 1980; Volokitin and Dubinin, 1989). The satellite observations show that the most part of turbulent pulsations are the Alfvén and magnetosonic waves in the solar wind (Belcher, 1971). They are thought to play an essential role in the solar wind heating. The MHD waves can provide a source of energy for corona heating. Alfvén waves have enough energy for heating of coronal loops (see, *e.g.*, Goossens, 1994 and references therein). But they are slowdamped. This is the reason why Alfvén wave can't heat coronal loops directly, and the problem arise: how the energy can be transferred from waves to plasma particles. The ion-acoustic and magnetosonic waves are rapid damped waves. Therefore, if the propagating Alfvén wave decays into ion-acoustic and magnetosonic waves, they can transfer rapidly their energy to particles due to dissipation. In the paper (Uchida, 1974; Wentzel, 1974) it was shown that the processes of formation of acoustic waves from Alfvén waves are effective in the region, where $V_A/V_s - 1/30 - 30$. The dissipation of wave energy arises on distances which are comparable with the length of coronal loops. Nonlinear interaction between Alfvén and ion-acoustic waves was considered for the case of linear dispersion , *i.e.*, without accounting thermal effect (finite Larmor radius of proton). But in the magnetosheric and coronal plasma thermal effects play an important role. Taking into account the thermal effects leads to nonlinear dependence of frequency from wavenumber, which is essential for nonlinear wave interaction.

In the present work we consider nonlinear parametric interaction of Alfvén wave with the ion-acoustic and magnetosonic waves.

BASIC EQUATION

It is assumed that Alfvén wave with finite amplitude propagates in homogeneous magnetized plasma ($\vec{B}_0 = B_0\vec{e}_z$):

$$\vec{E}_0 = (E_{0x}\vec{e}_x + E_{0z}\vec{e}_z)\exp i(-\omega_0 t + \vec{k}_0\vec{r}) + c.c., \tag{1}$$

where the frequency and wave vector are related by equality:

$$\omega_0^2 = k_{0z}^2 V_A^2(1 + t\mu_i). \tag{2}$$

Here $\mu_i = k_{0x}^2 \rho_i^2, \rho_i = V_{Ti}/\omega_{Bi}$ – proton Larmor radius, $\omega_{Bi} = eB/m_i c$ – ion cyclotron frequency, $t = T_e/T_i$. Our governing equations are a set of two-fluid MHD equation:

$$\frac{\partial \vec{v}_\alpha}{\partial t} = \frac{1}{m_\alpha}(e_\alpha \vec{E} + \vec{F}_\alpha) + (\vec{v}_\alpha \times \vec{\omega}_{B\alpha}) - \frac{T_\alpha}{m_\alpha n_\alpha} \nabla n_\alpha, \tag{3}$$

$$\frac{\partial n_\alpha}{\partial t} = -\nabla(n_\alpha \vec{v}_\alpha), \tag{4}$$

$$\nabla \times \vec{B} = \frac{4\pi}{c}\vec{j} + \frac{1}{c}\frac{\partial \vec{E}}{\partial t}, \tag{5}$$

$$\nabla \times \vec{E} = -\frac{1}{c}\frac{\partial \vec{B}}{\partial t}, \tag{6}$$

$$\nabla \cdot \vec{E} = 4\pi\rho, \tag{7}$$

where

$$\vec{j} = e(n_i \vec{v}_i - n_e \vec{v}_e),$$
$$\rho = e(n_i - n_e),$$
$$\vec{F}_\alpha = \frac{e_\alpha}{c}(\vec{v}_\alpha \times \vec{B}) - m_\alpha (\vec{v}_\alpha \nabla)\vec{v}_\alpha.$$

Index $\alpha = i, e$ corresponds to the ion and electron components of plasma, respectively. As $F_{pi} = \frac{m_e}{m_i} F_{pe}$, influence of F_{pi} force is small, and can be neglected. In Ampere-Maxwell's equation we also neglect the displacement current.

We consider equations in Cartezian coordinates (x, y, z), supposing that all of the wave vectors are situated in OXZ plane. It is assumed that the wave synchronism conditions are satisfied:

$$\omega_0 = \omega + \omega_1, \quad \vec{k}_0 = \vec{k} + \vec{k}_1, \tag{8}$$

where $\omega_1, \vec{k}_1, \omega, \vec{k}$ – frequency and wave vector of magnetosonic and ion-acoustic wave, respectively.

DISPERSION EQUATION FOR LOW-FREQUENCY PERTURBATIONS

Since Alfvén and ion-acoustic waves are the ultralow-frequency waves, we can use the plasma approximation for obtaining the dispersion equation:

$$\tilde{n}_e = \tilde{n}_i, \tag{9}$$

where $\tilde{n}_e$ and $\tilde{n}_i$ are perturbations of the ion and electron number densities. From the motion and continuity equations, we can write for $\tilde{n}_e$ and $\tilde{n}_i$:

$$\frac{\tilde{n}_e}{n_0} = \frac{e}{T_e}\left(\psi - \frac{k_x^2}{k_z^2}\frac{\omega^2}{\omega_{Be}^2}\phi - Q_{NL}\right), \tag{10}$$

$$\frac{\tilde{n}_i}{n_0} = \frac{e}{m_e}\left(\frac{k_z^2 \psi}{\omega^2} - \frac{k_x^2 \varphi}{\omega_{Bi}^2}\right). \tag{11}$$

Here

$$Q_{NL} = \frac{k_x \omega}{e k_z^2 \omega_{Be}}\left(i\frac{\omega}{\omega_{Be}}F_x + F_y\right) + \frac{F_z}{iek_z}.$$

To find the relation between φ and ψ, we use z component of Ampere's law in two potential approximation and equation of charge conservation. Comparing (10) with (11) and using relation between φ and ψ, we obtain the dispersion equation for ultralow-frequency perturbations:

$$\left[\frac{k_z^2 V_s^2}{\omega^2}\left(1 - \frac{\omega^2}{k_z^2 V_A^2}\right)\left(1 - \frac{\omega^2}{k_z^2 V_s^2}\right) - \mu_s\right]\varphi = -Q_{NL}. \tag{12}$$

In the absence of pump wave ($Q_{NL} = 0$) we have:

$$\begin{aligned} \omega_A^2 &= k_z^2 V_A^2 (1 + \mu_s), \\ \omega_s^2 &= k_z^2 V_s^2 / (1 + \mu_s). \end{aligned} \tag{13}$$

These expressions describe dispersion laws for the Alfvén and ion-acoustic waves, respectively. The special properties of these waves are their ability to propagate in xz plane, thus the wave energy can be transferred across the external magnetic field as well as along it. And since $\omega_s^2 \ll \omega_A^2$ and $\omega_A^2 \simeq k_z^2 V_A^2$, the dispersion equation for an ion-acoustic wave can be rewritten as:

$$\varepsilon \phi = \eta \psi_0 E_{1y}^*, \tag{14}$$

where

$$\varepsilon = \omega^2 - k_z^2 V_s^2 / (1 + \mu_s),$$

$$\eta = -\frac{\omega^2}{\omega_{Be}} \frac{k_{0x}}{k_z} \frac{V_{Te}^2}{V_A} \frac{e}{T_e},$$

In the calculation of the coupling coefficient η, we have taken into account the pondermotive force created by interaction of the pump wave with the magnetosonic wave.

DISPERSION EQUATION FOR MAGNETOSONIC WAVE

To obtain a dispersion equation for magnetosonic wave propagating across magnetic field, we also use plasma approximation. In this case ions and electrons velocity must coincide. From the electron equation of motion we find:

$$V_{ex} = \frac{e}{m_e \omega_{Be}} \left(E_{1y} + i \frac{\omega_1}{\omega_{Be}} E_{1x} \right) + \frac{1}{m_e \omega_{Be}} \left(i \frac{\omega_1}{\omega_{Be}} F_{1x} + F_{1y} \right), \tag{15}$$

where the term proportional to (ω / ω_{Be}) describes the inertial drift, of the wave that propagates across magnetic field. The component of pondermotive force is determined by interaction of pump wave and ion-acoustic wave. From the ion equation of motion and Maxwellś equation we write expression for V_{ix}:

$$V_{ix} = \frac{k_1^2 V_A^2}{\omega_1^2} \frac{e E_{1y}}{m_e \omega_{Be}}. \tag{16}$$

Comparing (15) with (16) we obtain dispersion equation for the magnetosonic wave:

$$\varepsilon_1 E_{1y} = \eta_1 \varphi^* \phi_0, \tag{17}$$

where

$$\varepsilon_1 = \omega_1^2 V_A^2$$

and coupling coefficient is determined by

$$\eta_1 = -2 V_A V_S \frac{m_e}{e} \left(\frac{V_{Te}}{V_A} \right)^2 \frac{k_{0x}}{\omega_{Be}} \omega_1^2 \omega_0 \mu_e \tag{18}$$

$$\mu_e = k_x^2 \rho_e^2.$$

NONLINEAR DISPERSION EQUATION AND DECAY GROWTH RATE

From ion-acoustic (14) and magnetosonic (17) dispersion equations we can obtain a nonlinear dispersion relation describing three-wave interaction:

$$\varepsilon \varepsilon_1^* = \eta \eta_1^* \mid \phi_0 \mid^2 . \tag{19}$$

In the absence of the pump wave, $\phi_0 = 0$, two kinds of waves with frequencies $\omega = \omega_k$ and $\omega_1 = \omega_{1k}$ exist in the plasma. In the presence of the pump wave, $\phi_0 \neq 0$, energy transfer from the pump KAW to the other plasma modes occurs, and amplitudes increase with the growth rate. Putting $\omega = \omega_r + i\gamma$, $\omega_1 = \omega_{1r} + i\gamma$ ($\mid \gamma \mid \ll \omega_r, \omega_{1r}$) into (19) and expanding ε and ε_1 in Taylor series, we obtain an expression for the wave growth rate:

$$\gamma^2 = \left. \frac{\eta \eta_1^* |\phi_0|^2}{\frac{\partial \varepsilon}{\partial \omega} \frac{\partial \varepsilon_1}{\partial \omega_1}} \right|_{\omega = \omega_r, \omega_1 = \omega_{1r}}, \tag{20}$$

where ω_r and ω_{1r} are defined from equations:

$$\varepsilon(\omega_r, \vec{k}) = 0, \qquad \varepsilon_1(\omega_1, \vec{k_1}) = 0.$$

Substituting the expressions for the coupling coefficients η, η_1 and derivative $\dfrac{\partial\varepsilon}{\partial\omega}$, $\dfrac{\partial\varepsilon_1}{\partial\omega_1}$ we find:

$$\gamma^2 = \frac{W}{2}\frac{V_S}{V_A}\frac{\omega_0^2}{\omega_{Be}k_z V_A}\left(\frac{\omega}{\omega_{Be}}\right)\mu_e\omega_{pe}^2, \tag{21}$$

where

$$W = \frac{\left|E_{0x}^2\right|}{4\pi n_0 T_e}. \tag{22}$$

CONCLUSIONS

Let us estimate the instability growth rate for the coronal plasma. Spectroscopic observations suggest the presence of the Alfvén waves with amplitudes $B/B_0 = 0.01$ in coronal loops (Hara, 1999). To examine existence of the Alfvén waves, these authors used the method first proposed by McClements *et al.* (1991). Typical parameters for such loop are the length $L = (2-5)\times 10^9$ cm, $n = (0.5-1)\times 10^{10}$ cm^{-3}, $B = 100-500$ G, $T = 4\times 10^6$ K, $\omega_{pe}/\omega_{Be} \approx 10$, $\mu_e \approx 1$, $\omega_1 \approx 10^{-1}\omega_{Bi}$. Substituting these values of the plasma parameters and the KAW intensity of $W \approx 10^{-5} - 10^{-6}$ into (21), we obtained $\gamma \approx \left(10^2 \div 10^3\right) c^{-1}$ and the time of instability development $\tau = \gamma^{-1} \approx 0.01$ c, respectively.

The nonlinear interaction of the Alfvén waves with the magnetosonic and ion-acoustic waves presented in this paper could occur in the Earth magnetosphere as well as in the solar magnetosphere, where a value of the plasma parameter β is low. In the solar atmosphere the sources of the Alfvén waves can be 5-min. chromospheric oscillation that swing the basis of magnetic loops and lead to propagation of the Alfvén waves into corona. Alfvén waves will transform into the kinetic Alfvén waves during the propagation along magnetic field. The kinetic Alfvén wave can interact more effectively with other kinds of waves because of the presence of a non-zero longitudinal component of the electric field E_z. When KAW reaches the region with low plasma parameter β it will decay into the magnetosonic and ion-acoustic waves. Due to their rapid dissipation, these waves are more effective for heating of the coronal plasma. The excitation of fast magnetosonic waves by phase mixing of an Alfvén wave was considered in Nakarjakov (1997). The relative effective excitation of the slow and fast magnetosonic waves by Alfvén waves needs further investigation.

REFERENCES

[1] *Belcher J.W., Devis L.* Large-amplitude Alfvén waves in the interplanetary medium // J. Geophys. Res.–1971.–**76**, N 1.–P. 3539–3574.

[2] *Goossens M.* Alfvén wave heating // Space Sci. Rev.–1994.–**68**.–P. 51.

[3] *Hara H. and Ichimoto K.* Microscopic Nonthermal Plasma Motions of Coronal Loops in a Solar Active Region // Astrophys. J.–1999.–**513**.–P. 969–982.

[4] *McClements, et al.* The detection of wave activity in the solar corona using UV line spectra // Solar Phys.–1991.–**131**.–P. 41.

[5] *Nakariakov V. M., Roberts B., Murawski K.* Alfvén Wave Phase Mixing as a Source of Fast Magnetosonic Waves // Solar Phys.–1997.–**175**.–P. 93–105.

[6] *Nishida A.* Geomagnetic diagnostics of the magnetosphere.–Moscow: Mir, 1980.–299 p. (in Russian).

[7] *Uchida Y., Kaburaki O.* Excess Heating of Corona and Chromosphere Above Magnetic Regions by Non-Linear Alfvén Waves // Solar Phys.–1974.–**35**.–P. 451.

[8] *Volokitin A. S., Dubinin E. M.* The turbulence of Alfvén waves in the polar magnetosphere of the earth // Planet. and Space Sci.–1989.–**37**.–P. 761–765.

[9] *Wentzel D. G.* Coronal heating by Alfvén waves // Solar Phys.–1974.–**35**.–P. 451.

NEAR SPACE PLASMA DIAGNOSTIC AT EXTREMELY LOW FREQUENCIES

J.-L. Bougeret[1], N. N. Kalinichenko[2], A. A. Konovalenko[2], I. S. Falkovich[2], M. R. Olyak[2]

[1] *Paris-Meudon Observatory, France*

[2] *Institute of Radio Astronomy, NAS of Ukraine*
4 Chervonopraporna St., 61002 Kharkiv-2, Ukraine
e-mail: kalinich@ira.kharkov.ua

Solar wind shock waves associated with high-speed streams and coronal mass ejections (CMEs) are constantly present in the interplanetary medium. Though they decay with distance from the Sun, the most powerful CMEs are observed close to the border of the heliosphere [1]. Shocks in the inner heliosphere have been extensively studied by measuring the interplanetary scintillation (IPS) of distant, compact radio sources at centimetre, decimetre and metre wavelengths at which the scintillation index has maximum at solar elongations less 90° [2]. Since at large elongations the scintillation index at decametre wavelengths is higher than that above-stated, it is interesting to investigate whether IPS technique at decametre wavelengths can be applied with greater success to study large-scale solar wind disturbances in the outer heliosphere. It is necessary to note that such research have been only episodically undertaken with the help of spacecrafts.

To study this question, IPS observations have been made with the UTR-2 radio telescope of the Institute of Radio Astronomy of the NASU [3]. The UTR-2 radio telescope is the world's largest decametric array that operates at the frequency range from 8 MHz to 32 MHz. The full effective area of the UTR-2 is near 150,000 square meters for the zenith orientation and the beam width range is from 20 minutes to 1.5 degrees of arc. The radio source 3C273 was observed at solar elongation $\cong 140°$. To discriminate a radio source signal and a terrestrial interference, the standard procedure of simultaneous observations of a radio source and a background one was applied by using 5 spatially separated beams of the UTR-2 antenna array. Two frequencies were used: 20 and 25 MHz, with band width 10 kHz. The data processing consists in definition of scintillation indices with the purpose of detection of their sharp (hours), long (few days), and strong (tens of percents) increases which can be associated with shocks.

Since December 1999 to March 2000 we completed a total of 56 hours of IPS observations and did not find out such disturbances except for the case on January 26, 2000. During these observations the scintillation index was typically as 0.09 ± 0.02 (20 MHz) and 0.1 ± 0.02 (25 MHz). On January 26, 2000 down to 23:40 UT the scintillation index behaved in a similar manner. From 23:40 UT at the interval of about 1.5 hours the appreciable increase of the scintillation index from 0.09 to 0.18 to be occurred. In our opinion, however, the shocks are not the cause of this phenomenon. The detailed analysis of the visible movement of the radio source on this day shows that it crossed the "shadow" of the Moon in the solar wind and the beginning and end of the effect rather well coincided with the radio source going in and out the lunar "shadow".

It is known that the Moon as well as another bodies of the solar system are the obstacle on the way of the solar wind. Its movement results in the perturbation of the interplanetary magnetic field and plasma. Calculations have shown that on the night side of the Moon the cavity (or "shadow") of the conic form which lasts behind it in the direction of the solar wind will be formed [4]–[6]. The magnetic field strength increases and the interplanetary plasma density decreases inside the cavity. The phenomenon which we name by the lunar cavity or "shadow" was first discovered by Explorer 18 [7].

The assumption of the connection of the index increase with the lunar "shadow" is not contradicted by the scintillation spectra. Inside the "shadow" the spectra are wider than outside of it. Physically, it can mean an increase of irregularities of a speed or/and a share of small-scale irregularities over the line of sight. During the other days of observations the lack of the effect may well be attributable to large distance between the Moon and the examined region at which the "shadow" is weak (for the moment, this distance was equal to $14\,R_L$, during the other days of observations $\geq 30\,R_L$).

Our results can be summarized as follows:

1. No shock was found in the data of our observations. We believe that it may be connected with the short duration of observations and with only one direction of observations.

2. The increase of the scintillation index, which we observed on 26.01.2000, is probably associated with

the lunar "shadow" in the solar wind. If this statement is correct, then the size of irregularities is less inside the lunar "shadow" and speed of irregularities is higher than outside of it.

3. IPS technique at decametre wavelengths, which is efficient for large elongations, especially with using of a huge radio telescope, can be useful as a ground support of space missions (WIND, STEREO, *etc.*) to study parameters and evolution of large-scale solar wind structures moving from the Sun up to the Earth and further behind its orbit combining with low frequency observations of various kind solar radioemissions.

Acknowledgements. This work was supported in part by grant INTAS-CNES 97-1450.

REFERENCES

[1] *Gurnett D. A., Kurth W. S., Allendorf S. C., Poynter R. L.* Radio emission from the heliopause triggered by an interplanetary shock // Science.–1993.–**262**.–P. 199–203.

[2] *Behannon K. W., Burlaga L. F.* Structure and evolution of compound streams at AU // J. Geophys. Res.–1991.–**96**.–P. 21,213–21,225.

[3] *Braude S. Ya., Megn A. V., Sodin L. G.* Decametre waves radiotelescope UTR-2 // Antenny.–1978.–N 26.–P. 3–15.

[4] *Schwartz K., Schubert G.* Lunar electromagnetic scattering. 1. Propagation parallel to the diamagnetic cavity axis // J. Geophys. Res.–1973.–**78**.–P. 6496–6506.

[5] *Horning B., Schubert G.* Lunar electromagnetic scattering. 3. Propagation at arbitrary angles to the cavity axis // J. Geophys. Res.–1975.–**80**.–P. 4215–4229.

[6] *Podgorny I. M., Andriyanov Yu. V., Kulikov G. B.* Laboratory modeling of solar wind interaction with the Moon // Kosmicheskie issledovaniya.–1975.–**13**, N 6.–P. 914–922.

[7] *Ness N. F.* The probable observation of the Moon turbulence shadow // Proc. Solar Wind Conf., Pasadena, USA, 1964.

PARAMETRIC INTERACTION OF WHISTLER WAVES AND KINETIC ALFVÉN WAVES IN THE SPACE PLASMAS

A. K. Yukhimuk[1], **V. M. Fedun**[2], **E. K. Sirenko**[1], **Yu. M. Voitenko**[1], **and V. A. Yukhimuk**[3]

[1]*Main Astronomical Observatory, NAS of Ukraine*
27 Zabolotnoho St., 03680 Kyiv, Ukraine
e-mail: yukhimuk@mao.kiev.ua

[2]*Department of Astronomy and Space Plasma Physics, Taras Shevchenko National University*
6 Glushkova, 03022 Kyiv, Ukraine
e-mail: fedun@astrophys.ups.kiev.ua/fedun@mao.kiev.ua

[3]*Los Alamos National Lab., USA*

Satellite observations show a close relationship between the whistlers and lower-hybrid waves in space plasmas. Intense whistler waves generated by lighting discharges [17] or by quasi-monochromatic VLF transmitters can be unstable to three-wave parametric interaction. Work [7] demonstrates experimental results about excited lower hybrid waves by VLF whistler mode waves in the topside ionosphere and near magnetosphere. Kinetic Alfvén waves are often observed by satellites [21, 32]. In this paper we consider analytically a possible mechanism of this relationship – parametric interaction of whistler pump waves with lower-hybrid and Alfvén waves in magnetized plasma with small plasma parameter. In the dynamics of Alfvén waves the kinetic effects (finite ion Larmor radius and electron inertia) are taken into account. A nonlinear dispersion equation describing three-wave interaction is obtained in the framework of two-fluid magnetohydrodynamics. The instability growth rates and time of instability development are found. Our theoretical investigation shows that the whistler mode well be an effective source of the lower hybrid and Alfvén waves in the magnetospheric plasma. This nonlinear process can take place in the Earth magnetosphere and in the solar atmosphere. The products of the decay – lower-hybrid and kinetic Alfvén waves – can effectively interact with magnetospheric and solar plasmas.

INTRODUCTION

The interest to the three-wave resonant (TWR) parametric decay closely related with the study of the origin of the waves observed in the laboratory and space plasmas. Also, different wave modes damp with different rates, and a mutual transformation of the wave modes caused by TWR can significantly change the rate of plasma heating, often providing an explanation for enhanced (or reduced) plasma heating. Therefore, the parametric interactions is of great interest [3, 25, 22, 27, 12, 20, 34, 35]. In introduction we shall be interested in processes, which can be united by the same physical phenomenon, the parametric interaction of whistler mode waves with ionospheric and magnetospheric plasmas [23] analyzing the effect of parametric excitation of the electrostatic whistler waves by electron plasma waves. A new excitation mechanism of auroral Langmuir and Alfvén waves in the planetary magnetosphere is presented in [10]. It was shown that a large-amplitude electromagnetic whistler wave propagating along the magnetic field lines can nonlinearly generate Langmuir and Alfvén waves through three wave parametric instability. The question of a generation of the oblique Alfvén waves by the parametric instability of the whistlers in the near Earth Plasma is considered in [28], namely the decay process with participation two whistlers waves spreading under angles to an external magnetic field and oblique Alfvén wave. It is shown that parametric instability whistlers should reduce to fast growth oblique Alfvén waves with perpendicular wave length. There is also very interesting work [13]. In this paper the parametric instability of quasi-monochromatic VLF waves in the upper ionosphere is considered. It is shown that the initial signal scattering into a low-frequency plasma wave and decaying into low frequency and ion-cyclotron waves is the most effective. A parametric interaction between two whistlers and ion-cyclotron wave is considered. The above process also may be responsible for excitation of the low-hybrid resonance in the ionosphere and magnetosphere of the Earth. The processes of whistlers scattering in the fields of big angles to an external magnetic field were analyzed in the paper [29]. In the paper [25] the decay of UHW on the whistler and KAW was studied. In the paper [22] the decay of LHW on the UHW and electromagnetic wave was studied. Later [20] used theoretical results of Murtaza and Shukla for interpretation of the nature of downshifted maximum, and of Stenflo for interpretation of stimulated electromagnetic emission in the ionosphere. In the paper [35] the nonlinear interaction of kinetic Alfvén wave with upper hybrid wave has been investigated, and the results were used for the interpretation of long-period geomagnetic pulsations.

Whistlers are one of the most widespread type of waves in a magnetized plasma. The generation mechanisms are related to flashes, particle beams, anisotropic velocity distributions of particles, and nonlinear processes in space plasmas. In the Earth magnetosphere, whistlers can propagate from one hemisphere to another, and under favorable conditions can be detected by the ground instruments and satellites in "magnetoconjugated" points. The low-hybrid waves were often observed simultaneously with whistlers [4, 8, 11, 26, 6, 7]. Satellite observations shown a close relationship between whistlers and LHWs [30, 5], and suggested that whistlers are the source of the lower hybrid wave.

However, despite of the observational data mentioned above, an exact mechanism of such a close relation between lower hybrid emissions and whistlers is still uncertain. In the present paper the nonlinear interaction of whistlers and lower hybrid waves have been investigated. Lower hybrid wave is excited as a result of parametric decay of whistlers into KAWs and LHW. A high efficiency of the interaction among KAWs and whistlers is caused by the presence of the longitudinal component of KAW electric field.

BASIC EQUATIONS

Parametric instability, where the whistlers wave decay to the LHW and kinetic Alfvén wave W = LHW + KAW is considered.

Whistler pump wave

$$\vec{E}_0 = (E_{0x}\vec{e}_x + E_{0y}\vec{e}_y)\exp i\psi_0 + c.c., \tag{1}$$

where $\psi_0 = -\omega_0 t + k_{0x}x + k_{0z}z$, $\omega_0 = \left(k_0^2c^2/\omega_{pe}^2\right) \mid cos\theta\omega_{Be} \mid$, propagates in the homogeneous magnetized plasma ($\overrightarrow{B_0} = B_0\overrightarrow{e_z}$). It is assumed that the wave synchronism condition is satisfied

$$\omega_0 = \omega + \omega_1, \quad \vec{k}_0 = \vec{k} + \vec{k}_1, \tag{2}$$

where $\omega_0, \vec{k}_0$ – the frequency and wave vector of whistler pump wave, $\omega, \vec{k}$ – the frequency and wave vector of kinetic Alfvén wave, $\omega_1, \vec{k}_1$ – the frequency and wave vector of lower hybrid wave. Let us consider that all wave vectors are situated in OXZ plane.

To study three-waves parametric interaction we use two-fluid magnetohydrodynamics (MHD):

$$\frac{\partial \vec{v}_\alpha}{\partial t} = \frac{1}{m_\alpha}(e_\alpha\vec{E} + \vec{F}_\alpha) + (\vec{v}_\alpha \times \vec{\omega}_{B\alpha}) - \frac{T_\alpha}{m_\alpha n_\alpha}\nabla n_\alpha, \tag{3}$$

$$\frac{\partial n_\alpha}{\partial t} = -\nabla(n_\alpha\vec{v}_\alpha), \tag{4}$$

$$\nabla \times \vec{B} = \frac{4\pi}{c}\vec{j} + \frac{1}{c}\frac{\partial \vec{E}}{\partial t}, \tag{5}$$

$$\nabla \times \vec{E} = -\frac{1}{c}\frac{\partial \vec{B}}{\partial t}, \tag{6}$$

$$\nabla \cdot \vec{E} = 4\pi\rho, \tag{7}$$

where

$$\vec{j} = e(n_i\vec{v}_i - n_e\vec{v}_e),$$
$$\rho = e(n_i - n_e),$$
$$\vec{F}_\alpha = \frac{e_\alpha}{c}(\vec{v}_\alpha \times \vec{B}) - m_\alpha(\vec{v}_\alpha\nabla)\vec{v}_\alpha.$$

Index $\alpha = i, e$ corresponds to the ion and electron components of plasma, respectively. Electron density and velocity, electric and magnetic field are presented in the form:

$$\begin{aligned} n_e &= n_0 + \tilde{n}_A + \tilde{n}_1, \\ \vec{v}_e &= \vec{v}_0 + \vec{v}_A + \vec{v}_1, \\ \vec{E} &= \vec{E}_0 + \vec{E}_A + \vec{E}_1, \\ \vec{B} &= B_0\vec{e}_z + \vec{B}_A, \end{aligned} \tag{8}$$

where n_0 is the mean value of plasma density, index 0 in expression for $\vec{v}_e$ and $\vec{E}$ denotes the variable related to the pump wave, and indexes A and 1 denote the variables related to KAW and UHW, respectively.

DISPERSION EQUATION OF ALFVÉN WAVES

To obtain dispersion equation we use plasma approximation

$$\tilde{n}_e = \tilde{n}_i, \tag{9}$$

as Alfvén waves are slow. Here $\tilde{n}_e$ and $\tilde{n}_i$ are the perturbations of electron and ion density, respectively. From the motion Equation (3) and continuity Equation (4) we find the expression for $\tilde{n}_e$, $\tilde{n}_i$:

$$\frac{\tilde{n}_e}{n_0} = \left(1 - \frac{v_{ph}^2}{v_{T_e}^2}\right)^{-1} \frac{e}{T_e}\left[\varphi - A + \frac{k_x}{k_z^2}\frac{\omega}{\omega_{Be}}\frac{1}{e}\left(i\frac{\omega}{\omega_{Be}}F_x + F_y\right) + \frac{F_z}{iek_z}\right], \tag{10}$$

$$\frac{\tilde{n}_i}{n_0} = -\frac{e}{T_e}\frac{\mu_i}{1+\mu_i}\left(\varphi + \frac{\omega_{Bi}^2 k_z^2}{\omega^2 k_x^2}A\right), \tag{11}$$

where $v_{ph} = \omega/k_z$, $A = \frac{\omega}{k_z c}A_z$, $\mu = k_x^2\rho_i^2$, $\rho_i = v_{Ti}/\omega_{Bi}$ is the ion Larmor radius, φ and A_z are scalar and vector potentials of KAW electric field, respectively. The first relation between φ and A follows from (10)–(11):

$$\begin{aligned} A \;=\; & \left(1 + \frac{T_e}{T_i}\frac{\mu_i}{1+\mu_i}\left(1 - \frac{V_{ph}^2}{V_{Te}^2}\right)\right)\varphi - \frac{k_x^2}{k_z^2}\frac{\omega^2}{\omega_{Be}^2}\frac{1}{iek_x}\bar{F} + \\ & \frac{1}{iek_z}F_z - \frac{T_e}{e}\frac{V_{ph}^2}{V_{Te}^2}\frac{\vec{k}}{\omega}\cdot\left(\frac{n}{n_0}\vec{V}\right)_e, \end{aligned} \tag{12}$$

where

$$\bar{F} = \left(F_x - i\frac{\omega_{Be}}{\omega}F_y\right).$$

We can find the second relation between φ and A from the perpendicular projection of Ampere low:

$$-k^2 k_z A_z = \frac{4\pi}{c}k_x j_x. \tag{13}$$

The linear part of the transverse current j_x is determined by the plasma ion component, but the nonlinear perpendicular current is generated by the beating of LHW and whistler in electron motions:

$$j_x = en_0 V_{ix}^L + j_{ex}^{NL}. \tag{14}$$

Inserting the expression for ion velocity and nonlinear electron current we get the second relation between KAW potentials:

$$\begin{aligned} A \;=\; & \frac{V_{ph}^2}{V_A^2}\frac{1}{1+\mu_i}\varphi + \left(k_z^2\delta_i^2\right)^{-1}\frac{m_i}{e}\frac{\omega}{k_x}\frac{n_e^L}{n_0}V_{ex}^L + \left(k_z^2\delta_i^2\right)^{-1}\frac{m_i}{e}\frac{\omega^2}{\omega_{Be}^2}\times \\ & \left[\left(\frac{V_{ph}^2}{V_{Te}^2} - 1\right)^{-1}\frac{1}{im_e k_z}F_z + \left(\frac{V_{ph}^2}{V_{Te}^2} - 1\right)^{-1}\frac{\omega}{k_z^2}\vec{k}\cdot\left(\frac{n}{n_0}\vec{V}\right) + \frac{1}{im_e k_x}\bar{F}\right], \end{aligned} \tag{15}$$

where $\delta_i^2 = c^2/\omega_{pi}^2$. Equating (12)–(15) we obtain the nonlinear dispersion equation for KAW:

$$\begin{aligned} & \left[\frac{V_{ph}^2}{V_A^2}(1+\chi_e) - (1+\bar{\mu}_i)\right]\frac{1}{1+\mu_i}\varphi = \\ & \frac{1}{iek_z}F_{ez} - \frac{m_e}{m_i}\frac{V_{ph}^2}{V_A^2}(1+\chi_e)\frac{1}{iek_x}\left(F_{ex} - i\frac{\omega_{Be}}{\omega}F_{ey}\right) - \\ & \frac{m_i}{e}\left(k_z^2\delta_i^2\right)^{-1}\frac{\omega}{k_x}(1+\chi_e)\frac{n_e^L}{n_0}V_{ex}^L, \end{aligned} \tag{16}$$

where $\chi_e = k_x^2\delta_e^2, \bar{\mu}_i = (1+T_e/T_i)\mu_i$. From the motion equation we find electron velocity components in the field of whistler wave:

$$v_{0x} = -i\frac{eE_{ox}}{m_e(\omega_0-\omega_{Be})}, \qquad (17)$$
$$v_{0x} = \frac{eE_{ox}}{m_e(\omega_0-\omega_{Be})},$$

and from (6) we find components of magnetic field pump wave:

$$b_{0x} = -i\frac{ck_{oz}}{\omega_0}E_{0x},$$
$$b_{0y} = \frac{ck_{oz}}{\omega_0}E_{0x}, \qquad (18)$$
$$b_{0z} = i\frac{ck_{ox}}{\omega_0}E_{0x}.$$

Velocity components in the LHW field can be obtained from electron motion equation:

$$v_{1x} = -\frac{ek_{1x}\omega_1}{m_e(\omega_1^2-\omega_{Be}^2)}\varphi_1,$$
$$v_{1y} = -i\frac{ek_{1x}\omega_{Be}}{m_e(\omega_1^2-\omega_{Be}^2)}\varphi_1, \qquad (19)$$
$$v_{1z} = -\frac{ek_{1z}}{m_e\omega_1}\varphi_1.$$

Using expressions (17)–(19) and from (16), we find dispersion equation for the Alfvén wave:

$$\varepsilon_A\varphi = \mu_A(E_{0x}\varphi_1^*), \qquad (20)$$

where μ_A is the coupling coefficient defined by the expression:

$$\mu_A = i\frac{e}{m_e}\frac{k_{1x}}{\omega_{Be}}\frac{k_{0z}}{k_z}\frac{k_z^2V_A^2}{\omega_0}(1+\mu_i)\left[1+\frac{m_e}{m_i}\frac{k_z}{k_x}\frac{\omega_{Be}^2}{\omega_1\omega}\frac{k_{1z}}{k_{1x}}(1+\bar{\mu_i})\right],$$
$$\varepsilon_A = \omega^2 - k_z^2V_A^2(1+\bar{\mu_i}).$$

In the calculation of the coupling coefficient μ_A, we have taken into account the pondermotive force created by scattering whistlers pump wave on LHW. And since we consider magnetosphere, where the plasma parameter is as $m_e/m_i << \beta << 1$, and we keep therms with finite-Larmor-radius effects in the dispersion equation for KAW.

DISPERSION EQUATION OF LHW

Dispersion equation of LHW can be find from Puasson equation:

$$\triangle\varphi_1 = -4\pi e(\tilde{n}_i - \tilde{n}_e). \qquad (21)$$

We find expression for $\tilde{n}_i$, $\tilde{n}_e$ from the motion Equation (3) and continuity Equation (4):

$$\tilde{n}_i = \frac{en_0}{m_i}\left(\frac{k_{1x}^2}{\omega_1^2-\omega_{Bi}^2}+\frac{k_{1z}^2}{\omega_1^2}\right)\varphi_1, \qquad (22)$$

$$\widetilde{n_e} = -\frac{en_0}{m_e}\left(\frac{k_{1x}^2}{\omega_1^2-\omega_{Bi}^2}+\frac{k_{1z}^2}{\omega_1^2}\right)\varphi_1 - \frac{n_0}{m_e}\frac{k_{1x}\omega_{Be}}{\omega_1(\omega_1^2-\omega_{Be}^2)}\times \qquad (23)$$
$$\left[i\frac{\omega_1}{\omega_{Be}}F_{1x}+F_{1y}+i\frac{k_{1z}}{k_{1x}}\frac{(\omega_1^2-\omega_{Be}^2)}{\omega_1\omega_{Be}}F_{1z}\right] - \frac{\vec{\nabla}\langle\tilde{n_A}\vec{V_0}\rangle}{-i\omega},$$

where components of pondermotive force are defined by interaction of pump wave and Alfvén wave. From (21)–(23) we find the dispersion equation for LHW:

$$\varepsilon_1 \varphi_1 = \mu_1 \left(E_{0x} \varphi^* \right), \tag{24}$$

where coupling coefficient μ_1 is defined by the expression:

$$\mu_1 = i \frac{e}{m_e} \frac{\mu_s}{1+\mu_i} \frac{\omega}{k_z} \frac{1}{V_{Te}^2} \frac{k_{0z}}{\omega_0} \frac{\omega_1 \omega_{Be}}{k_{1x}} \left[1 + \frac{k_{1z}}{k_{1x}} \frac{k_z}{k_{0z}} \frac{k_z}{k_x} \frac{\omega_0}{\omega_1} \frac{\omega_{Bi}^2}{\omega^2} \frac{V_{Te}^2}{V_s^2} \left(1 + \tilde{\mu_i}\right) + \frac{\omega_0}{\omega} \frac{k_z}{k_{0z}} \right],$$

$$\varepsilon_1 = \omega_1^2 - \frac{\omega_{pi}^2}{1 + \frac{\omega_{pe}^2}{\omega_{Be}^2}} \left(1 + \frac{m_i}{m_e} \frac{k_{1z}^2}{k_1^2} \right).$$

NONLINEAR DISPERSION EQUATION FOR THREE-WAVE INTERACTION

From Equations (20) and (24) we find the nonlinear dispersion equation describing three-wave interaction (decay of whistler pump wave into the KAW and LHW):

$$\varepsilon_A \varepsilon_1^* = \mu_A \mu_1^* |\varphi_0|^2. \tag{25}$$

Assuming in (25)

$$\omega = \omega_r + i\gamma_1,$$

$$\omega_1 = \omega_{1r} + i\gamma_1,$$

(where $|\gamma| \ll \omega_r, \omega_{1r}$) and decomposing ε_A and ε_1 to the Taylor series after the small parameter $i\gamma_1$ we obtain the expression for the instability growth rate

$$\gamma_1 = \left. \frac{\mu_A \mu_1^* |E_{0x}|^2}{\frac{\partial \varepsilon_A}{\partial \omega} \frac{\partial \varepsilon_1}{\partial \omega_1}} \right|_{\omega = \omega_r, \omega_1 = \omega_{1r}}, \tag{26}$$

where ω_r and ω_{1r} could be found from the equations

$$\varepsilon_A(\omega_r, \vec{k}) = 0, \qquad \varepsilon_1(\omega_1, \vec{k_1}) = 0.$$

Substituting values of derivatives

$$\frac{\partial \varepsilon_A}{\partial \omega} = 2\omega, \qquad \frac{\partial \varepsilon_1}{\partial \omega_1} = 2\omega_1,$$

and coefficients μ_A and μ_1 into (26) we obtain

$$\gamma_1^2 = \frac{W}{4} \frac{\omega_{pe}^2}{\omega_0^2} \mu_s V_A^2 k_{0z}^2 \times \left[1 + \frac{m_e}{m_i} \frac{k_z}{k_x} \frac{\omega_{Be}^2}{\omega_1 \omega} \frac{k_{1z}}{k_{1x}} \left(1 + \bar{\mu_i}\right) \right] \times \left[1 + \frac{k_{1z}}{k_{1x}} \frac{k_z}{k_{0z}} \frac{k_z}{k_x} \frac{\omega_0}{\omega_1} \frac{\omega_{Bi}^2}{\omega^2} \frac{V_{Te}^2}{V_s^2} \left(1 + \tilde{\mu_i}\right) + \frac{\omega_0}{\omega} \frac{k_z}{k_{0z}} \right], \tag{27}$$

where $W = \dfrac{|E_{0x}|^2}{4\pi n_0 T_e}$.

DISCUSSION AND APPLICATION

In this paper we consider analytically the nonlinear parametric interaction of whistlers with LHW and Alfvénic wave in a low-β plasma. The kinetic effects (finite ion Larmor radius and electron inertia) are taken into account for dispersion law, when we investigate the dynamics of Alfvén wave. Such Alfvén wave are usually called kinetic Alfvén wave. They have some properties which are different from the MHD Alfvénic wave. They include a presence of nonzero parallel electric field E_z and can propagate in xz-plain. Due to this properties KAW interact effectively with whistler and amplify lower hybrid wave. The nonlinear three-wave parametric interaction we consider can observe in laboratory and space plasma with low-β plasmas. Such processes in space plasmas can take place in the ionosphere and magnetosphere of the Earth, and in the some regions of solar atmosphere where the plasma parameter is small.

In our paper we consider magnetospheric plasma in the capacity of supplement (or application). Typical parameters for magnetospheric plasma at $3-4\ R_E$ are following: $V_{Te} \approx 10^7\,\mathrm{cm\,c^{-1}}$, $\omega_{pe} \approx 10^5\,\mathrm{c}^{-1}$, $\omega_{Be} \approx 10^5\,\mathrm{c}^{-1}$, $\omega_{Bi} \approx 10^2\,\mathrm{c}^{-1}$. Substituting plasma parameters and whistlers intensity $W \simeq 10^{-5}$ into (27), the time of instability development is of $\tau \approx \gamma_{\max}^{-1} = 0.01$ c.

Our theoretical investigation show, that whistler wave, propagating in the magnetosphere, will be a source of lower hybrid and Alfvén waves. Theoretical results can explain satellite observations of the coexistence of whistler, lower hybrid and Alfvén waves.

The nonlinear parametric processes considered in this paper could take place in the solar corona as well, where whistlers are generated by energetic electrons in magnetic traps on the Sun. Whistlers will excite lower hybrid and Alfvén waves while propagating through the solar atmosphere. Lower hybrid wave can effectively accelerate electrons to high energy. Kinetic Alfvén waves interact effectively with plasma particles and participate in the heating and acceleration of space plasma particles owing to presence of the longitudinal component of electric field. Thus, the products of the decay – low-hybrid and kinetic Alfvén waves – can affect the magnetospheric and solar plasmas stronger than the initially excited whistler waves.

Acknowledgements. This work was supported in part by INTAS Grant 99-00-78.

REFERENCES

[1] *Alongi M., Bertelli G., Bressan A. et al.* Results of Observations // Astrophys. J.–1993.–**97**, N 1.–P. 851–860.

[2] *Benz A. O., Smith D. F.* Stochastic acceleration of electrons in Solar flares // J. Geophys. Res.–1987.–**107**, N 2.–P. 299–309.

[3] *Berger R. L., Chen L.* Excitation of fast waves by slow waves near the lower-hybrid frequency // Phys. Fluids.–1976.–**19**.–P. 1392–1399.

[4] *Barrington R. E., Berlose G. S.* Preliminary results from the very-low-frequency receiver on board Canadas Alouette satellite // Nature.–1963.–**198**.–P. 651–656.

[5] *Bell T. F., Ngo H. D.* Electrostatic waves stimulated by coherent VLF signals propagating in and near the inner radiation belt // J. Geophys. Res.–1988.–**93**.–P. 2599.

[6] *Bell T. F., Inan U. S., Sonwalnar V. S., et al.* DE-1 observations of lower hybrid waves excited by VLF whistler mode waves // Geophys. Res. Lett.–1991.–**48**.–P. 393.

[7] *Bell T. F., Inan U. S., Lauben D., et al.* DE-1 and COSMOS 1809 observations of lower hybrid waves excited by VLF whistler mode waves // Geophys. Res. Lett.–1994.–**21**, N 8.–P. 653–656.

[8] *Brice N. M., Smith R. L.* Recording from satellite Alouette-2-A very low frequency plasma resonance // Nature.–1964.–**203**.–P. 926–927.

[9] *Chin Y. C., Wentzel D. G.* Nonlinear dissipation of Alfv́en Waves // Astrophys. and Space Sci.–1972.–**16**.–P. 465.

[10] *Chian A. C.-L., Lopes S. R., Alves M. V.* Nonlinear excitation of Langmuir and Alfv́en waves by auroral whistler waves in the planetary magnetosphere // Astron. and Astrophys.–1994.–**288**.–P. 981–984.

[11] *Gurnett D. A.* A satellite study of VLF hiss // J. Geophys. Res.–1966.–**71**, N 23.–P. 5599–5615.

[12] *Gucha S., Sarkar R.* Parametric decay of a whistler wave at the difference frequency of two electromagnetic waves in a plasma // J. Plasma Physics.–1991.–**47**, N 1.–P. 115–123.

[13] *Grach S. M.* Parametric Instability of VLF Waves in the Upper Ionosphere // Radiophysica.–1975.–**18**, N 11.–P. 1627–1637. (in Russian).

[14] *Hasegava A., Chen L.* Kinetic processes in plasma heating by resonant mode conversion of Alfven wave // Phys. Fluids.–1976.–**30**.–P. 1924.

[15] *Hui C. H., Seyler C. E.* Electron acceleration by Alfvén waves in the magnetosphere // J. Geophys. Res.–1992.–**97**, N 4.–P. 3953–3963.

[16] *Ionson I. A.* Resonant absorption of Alfvénic surface waves and heating of solar coronal loops // Astrophys. J.–1978.–**226**, N 2.–P. 650–673.

[17] *Kelley M. C., Ding J. G.* Intence Ionospheric and Magnetic Field Pulses Generated by Lighting // Geophys. Res. Lett.–1990.–**17**, N 12.–P. 2221–2224.

[18] *Kletzing C. A.* Electron acceleration by kinetic Alfven waves // J. Geophys. Res.–1994.–**99**, N 11.–P. 11095–11103.

[19] *Lakhina G. S., Buti B.* Stochastic acceleration by lower hybrid waves in the solar corona // Solar Phys.–1996.–**165**, N 2.–P. 329–336.

[20] *Leyser T. B.* Parametric interaction between hybrid and low hybrid waves in heating experiments // Geophys. Res. Lett.–1991.–**18**, N 3.–P. 408–411.

[21] *Louran P., Wahlund J. E., Chust T.* Observation of Kinetic Alfven waves by the FREJA Spacecraft // Geophys. Res. Lett.–1996.–**21**, N 17.–P. 1847–1850.

[22] *Murtaza G., Shukla P. K.* Nonlinear generation of electromagnetic waves // J. Plasma Phys.–1984.–**31**.–P. 423–436.

[23] *Sharma R. P., Tripathi Y. K., Hadi A., et al.* Parametric Excitation of Electrostatic Waves by Electron Plasma Waves // J. Geophys. Res.–1992.–**97**.–P. 4275–4281.

[24] *Shukla P. K., Stenflo L.* Nonlinear Alfven waves // Physica Scripta.–1995.–**60**.–P. 32–35.

[25] *Shukla P. K., Mamedow M. A.* Nonlinear decay of a propagating lower-hybrid wave in a plasma // J. Plasma Phys.–1978.–**19**, N 1.–P. 87–96.

[26] *Scarf F. L., Fredrics R. W., Smith E. J., et al.* OGO-5 observations of LHR noise emissions and whistlers near the plasmapause at several Earth radii during a large magnetic storm // J. Geophys. Res.–1972.–**77**, N 10.–P. 1776–1793.

[27] *Stenflo L.* Stimulated scattering of large amplitude waves in the ionosphere // Physica Scripta.–1990.–**30**.–P. 166–169.

[28] *Taranenko Yu. N., Chmyrev V. M.* Generation of Oblique Alfven Waves by the Parametric Instability of Whistlers in the Near-Earth Plasmas // Geomagnetizm and Aeronomy.–1987.–**27**.–P. 664–665.

[29] *Taranenko Yu. N., Chmyrev V. M.* Parametric Interaction of Whistler and Electron Cyclotron Waves in the ionospheric Plasma // Geomagnetizm and Aeronomy.–1989.–**29**.–P. 459–464.

[30] *Titova E. E., Di V. I., Yurov V. E., et al.* Interaction between VLF waves and turbulent ionosphere // Geophys. Res. Lett.–1984.–**11**.–P. 323.

[31] *Robert I., Stefant R. J.* Alfven wave damping from finite gyroradius coupling to the ion acoustic mode // Phys. Fluids.–1970.–**13**, N 2.–P. 440–450.

[32] *Volokitin A. S., Dubinin E. M.* The turbulence of Alfven waves in the polar magnetosphere of Earth // Planet. and Space Sci.–1989.–**37**, N 7.–P. 761–768.

[33] *Yukhimuk A. K.* Plasma phenomenons in geophysics.–Kiev: Naukova Dumka, 1982.–165 p.

[34] *Yukhimuk A. K., Kotsarenko N. Ya., Yukhimuk V. A.* Nonlinear interaction of Alfvén waves in solar atmosphere // Proc. 26th ESLAB Symp. Killarny, 16-19 June, Noordwijk, 1992.–P. 337–341.

[35] *Yukhimuk V. A., Voitenko Yu. M., Fedun V. M., Yukhimuk A. K.* Generation of kinetic Alfvén waves by upper-hybrid pump waves // J. Plasma Physics.–1998.–**60**, N 3.–P. 485-495.

THE FOKKER–PLANCK EQUATION IN THE SECOND ORDER PITCH ANGLE APPROXIMATION AND ITS EXACT SOLUTION

B. A. Shakhov[1], **M. Stehlik**[2]

[1]*Main Astronomical Observatory, NAS of Ukraine*
27 Zabolotnoho St., 03680 Kyiv, Ukraine
e-mail: shakhov@mao.kiev.ua

[2]*Institute of Experimental Physics, Slovak Academy of Sciences*
47 Watsonova, 04001 Košice, Slovakia

In contrast to the Boltzman scattering of particles, when the existence of the unscattered particles is possible, the Fokker-Plank scattering can not be used to identify the unscattered particles on the background of the scattered ones. For the case of the Boltzman scattering of particles the kinetic equation describing this process may be solved exactly for all angles. From the other hand the Fokker-Plank kinetic equation is more complex. Here the exact analytical solution of the Fokker-Plank kinetic equation to the second order pitch-angle approximation is given.

Let us consider the following equation:

$$\partial_t f + v \cos\theta \; \partial_x f = \frac{v}{\lambda \sin\theta} \; \partial_\theta \sin\theta \; \partial_\theta f + \delta(x) \; \delta(t) \; \frac{\delta(\theta-\theta_0)}{\sin\theta_0} \, . \tag{1}$$

Here θ is the particle pitch angle (the angle between velocity vector and the axis x) , λ is the particle mean free path ($\lambda = v/v_s$, v_s is the scattering frequency). Introducing the dimensionless variables $y = x/\lambda$ and $\tau = vt/\lambda$, Eq. (1) can be written in the form

$$\partial_\tau f + \mu \; \partial_y f = \partial_\mu f (1-\mu^2) \; \partial_\mu f + \frac{1}{\lambda} \delta(y) \; \delta(\tau) \; \delta(\mu - \mu_0) \, , \tag{2}$$

where $\mu = \cos\theta$. Taking the Fourier transform of the space variable y and the Laplace transform of the time τ, Eq. (2) gives

$$\partial_\mu (1-\mu^2) \; \partial_\mu f - \mathrm{i} k \mu f - s f = -\frac{1}{\lambda} \delta(\mu - \mu_0) \, . \tag{3}$$

Solutions of Eq. (3) are expressed by the Coulomb – spheroidal functions with indefinite parameters [1] and some approximations are necessary. The simplest approximation corresponds to very small pitch angle θ, when one can put $\sin\theta \to \theta$ and $\cos\theta \to 1$. In the other words the equality $\sin^2\theta + \cos^2\theta = 1$ is fulfilled up only to the first order of θ. In this case one find

$$\partial_\tau f + \partial_y f = \frac{1}{\theta} \; \partial_\theta \; \theta \; \partial_\theta f + \frac{1}{\lambda} \delta(y) \; \delta(\tau) \frac{\delta(\theta - \theta_0)}{\theta_0} \, . \tag{4}$$

This equation including the focusing term has been investigated by Toptygin *et al.* [2] and Kats *et al.* [3, 4] for the stationary and non-stationary case, respectively. The solution of Eq. (4) reads

$$f(y, \tau, \theta, \theta_0) = \frac{1}{2\lambda\tau} \; \exp\left[-\frac{\theta^2 + \theta_0^2}{4\tau} \right] \; I_0 \left(\frac{\theta\theta_0}{2\tau} \right) \; \delta(y - \tau) \, , \tag{5}$$

where $I_0(x)$ is the zero order Bessel function of imaginary argument (the hyperbolic Bessel function). The last equation rewritten in the variables $\{x, t\}$ reads

$$f(x, t, \theta, \theta_0) = \frac{\lambda}{2vt} \; \exp\left[-\lambda \frac{\theta^2 + \theta_0^2}{4vt} \right] \; I_0 \left(\lambda \frac{\theta\theta_0}{2\tau} \right) \; \delta(x - vt) \, . \tag{6}$$

The δ-function in Eq. (6) expresses the particle free propagation along the axis x.

Let us consider the second order pitch angle approximation. It means that $\sin\theta \to \theta$ and $\cos\theta \to (1-\theta^2/2)$. The equality $\sin^2\theta + \cos^2\theta = 1$ is fulfilled up to the second order of θ and Eq. (1) reads

$$\partial_\tau f + \left(1 - \frac{\theta^2}{2}\right) \partial_y f = \frac{1}{\theta}\, \partial_\theta \theta\, \partial_\theta f + \frac{1}{\lambda}\, \delta(y)\, \delta(\tau)\, \frac{\delta(\theta - \theta_0)}{\theta_0}\,. \tag{7}$$

Substituting $\eta = \theta^2/4$ changes Eq. (6) to the following

$$\partial_\tau f + (1 - 2\eta)\, \partial_y f = \partial_\eta\, \eta\, \partial_\eta f + \frac{1}{2\lambda}\, \delta(y)\, \delta(\tau)\, \delta(\eta - \eta_0)\,. \tag{8}$$

Taking the Laplace transform of τ and Fourier transform of y one obtains the equation for $f(s, k, \eta, \eta_0)$:

$$\partial_\eta\, \eta\, \partial_\eta f + 2\mathrm{i}k\eta f - (s + \mathrm{i}k) f = -\frac{1}{2\lambda}\, \delta(\eta - \eta_0)\,. \tag{9}$$

Solution of Eq. (9) can be the generalized form of the previous solution (5). For this purpose the solution is sought in the form

$$f = \frac{1}{2\lambda} \int_0^\infty \exp[-\alpha(\eta + \eta_0)\cosh\xi] \left(\coth\frac{\xi}{2}\right)^\beta I_0(2\alpha\sqrt{\eta\eta_0}\sinh\xi)\mathrm{d}\xi \tag{10}$$

with unknown parameters α, β. These are determined the substituting (10) into Eq. (9):

$$\alpha = \sqrt{-2\mathrm{i}k}, \qquad \beta = -\frac{s + \mathrm{i}k}{\sqrt{-2\mathrm{i}k}}\,. \tag{11}$$

Conditions for convergence of the integral (10) are the following: Re $\alpha > 0$, Re $\beta < 0$. Then $\alpha = (1-\mathrm{i})\sqrt{k}$ for $k > 0$ and $\alpha = (1+\mathrm{i})\sqrt{k}$ for $k < 0$, respectively. The inverse Laplace transform exists under condition Re s > 0, therefore, the condition Re $\beta > 0$ is fulfilled for those α and one obtains

$$\begin{aligned} f(k, \tau, \eta, \eta_0) &= \frac{1}{2\lambda}\, \exp\left[-\mathrm{i}k\tau - \alpha(\eta + \eta_0)\, \coth(\alpha\tau)\right] \\ &\times\ I_0\left(\frac{2\alpha\sqrt{\eta\eta_0}}{\sinh(\alpha\tau)}\right) \frac{2\alpha}{\sinh(\alpha\tau)}\,. \end{aligned} \tag{12}$$

The function of the argument k in Eq. (12) is regular relative to the complex value of k, so, one can apply the inverse Fourier transform of (12). Then the solution of Eq. (8) is

$$\begin{aligned} f(y, \tau, \eta, \eta_0) &= \frac{1}{4\pi\lambda} \int_0^\infty \Big\{\exp\Big[\mathrm{i}ky - \mathrm{i}k\tau - (1+\mathrm{i})\sqrt{k}(\eta + \eta_0) \\ &\times\ \coth\left((1+\mathrm{i})\sqrt{k}\tau\right)\Big] \\ &\times\ I_0\left(\frac{2(1+\mathrm{i})\sqrt{k}\sqrt{\eta\eta_0}}{\sinh\left[(1+\mathrm{i})\sqrt{k}\tau\right]}\right) \frac{2(1+\mathrm{i})\sqrt{k}}{\sinh\left[(1+\mathrm{i})\sqrt{k}\tau\right]} \\ &+\ \exp\left[-\mathrm{i}ky + \mathrm{i}k\tau - (1-\mathrm{i})\sqrt{k}(\eta + \eta_0)\coth\left((1-\mathrm{i})\sqrt{k}\tau\right)\right] \\ &\times\ I_0\left(\frac{2(1-\mathrm{i})\sqrt{k}\sqrt{\eta\eta_0}}{\sinh\left[(1-\mathrm{i})\sqrt{k}\tau\right]}\right) \frac{2(1-\mathrm{i})\sqrt{k}}{\sinh\left[(1-\mathrm{i})\sqrt{k}\tau\right]}\Big\}\, dk\,, \end{aligned} \tag{13}$$

or in the $\{x, t, \theta, \theta_0\}$ variables,

$$
\begin{aligned}
f(x,t,\theta,\theta_0) \quad &= \quad \frac{1}{4\pi\lambda}\int_0^\infty \left\{ \exp\left[\frac{\mathrm{i}k}{\lambda}(x-vt) - (1+\mathrm{i})\frac{\sqrt{k}}{4}(\theta^2+\theta_0^2) \right.\right. \\
&\times \quad \left. \coth\left((1+\mathrm{i})\sqrt{k}\frac{vt}{\lambda} \right) \right] \\
&\times \quad I_0\left(\frac{(1+\mathrm{i})\sqrt{k}\theta\theta_0}{2\sinh\left[(1+\mathrm{i})\sqrt{k}vt/\lambda\right]} \right) \frac{2(1+\mathrm{i})\sqrt{k}}{\sinh\left[(1+\mathrm{i})\sqrt{k}vt/\lambda\right]} \\
&+ \quad \exp\left[-\mathrm{i}\frac{k}{\lambda}(x-vt) - (1-\mathrm{i})\frac{\sqrt{k}}{4}(\theta^2+\theta_0^2)\coth\left((1-\mathrm{i})\sqrt{k}\frac{vt}{\lambda} \right) \right] \\
&\times \quad \left. I_0\left(\frac{(1-\mathrm{i})\sqrt{k}\theta\theta_0}{2\sinh\left[(1-\mathrm{i})\sqrt{k}vt/\lambda\right]} \right) \frac{2(1-\mathrm{i})\sqrt{k}}{\sinh\left[(1-\mathrm{i})\sqrt{k}vt/\lambda\right]} \right\} dk\,. \qquad (14)
\end{aligned}
$$

Eq. (6) can be obtained from (14) as a limit of the small time t. In fact, if t$\to$ 0 Eq. (14) acquires the form

$$
f(x,t,\theta,\theta_0) = \frac{\lambda}{2vt}\exp\left[-\frac{(\theta^2+\theta_0^2)\lambda}{4vt} \right] I_0\left(\frac{\theta\theta_0\lambda}{2vt} \right) \delta\left(x - vt\left(1 - \frac{\theta^2+\theta_0^2}{6} \right) \right)\,. \qquad (15)
$$

One can see from Eq. (15) that both processes of the pitch – angle diffusion and particle transport are connected with each other. To separate them the expansion of cosine into series up to the second order, $\cos\theta = 1 - \theta^2/2$, must be used and after that the term of θ^2 can be neglected in comparison with unit. This gives the Eq. (6).

REFERENCES

[1] *Komarov I. V., Ponomariov L.I., Slavyanov S. Yu.* Spheroidal and Coulomb spheroidal functions.–Moscow: Nauka, 1976.–146 p.

[2] *Gal'perin V. A., Toptygin I. N., Fradkin A. H.* The particles scattering by magnetic irregularities in the strong magnetic field // JETF.–1971.–**60**.–P. 972.

[3] *Dorman L. I., Kats M. E.* About the cosmic ray fluctuations in the interplanetary magnetic field // Proc. V Leningrad Seminar.–1973.–P. 311–321.

[4] *Dorman L. I., Kats M. E.* Cosmic ray kinetics in space // Space Sci. Rev.–1977.–**20**.–P. 529.

DECAMETRIC STORMS OF TYPE III BURSTS

E. P. Abranin[1], L. L. Bazelyan[1], V. N. Mel'nik[1], Ya. G. Tsybko[2]

[1] *Institute of Radio Astronomy, NAS of Ukraine*
4 Chervonopraporna St., 61002 Kharkiv-2, Ukraine
e-mail: `melnik@ira.kharkov.ua`

[2] *Radiophysical Research Institute*
Nizhnii Novgorod, Russia

The results of determination of positions and velocities both usual Type III burst and microburst sources at decameter wavelengths are presented.

The radiotelescopes (such as UTR-2) with high sensitivity allow to carry out investigations of weak Type III bursts (microbursts) with brightness temperatures $T_B \leq 10^8$ K. These investigations are very interesting because the well known hypotheses of exitation don't explain both Type III bursts and microbursts simultaneously.

The microbursts were reported first by Kundu *et al.* [3]. Their observations were made at Clark Lake at four frequencies between 38.5 and 73.5 MHz. The properties of microbursts were confirmed by Subramanian *et al.* [4] approximately in the same frequency range.

These observations showed that the microbursts are low temperature continuation of usual Type III bursts. But their frequency drift rate is well below that obtained from the well known expression for the range $0.1 - 10^3$ MHz [1]:

$$df/dt = -0.01 f^{1.84}. \tag{1}$$

Below we present results and analysis of observations at decameter wavelengths of eight Type III noise storms.

Observations were made in various years of the solar activity cycle at six frequencies in the range from 10 to 25 MHz using UTR-2 telescope. Radiometers with dynamic range 40db could detect both microbursts and usual Type III bursts. Angular sizes of the bursts were calculated by means of empirical dependence of angular size on frequency $\theta = 10^{3.05} f^{-1.14}$ [2, 5]. In our case, the flux densities of microbursts with brightness temperatures $T_B \simeq 10^7$ K are equal to $S_{25} \simeq 1\, s.f.u.$ at 25 MHz.

The electron beam velocity v_b calculated from frequency drift of Type III bursts depend on two alternative possibilities: the bursts are generated in the average corona or in the coronal streamers.

For definition of burst source location the power laws of electron density ($N_e = N(\rho)$) dependence on the height $\rho = R/R_\odot$ for the corona and the several models of coronal streamers were obtained in frequency range 5–25 MHz

$$N_e = N_0 \rho^{-m}. \tag{2}$$

In our calculations the relative errors were less than 10% for all approximations.

The value m is of $m = 5.2$ both for the minimum and the maximum corona models, and $\log N_0$ are equal to 7.9 and 8.1, respectively. The values of m and $\log N_0$ for different streamer models are $2.4 \leq m \leq 4.1$ and $7.87 \leq \log N_0 \leq 7.97$.

For density dependence (2) we have the power law of frequency drift rate on frequency

$$\log df/dt = b_0 + b_1 + \log f, \tag{3}$$

where

$$b_1 = 1 + 2/m, \tag{4}$$

$$b_0 = \log\left(0.22 \times \frac{\beta}{1 - \beta cos\theta} \times \frac{m}{(3.1 \cdot 10^7 N_0)^{1/m}}\right), \tag{5}$$

$\beta = v_b/c$, and θ is the helio longitude of the active region. Flux densities and frequency drift rates were determined for 250 bursts in the range of $10 - 25$ MHz detected in various years of the solar activity cycle.

Using the obtained frequency drift rate we calculated values b_0 and b_1 from Equation (3) by the least square method and then we derived value m from Equation (4) for all bursts.

The analysis of the obtained data allowed us to state that the value $m \approx 2.8$ in the years near the maximum of the solar activity cycle (207 bursts) and $\bar{m} = 4.8$ near the minimum one (24 bursts). These results allow to make the following conclusions:

– the Type III burst sources in the years near maximum of the solar activity cycle are located into streamers;

– value of frequency drift rate calculated according to Equation (1) is higher that for the observed rates and this error increases at high frequencies.

Burst source velocities were calculated by Equation (5) assuming $\log N_0 = 7.9$ and $\theta = 0$. Relative velocities of burst sources β were obtained for the burst flux densities in the range $0.2 - 20\,s.f.u$. It turned out that $0.18 \leq \beta \leq 0.23$, *i.e.*, differences between the velocities of electron beams that generate usual Type II bursts and microbursts are not small.

Acknowledgements. This work was partially supported by INTAS (grant N 96-0183 and N 97-1964).

REFERENCES

[1] Solar and solar-terrestrial physics. Illustrated dictionary of terms / Eds A. Bruzek and Sh. Duran.–Moscow: Mir, 1980.–254 p.

[2] *Abranin E. P., Bazelyan L. L., Goncharov N. Yu., et al.* Angular sizes of stria-burst sources in the range 24-26 MHz // Solar Phys.–1978.–**57**.–P. 229–235.

[3] *Kundu M. R., Gergely T. E., Szabo A., et al.* Solar microbursts at meter-dekameter wavelengths // Astrophys. J.–1986.–**308**.–P. 308–442.

[4] *Subramanian K. R., Gopalswamy N., Sastry Ch. V.* A new investigation of micro-bursts at meter-decameter wavelengths // Solar Phys.–1993.–**143**.–P. 301–316.

[5] *Thejappa G., Gopalswamy N., Kundu M. R.* Microbursts of meter-decameter wavelengths // Solar Phys.–1990.–**127**.–P. 165–183.

THEORY OF RADAR ECHOES FROM THE SUN

V. N. Mel'nik

Institute of Radio Astronomy, NAS of Ukraine
4 Chervonopraporna St., 61002 Kharkiv-2, Ukraine
e-mail: melnik@ira.kharkov.ua

The plasma theory of radar reflection from turbulence generated by Type III electrons is considered. This theory allows to explain the main results of the well-known James experiments.

From 1961 to 1969 James [6, 7] observed the solar radio echoes at 38 MHz with surprisingly high bandwidth and intensity. The typical bandwidth was found of about 40 kHz with quasisymmetrical profiles. He obtained the high (up to $800\pi R_\odot^2$), moderate ($\approx 1 - 2\pi R_\odot^2$) and low ($< \pi R_\odot^2$) values of scattering cross section, σ. In accordance with James the echo scattering occurs mainly in the heights range from 1.3 to $1.6 R_\odot$. All these properties cannot be explained assuming reflection from the plasma layer (where the radar, ω_0, and Langmuir plasma, ω_{pe}, frequencies become equal) [1]. Other models by Gordon [4], Gordon *et al.* [5] Wentzel [11] and Chashei and Shishov [2] also failed in the main James' results interpretation.

In 1999 [8, 9] the plasma theory of radar reflection was proposed. According to the theory, a radar signal is scattered by both the anisotropic Langmuir and ion-sound turbulences generated by Type III electrons. The assumptions regarding the anisotropic turbulence were made. Electrons generate Langmuir waves with the spectral energy density $W_+(\vec{k}_l)$ along the direction of their propagation into a cone with angle $\varphi_l (\approx 10^\circ - 20^\circ)$. There is turbulence $W_-(\vec{k}_l)$ in the opposite direction in the same cone because of the process $l + i = l + i$ that changes plasmon wave vector direction, $\vec{k}_l' = -\vec{k}_l$. Turbulence in other directions, $W_\perp$, is not so significant: $W_\perp \ll W_+$. The Langmuir turbulence is concentrated near wave number $k_l^* \approx \omega_{pe}/v_{ph}$ (v_{ph} is phase velocity which is approximately equal to electron velocity v_0) with width $\delta k_l = k_l^*/3$. Since electron flux density $n'/n = 10^{-5} - 10^{-7}$ the turbulence energy density $W_l/nT \approx (n'/n)(mv_0^2/mv_{Te}^2) = 10^{-3} - 10^{-5}$ at $v_{Te} = 5\times10^8$ cm/s and $v_0 = 0.3\,c$. This turbulence occupies the corona volume with the length along the direction of electron propagation $\triangle z \approx v_0 \triangle t$ (axis $z \parallel \vec{v}_0$ and $\triangle t$ is the burst duration) and cross section, S, in the perpendicular plane that coincides with the visible site of Type III bursts.

For a description of the spectral energy density of electromagnetic waves $W_t(\vec{k}_t)$ we use the kinetic equation

$$\frac{\partial W_t(\vec{k}_t)}{\partial t} + \vec{v}\frac{\partial W_t(\vec{k}_t)}{\partial \vec{r}} = I, \tag{1}$$

where I is the collision integral of electromagnetic waves with other waves and particles, and $\vec{v}_{gr} = \partial\omega_t/\partial\vec{k}_t$ is the photon group velocity. The photon interacts with Langmuir plasmons through the different processes: $t + l = t + l$, $t + l = t$ and others. It is shown below that the main properties of the reflected signals can be obtained through the processes $t + l = t + l$ of radar scattering by the anisotropic turbulence.

Taking into account that electrons propagate along the open magnetic field lines, which coincides with the direction of coronal density decrease, and that $W_t \ll W_l$ Equation (1) takes the form

$$\frac{\partial W_t(\vec{k}_t)}{\partial t} + v_{gr} cos\theta \frac{\partial W_t(\vec{k}_t)}{\partial z} = a - bW_t(\vec{k}_t), \tag{2}$$

where a and b are emissivity and scattering coefficients, respectively. θ is an angle between $\vec{v}_0$ and $\vec{k}_t$.

In order that the radar wave interacts with Langmuir turbulence effectively the optical thickness $\tau = \triangle z b/v_{gr}$ needs to be ≥ 1. It can be shown that $\tau \ll 1$ at the altitudes where $\omega_{pe} \ll \omega_0$. So, electromagnetic waves do not interact with the turbulence in the higher corona. First $\tau \approx 1$ when $k_l^* \approx k_t$ (k_l and k_t are wavenumbers of interacting waves) or $\omega_{pe} \approx \omega_0 v_{ph}/c$.

Let us consider the scattering of electromagnetic wave (t) by plasmon (l), when electrons move i) from the Sun to the Earth and ii) away from the Earth.

In the first case, b reaches its maximum when the wave (t) is scattered by plasmon (l) from W_+ with moving to W_- [8, 9]. Then the scattered wave (t') propagates towards the Earth into the solid angle $\Omega \approx \pi\varphi_l^2$. For b one has

$$b \approx \frac{\pi^4}{16}\omega_0(\frac{\omega_p}{\omega_0})^3\frac{W_+W_-}{(nT)^2}\frac{v_0}{c}\frac{k_l^*}{\delta k_l}. \tag{3}$$

$b \approx 4-40$ s^{-1} at $W_+/nT \approx W_-/nT = 10^{-3}$, $\varphi_l = 1/3-1/6$, $\delta k_l/k_l^* = 1/3$ and the optical thickness is more than 1. Since there is the backscattering into preferred direction, the amplification should be $4\pi/\Omega$ [11] and cross section $\sigma \approx 4\pi S/\Omega = 4S/\varphi_l^2 = 10 \div 100S$ is roughly compared with the cross section of solar disk $\pi R_\odot^2$ at 40 MHz. So, $\sigma = 10-100\pi R_\odot^2$.

In the second case, b has a maximum when the scattered wave (t') is directed away from the Earth [8]. The scattered wave (t') comes in the direction of the Earth if plasmon moves from W_+ to $W_\perp$. In this case, parameter b is expressed by Equation (3) when $W_\perp$ is replaced by W_-. So, $\tau < 1$ because of $W_\perp \ll W_+$ and, consequently, the radar echo observed has a small cross section $\sigma < S$ or $\sigma < \pi R_\odot^2$ at 40 MHz.

Thus, when active regions are close to the center of the solar disk (case i), the radar cross sections increase, and when these regions are on the limb (case ii), the cross sections decrease. A similar tendency was found from analysis of James' experiments [4, 3].

Bandwidth of radar echoes in our model is determined by T_e, $\delta k_l/k_l^*$, v_{ph} and has the form

$$\triangle\omega_t = \omega_t - \omega_t' \approx 3\omega_0\frac{\omega_{pe}}{\omega_0}\frac{v^2k_l^*\delta k_l}{\omega_{pe}^2} \tag{4}$$

The observed values from 20 kHz to 60 kHz can be easily obtained for reasonable choices of parameter values.

If there are regions with $T_e > T_i$ in the solar corona then Langmuir turbulence is source of ion-sound waves due to processes $l = l + s$. The spectrum of these waves is from $k_s = 2\omega_{pl}/v_{ph}$ to $1/r_{De}$, and their level is $W_{s\pm} = 10^{-2}W_l$ [10]. The numerical analysis of scattering processes $t + s = t$ shows that $\tau \approx 1$ can be realized up to $R = 5R_\odot$. These are precisely the maximum altitudes observed in James' experiments [6]. Frequency shifts of reflected signals for processes $t + s = t$ $\triangle\omega = \omega_0(T_e/Mc^2)^{1/2}$ are defined by electron temperature and equal to 10 kHz – 20 kHz that also are close to the observed values [7].

According to the plasma theory the main reflections occur in the region $R = 1.3-1.6R_\odot$ due to processes $t + l = t + l$, and beyond $1.6R_\odot$ in the regions with nonisothermal plasma due to processes $t + s = t$.

Acknowledgements. This work was partially supported by INTAS (grant N 96-0183 and N 97-1964).

REFERENCES

[1] Bass F. G., and Braude S. Ya. To the problem of radar reflection from the Sun // Ukr. Fiz. Zh.–1957.–**11**, N 2.–P. 149–164.

[2] Chashei I. V., Shishov V. I. Volume scattering model for interpretation of solar radar experiments // Solar Phys.–1994.–**149**.–P. 413–416.

[3] Gerasimova N. N. To plasma theory of radar signals and their connection with the solar activity // IRE Cand. fiz-math. nauk thesis.–Kharkiv, 1975.–123 p.

[4] Gordon I. M. Radar researches of the Sun and cosmic plasma turbulence // IRE Doct. fiz.-math. nauk thesis.–Kharkiv, 1974.–218 p.

[5] Gordon I. M., Liperovsky V. A., and Tsytovich V. N. Turbulence spectrum in solar coronal plasma and structure of radar echoes // Sov. Astron. Zh.–1971.–**48**.–P. 70–83.

[6] James J. C. Radar studies of the Sun at 38MC/s // Astrophys. J.–1966.–**146**, N 2.–P. 356–366.

[7] James J. C. MIT Center of Space Res. Technical Report 70-2, Febr. 1970.–89 p.

[8] Mel'nik V. N. Radar scattering by anisotropic Langmuir turbulence // Solar Phys.–1999.–**184**.–P. 363–367.

[9] Mel'nik V. N. On the plasma theory of reflection of a radar signal from the Sun // Astron. Lett.–1999.–**25**.–P. 336–340.

[10] Mel'nik V. N. Plasma theory of solar radar echoes after thirty years // Abstract Book of IAU 24th General Assembly (Manchester, 7-18 August, 2000).–2000.–P. 171.

[11] Wentzel D. G. New interpretation of James's Solar radar echoes involving lower-hybrid waves // Astrophys. J.–1981.–**248**, N 3.–P. 1132–1143.

RADIO PROBING OF THE PERTURBATIONS ORIGINATING IN THE NEAR–EARTH PLASMA FROM NATURAL AND ANTHROPOGENIC ENERGY SOURCES

L. F. Chernogor, L. S. Kostrov, and V. T. Rozumenko

Department of Space Radio Physics, V. Karazin Kharkiv National University
4 Svoboda Square, 61077 Kharkiv, Ukraine
e-mail: Leonid.F.Chernogor@univer.kharkov.ua

INTRODUCTION

There are many papers concerned with search of the effects caused by rocket launches. They describe generally the effects occurring along the trajectory of a lifting rocket. The processes occurring at distances of $\sim 1,000 - 10,000$ km from the launch site and the rocket trajectory are investigated in this paper. Such perturbations are called large-scale or global-scale.

The comprehensive method and technique for search of the effects of rocket engine burns in the bottomside ionosphere (heights of $100 - 300$ km) are used in this study. It is important that observations were carried out for different rocket families at different ranges from launch sites, for different moments of a day- and night-time, and under different geophysical conditions.

TECHNIQUE

Non-stationary processes in the bottomside ionosphere have been studied with an HF Doppler radar taking vertical incidence measurements. The measurements were performed at 2.8 MHz and 3.0 MHz during $4 - 6$ hr period, beginning at 2–3 hr before the event. The data recording system acquired measurements at a repetition rate of 100 per second, which were subjected to a fast Fourier transform, and Doppler spectra were computed in a frequency band of –1 Hz to +1.5 Hz on 51.2 s time intervals with ~ 0.02 Hz resolution. In the case of quasi-periodic processes with periods of $T \approx 10 - 60$ min, a spectral analysis was undertaken on 128 min or 256 min intervals.

The minimum range to a launch site is $R \sim 700$ km, the maximum R is of about 10,000 km. The most distant sites are Edwards and Vandenberg (USA), the most "southern" site is Kourou (France), the nearest launch site is Kapustin Yar (Russia), and the most "northern" is Plesetsk.

LARGE–SCALE PERTURBATIONS DURING ROCKET BURNS

The Soyuz rocket was launched at 13:22 UT on October 18, 1999 (see Figure 1). Before the launch the ionosphere remained quiet. From about 12:55 UT to 13:03 UT, the main and additional modes of the reflected signals were observed, and a quasi-periodic process appeared with the period $T \approx 10$ min. After 13:45 UT, the amplitude of the oscillations increased significantly (amplitude of Doppler shift attained $f_{Da} = 0.5$ Hz), and the oscillation with $T \approx 20$ min became predominant over a period of about 30 min. Between 14:12 UT and 14:40 UT, the ionosphere was practically undisturbed. During the 14:40 – 14:50 UT interval, in addition to the principal mode of the signal, an additional mode shifted by $f_D = 0.3$ Hz (f_D is the Doppler shift) was recorded. After 14:50 UT, the disappearance of its persistent maximum was observed. This provides evidence to the appearance of random irregularities in the ionosphere below the reflection height (approximately of 150 km). Such perturbations persisted for more than 1 hr. In addition, the sunset at the ground occurred approximately at 15:20 UT and an hour later at the reflection level.

GLOBAL–SCALE PERTURBATIONS ASSOCIATED WITH ROCKET ENGINE BURNS

The Space Shuttle Endeavor was launched at 08:35 UT on December 4, 1998 (see Figure 2). On this day, the ionosphere was disturbed, and the effect of spectrum spreading was recorded during the whole period of observation. Prior to and shortly after the lift-off, a quasi-periodic process with $T \approx 10$ min and $f_{Da} \approx 0.1$ Hz was observed. Between 08:50 UT and 09:25 UT the ionosphere remained relatively quiet, and from 09:25 UT

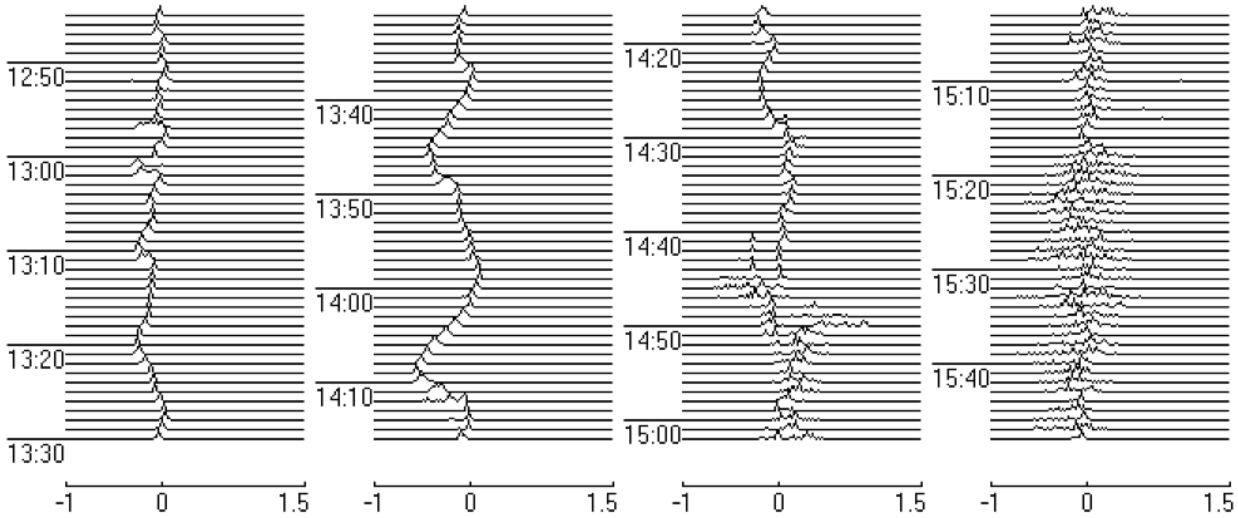

Figure 1: Doppler spectra acquired after Soyuz rocket launch at 13:22 UT on October 18, 1999

to 10:00 UT a significant spectrum spreading, as well as a quasi-periodic process with $T \approx 15 - 20$ min were recorded. At 10:05 UT to 10:10 UT, an additional mode appeared with the maximum Doppler shift of 0.5 Hz. After 10:22 UT, a spectrum spreading persisted for a long time interval, and a quasi-periodic process with amplitude of 0.2 Hz and $T \approx 10$ min occurred.

The launch of a rocket occurred at 21:04 UT on February 7, 1999. Approximately at 21:10 UT, an additional mode and the quasi-periodic process with $T \approx 8 - 10$ min, $f_{Da} \approx 0.1$ Hz, and $\Delta T \approx 40$ min appeared. After 21:50 UT, the ionosphere remained quiet, and within the 22:05 – 22:25 UT time interval, an abrupt decrease in f_{Da} by $0.4 - 0.6$ Hz and spectrum spreading occurred. After 22:25 UT, the ionosphere remained quite undisturbed, and the faintly discernible quasi-periodic process with $T \approx 25$ min and $f_{Da} \approx 0.10 - 0.15$ Hz occurred.

GLOBAL–SCALE PERTURBATIONS DURING SPACE VEHICLE LANDINGS

Over the interval 14:35 – 15:24 UT during the Space Shuttle landing at 17:04 UT on November 7, 1998, the Doppler spectra variations exhibited the $T \approx 10$ min periodicity with $f_D \approx 0.2 - 0.4$ Hz, and the signal remained one-mode or two-mode with small frequency variations in the second mode. The sharp decrease of $0.5 - 0.6$ Hz in f_D occurred between 15:24 UT and 16:05 UT, and even of 1 Hz between 15:46 – 15:50 UT. The next significant decrease in f_D was recorded over the 16:22 – 16:55 UT interval, and between 16:42 UT and 16:55 UT the signal was two-mode and the difference reached values up to 1 Hz. After 17:00 UT, the ionosphere remained weakly perturbed. During the interval 18:00 – 18:50 UT, marked variations in f_D of not more than 0.5 Hz and two modes were observed. We have to point out that the sunset at the ground occurred at 14:30 UT, and almost an hour later in the lower part of the F region.

DISCUSSION

The additional mode with $-0.2 \div -0.3$ Hz shift with the delay of about $60 - 80$ min for the day and night or Doppler spectrum spreading is the characteristic feature of launching sites removed from the observation site at 2,500 km. The duration of these effects is of $5 - 10$ min, and the apparent propagation speed of the perturbations is of about $410 - 570$ m/s. The speed of such an order of magnitude is a characteristics of the acoustic waves.

The faster perturbations associated with a rocket launch are observed in Doppler data randomly. Quasi-periodic processes arose in the ionosphere soon ($\Delta t \approx 2 - 4$ min) after the launch of rockets on March 22, 1999 and October 18, 1999. These time delays correspond to speeds of $v \approx 10 - 20$ km/s. Such propagation speeds are distinctive features of the gyrotropic waves in the plasma of the ionospheric E and F regions. Since rockets of the same family (Proton) were launched on March 21, 1999 and on July 5, 1999, but the latter launch was to be not followed by quasi-periodic processes, then it could be suggested that the oscillation observed on March 21, 1999 was of natural origin. In addition, it is necessary to take into account that the first launch occurred at night and the second one at the day-time, that is under vastly different conditions. It cannot be discarded such a fact that on July 5, 1999 the rocket exploded at the height up to 120 km did not possibly reach the region

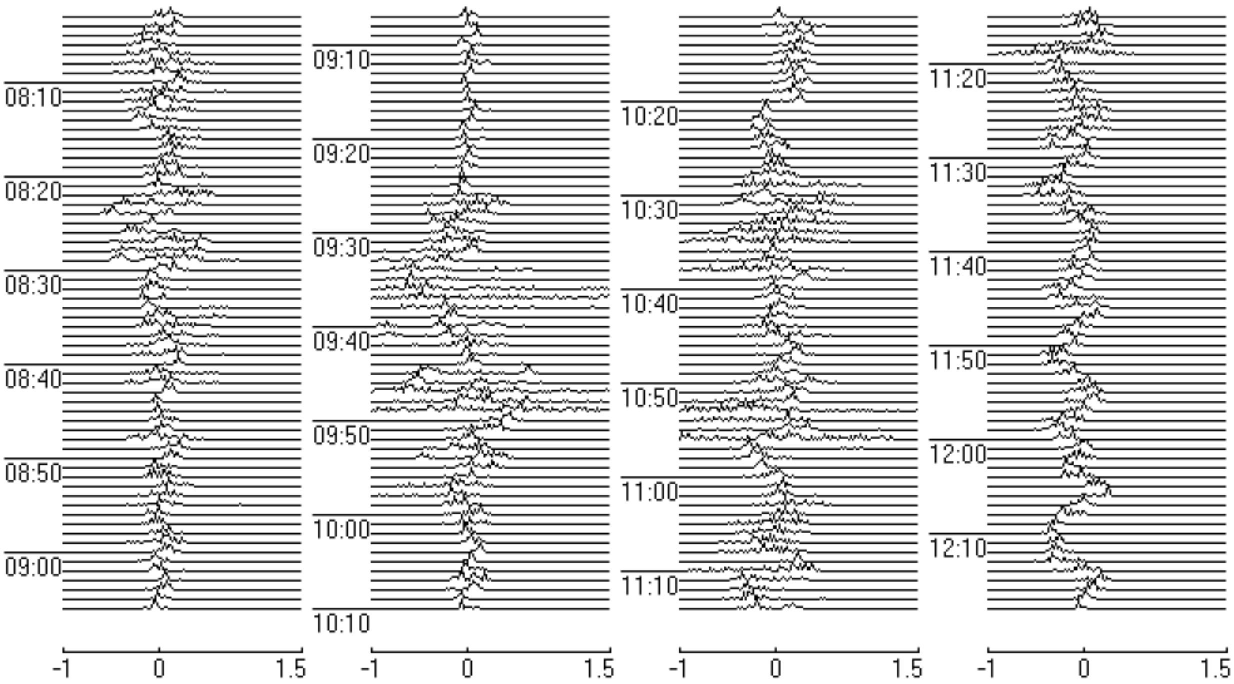

Figure 2: Doppler spectra acquired after the Space Shuttle Endeavor launch at 08:35 UT on December 4, 1998

where the gyrotropic waves were effectively generated. Regarding the acoustic momentum from the explosion, it was apparently observed from 15:04 UT to 15:05 UT and from 15:08 UT to 15:09 UT.

Next, consider global-scale perturbations. Thirty-two launches of space vehicles of different rocket families have been examined. A steady enough ionospheric response to launches from launch sites in the USA and France was observed most often in $60-80$ min after their launch. The trajectories of the rockets differed, and this could explain the variations in delay of $60-100$ min. The apparent speed is equal to $v \approx 2-3$ km/s, provided that the mean value $R \approx 10,000$ km. Such propagation speeds are exhibited by the slow MHD waves in the ionosphere. They are weakly attenuated, and, therefore, could transfer global-scale perturbations. A mechanism for perturbation transfer could be as follows. The perturbations are not from zero and first rocket stages, but from orbital maneuvering system engine burns. Although their power is significantly lower, it should be taken into account that they release the exhaust gases directly into the plasma, and electromagnetic and MHD waves are effectively generated in this case. The perturbations are often observed with delays of $6-7$ min ($R \approx 9,000-$ 10,000 km) and duration of tens of minutes, which correspond to a speed of 25 km/s. As mentioned above, the gyrotropic waves have such speeds.

Let us consider possible global-scale effects occurring during space vehicle landings. Six landings of Space Shuttle Orbiters have been examined. A steady enough ionospheric response was observed to occur $70-90$ min prior the landing with the temporal duration of tens of minutes. For example, for landing on December 28, 1999, the delay of 12 min was determined from the decrease in direct bias in a long-period Doppler shift and from the appearance of new spectral components with $T \approx 2$ min, $T \approx 4$ min, and $T \approx 8$ min, giving an apparent perturbation transfer speed of a few tens of km/s.

The second group of quasi-periodic perturbations has delays of $\Delta t \approx 80$ min, $\Delta T \approx 40$ min, and $T \approx 10$ min and $T \approx 20$ min. Provided these processes are associated with deorbit burns of orbital maneuvering system engines, their apparent speed is of the order of unit of km/s. The slow MHD waves have the same speeds.

CONCLUSIONS

1. Acoustic perturbations (sound and acoustic gravity waves) propagate from rocket engines along the earth's surface in the ionosphere at distances not less than 2,300 km. The ionospheric F region often becomes turbulent and Doppler spectra spread after the arrival of these perturbations.

The perturbations are quite often observed to exhibit propagation speeds vastly exceeding the limits of ionospheric acoustic propagation at distances up to 2,300 km from a rocket. They have velocities of $10-20$ km/s. This statement, however, needs further investigations.

2. Global-scale perturbations are observed in the ionosphere during rocket launches at distances of about 10,000 km. The mechanism for their transfer might be linked to both main engine burns in the near-earth atmosphere and orbital maneuvering system or upper rocket stage burns in the ionosphere. The latter suggestion is preferable because the mechanism for the generation of electromagnetic and MHD waves by a plasma jet in the plasma is well understood, and the waves in question are most probably the gyrotropic waves. According to our observations, they have speeds of $10-25$ km/s.

3. Approximately $60-80$ min before the landing of a space vehicle, perturbations are recorded a few tens of minutes in duration, which is plausibly associated with deorbit burns of orbital maneuvering system engines. The apparent propagation speeds of these perturbations are of about $10-20$ km/s, while for the second group of perturbation $v \approx 2-3$ km/s.

4. Three groups of speeds are observed in these experiments: $0.5-0.7$ km/s and less, $2-3$ km/s, and $10-25$ km/s. They apparently correspond to the acoustic and acoustic gravity waves, the slow MHD waves, and the gyrotropic waves, respectively.

Acknowledgements. The authors used the data collected in the database created in V. Karazin Kharkiv National University during a period of the research project supported by STCU grant 471.

SENSITIVITY OF THE SPORADIC-E IRREGULARITY SPECTRUM TO THE ION COMPOSITION OF THE LAYER

Yu. Kyzyurov

Main Astronomical Observatory, NAS of Ukraine
27 Zabolotnoho St., 03680 Kyiv, Ukraine
e-mail: kyzyurov@mao.kiev.ua

Plasma density irregularities in sporadic-E layers below the turbopause level are resulted from the action of turbulence in the neutral atmosphere. A possible dependence of the spectrum of irregularities on the sporadic-E ion composition is considered in this paper. The consideration is based on an analytic expression for the irregularity spectrum. It is shown that the rms level of the relative plasma density fluctuations caused by neutral turbulence and the shape of their spectrum should be sensitive to changes in the metal ion concentration in the layer. The rms fluctuation and the slope of the irregularity spectrum increase with increasing the concentration of metallic ions in the sporadic-E. These changes in the spectrum and in the fluctuation level are explained by the reduction in the recombination rate and by the increase in the mean ion mass.

INTRODUCTION

It is known that the wind-shear mechanism can produce sporadic-E (E_s) layers in the auroral and mid-latitude ionosphere [9, 10]. This mechanism provides a redistribution of ionization through the interaction of the plasma imbedded in the neutral wind with the geomagnetic field under the appropriate vertical profile of the horizontal wind velocity. The mechanism is not very effective for the molecular ions which make up the greater part of the total ion content, since these have a lifetime less than the formation time of the layer; rather, the process acts on atomic metal ions (produced as a result of meteoric influx). These are thought to have very long lifetimes in the E-region, since the recombination reaction for monatomic ions is very slow compared to the dissociative recombination of molecular ions. The data of observations show that the ion composition of sporadic-E usually differs from that of the normal E-region (NO^+ and O_2^+), and most of the ions at the E_s peak are often metallic such as Fe^+ and Mg^+ [9, 10]. In addition, if the sporadic-E is not above the turbopause, the neutral air turbulence plays an important role in the E_s formation [2]. Due to turbulent mixing, various values of concentration of metal ions can be expected in the layer. Changes in the concentration of such ions provide changes in values of the effective recombination coefficient, α_r, and mean ion mass, m, [1, 9]. It is also evident that plasma irregularities are generated by neutral air turbulence in sporadic-E. The present report is devoted to the study of the ion composition sensitivity of such plasma irregularities. In particular, here we discuss the irregularity spectra, which can be measured during rocket experiments in sporadic-E layers for three cases of values of the iron ion concentration.

EFFECT OF IRON ION CONCENTRATION ON SPORADIC-E PLASMA IRREGULARITIES

A starting point of our consideration is an expression for the three-dimensional spectrum, $P(\mathbf{k})$, of plasma density fluctuations produced by neutral turbulence in a weakly ionized gas of the lower ionosphere [4]:

$$P(\mathbf{k}) =(4\pi\Gamma(k))^{-1}(L_N^{-2}k^{-2}(\mathbf{n}\times\mathbf{k})^2 + \frac{\Omega^2}{\nu^2}(\mathbf{b}\times\mathbf{k})^2)\cdot C_1\varepsilon^{2/3}k^{-11/3}, \tag{1}$$

where

$$\Gamma(k) = (2\alpha_r N_0 + (D_a+\mu_n)k^2 + 2\varepsilon^{1/3}k^{2/3})\cdot(2\alpha_r N_0 + D_a k^2 + \varepsilon^{1/3}k^{2/3}). \tag{2}$$

Here L_N is the length scale of the gradient of mean plasma density N_0, $\mathbf{n} = L_N\cdot N_0^{-1}\nabla N_0$ is the unit vector along the gradient, $\mathbf{b} = \mathbf{B}/B$ is the unit vector along the geomagnetic field $\mathbf{B}$, $\Omega = eB/mc$ is the ion gyrofrequency, ν is the ion-neutral collision frequency, C_1 is a dimensionless constant of order unity, ε is the rate of dissipation of turbulent energy per unit mass, D_a is the ambipolar diffusion coefficient, μ_n is the kinematic viscosity of neutral gas. In our case $D_a \approx \mu_n$.

Expression (1) describes plasma fluctuations with wavenumbers $L_N^{-1} < k < k_d$ ($k_d = (\varepsilon/\mu_n^3)^{1/4}$ is the Kolmogorov dissipation wavenumber) and permits an rms level of the relative plasma density fluctuations, $< \delta N^2/N_0^2 >^{1/2}$, to be estimated:

$$\langle \frac{\delta N^2}{N_0^2} \rangle = \int P(\mathbf{k}) \mathrm{d}\mathbf{k} = \int_{k_1}^{k_2} P_1(k) \mathrm{d}k, \tag{3}$$

where

$$P_1(k) = \frac{2}{3\Gamma(k)} \cdot (L_N^{-2} + \frac{\Omega^2}{\nu^2} k^2) \cdot C_1 \varepsilon^{2/3} k^{-5/3} \tag{4}$$

($P_1(k)$ is the one-dimensional power spectral density (1D PSD) of fluctuations and may be convenient for explaining possible changes in the spectral form resulted from changes in a relative role of various processes in the creation of irregularities of different scales [5]). Estimates of the rms fluctuation level with use of (3) for three cases of possible Fe^+ concentration in the layer are presented in Table 1 ($k_1 = 10^{-3}$ m^{-1}, $k_2 \leq k_d \approx 0.2$ m^{-1}). An increase in the concentration of heavy metallic ions (Fe^+) results in both the reduction in α_r [1] and increase in m [3], hence, the ratio Ω/ν decreases ($\Omega/\nu = (m_0/m)\Omega_0/\nu$, m_0 is the mean ion mass for the ion composition of the normal E-region). Taking into account arguments presented in [6] when diffusion of heavy gas of small concentration in light gas was considered, we may neglect possible changes in D_a and ν resulted from the increase in m. In all these cases the values of L_N, N_0, ε, Ω_0/ν, and D_a defined in (2)–(4) are fixed as follows: $L_N = 3 \times 10^3$ m, $N_0 = 10^{11}$ m^{-3}, $\varepsilon = 0.1$ m^2 s^{-3}, $\Omega_0/\nu = 0.01$, $D_a \approx \mu_n = 4$ m^2 s^{-1} (the values correspond to the altitude about 95 km).

Table 1: Dependence of values of m, α_r, and $< \delta N^2/N_0^2 >^{1/2}$ on the Fe^+ concentration in the sporadic-E

Case	Fe^+, %	m, a.m.u.	α_r, m^3 s^{-1}	$< \delta N^2/N_0^2 >^{1/2}$, %
1	0–10	~ 31	$\sim 3.8 \times 10^{-13}$	~ 1.7
2	40	~ 41	$\sim 2.5 \times 10^{-13}$	~ 2.3
3	70	~ 50	$\sim 1.5 \times 10^{-13}$	~ 3.4

Figure 1 (dashed lines) shows self-normalized spectra, $P_1(k)/P_1(k_1)$, for all three cases of Fe^+ concentration (line numbers = case numbers, a straight line represents the Kolmogorov law $k^{-5/3}$). The use of (4) is quite valid when irregularities are isotropic.

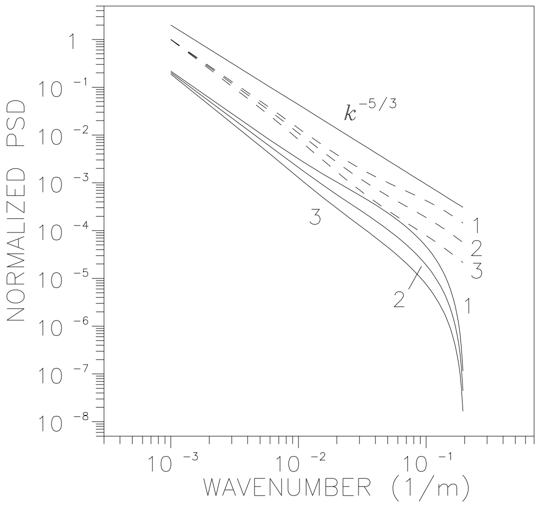

Figure 1: Normalized spectra of plasma density fluctuations under different values of Fe^+ concentration in the sporadic-E predicted by (4), $P_1(k)/P_1(k_1)$ (dashed lines), and by (5), $S_1(k_z)/P_1(k_1)$ (solid lines); the straight line represents the slope of the Kolmogorov spectrum

However, because of dependence on $\mathbf{n}$ and $\mathbf{b}$ in (1) the irregularity spectrum is not quite isotropic. Therefore, in order to predict the spectrum expected from an experiment (if the direction of measurement is along the z axis) a 1D spectrum in other form can be derived by use of $P(\mathbf{k})$, (1), namely,

$$S_1(k_z) = \int_0^{\sqrt{k_d^2-k_z^2}} k_\perp \mathrm{d}k_\perp \int_0^{2\pi} P(k_\perp \cos\varphi, k_\perp \sin\varphi, k_z)\mathrm{d}\varphi = \int_0^{\sqrt{k_d^2-k_z^2}} S(k_\perp, k_z) k_\perp \mathrm{d}k_\perp \tag{5}$$

with

$$S(k_\perp, k_z) = (4\Gamma(k))^{-1}(2L_N^{-2}k_\perp^2 + \frac{\Omega^2}{\nu^2}k^2(k_\perp^2 + k_\perp^2\cos^2\theta + 2k_z^2\sin^2\theta)) \cdot C_1\varepsilon^{2/3}k^{-17/3}, \tag{6}$$

if the sounding rocket trajectory is along the gradient of mean plasma density, $\mathbf{n}(0,0,1)$. Here $k^2 = k_\perp^2 + k_z^2$, $\theta = 90° - I$ is an angle between $\mathbf{b}$ and $\mathbf{n}$, I is the magnetic dip angle (say, in the case of the auroral ionosphere, where electron density fluctuations were measured by rockets during the ROSE project [7, 8], $I \approx 77°$). Solid lines in Fig. 1 represent the normalized spectra, $S_1(k_z)/P_1(k_1)$, for all three cases of Fe^+ concentration. We see that a rise in the concentration of slowly recombining ions in the sporadic-E increases the slope of the irregularity spectrum and the rms level of plasma density fluctuations. Estimates of the plasma fluctuation level and the shape of the irregularity spectrum obtained here do not contradict to the data gained during the ROSE rocket flights [8].

We can see also that $P_1(k)$, (4), is quite acceptable for an analysis of the irregularity spectrum in the wide range of wavenumbers, $L_N^{-1} < k < k_d$, except the wavenumber region near k_d (see Fig. 1). In particular, (4) allows us to conclude that an increase in the concentration of Fe^+ ions leads to broadening the wavenumber range, $L_N^{-1} < k < ((\Omega/\nu)L_N)^{-1}$, in which the plasma irregularities are mainly produced by the turbulent mixing of a background plasma density gradient (since an increase in m decreases the ratio Ω/ν) [5].

CONCLUSIONS

Thus, the ion composition of sporadic-E exerts apparent influence on the shape of the spectrum of plasma density fluctuations created by the neutral atmosphere turbulence. The analysis of the irregularity spectrum under different concentrations of Fe^+ ions in the layer shows that the presence of slowly recombining ions increases the slope of spectrum and the rms level of the plasma fluctuations. Due to change in the ratio of the ion gyrofrequency to the ion-neutral collision frequency, Ω/ν, resulted from change in the mean ion mass, some change in fine structure of the irregularity spectrum can be expected too.

REFERENCES

[1] *Bakhmetyeva N. V., Belikovich V. V., Ignatyev Yu. A., et al.* Determination of the effective recombination coefficient and the meteoric ion concentration in the mid-latitude sporadic-E layer // Geomagn. Aeron.–1996.–**36**, N 6.–P. 36–42.

[2] *Chimonas G.* Turbulent diffusion as a controlling factor in sporadic-E // J. Atmos. and Terr. Phys.–1974–**36**, N 2.–P. 235–244.

[3] *Haldoupis H., Farley D. T., Schlegel K.* Type-1 echoes from the mid-latitude E-Region ionosphere // Ann. Geophysicae.–1997–**15**, N 7.–P. 908–917.

[4] *Kyzyurov Yu. V., Malovichko P. P., Nosov S. F.* Plasma irregularities in a turbulent flow of partially ionized gas. I. Spatial spectrum of plasma density fluctuations in the lower Earth's ionosphere // Kinematics and Physics of Celestial Bodies.–1999.–**15**, N 5.–P. 455–466.

[5] *Kyzyurov Yu. V., Malovichko P. P., Nosov S. F.* Plasma irregularities in a turbulent flow of partially ionized gas. II. Features of spatial spectrum of plasma density fluctuations in the lower ionosphere // Kinematics and Physics of Celestial Bodies.–1999.–**15**, N 5.–P. 467–475.

[6] *Lifshitz E. M., Pitaevskii L. P.* Course of Theoretical Physics, Vol.10. Physical Kinetics.– Moscow: Nauka, 1979.– 528 p.

[7] *Rose G., Schlegel K., Rinnert K., et al.* The ROSE project. Scientific objectives and discussion of first results // J. Atmos. and Terr. Phys.–1992.–**54**, N 6.–P. 657–667.

[8] *Schlegel K.* Measurements of electron density fluctuations during the ROSE rocket flights // J. Atmos. and Terr. Phys.–1992.–**54**, N 6.–P. 715–723.

[9] *Steinweg A., Krankowsky D., Lammerzahl P., et al.* Metal ion layers in the auroral lower E-region measured by mass spectrometers // J. Atmos. and Terr. Phys.–1992.–**54**, N 6.–P. 703–714.

[10] *Whitehead J. D.* Recent work on mid-latitude and equatorial sporadic-E // J. Atmos. and Terr. Phys.–1989.–**51**, N 5.–P. 401–424.

NUMERICAL MODELLING OF THE PITCH–ANGLE SCATTERING AFFECT ON THE RADIATION BELT PROTONS DISTRIBUTION AT LOW ALTITUDES IN THE EARTH MAGNETOSPHERE

O. K. Cheremnykh[1], **V. Ya. Goloborod'ko**[2], **S. N. Reznik**[2]

[1] *Space Research Institute, NAS of Ukraine and National Space Agency of Ukraine, Kyiv, Ukraine*
[2] *Institute for Nuclear Research, NAS of Ukraine, Kyiv, Ukraine*

Numerical simulation was carried out in the present paper to demonstrate the effect of the pitch-angle scattering on the phase space distribution of proton omnidirectional fluxes in the Earth magnetosphere. It was shown that for Mc'Ilvine parameter of order 2–4 even a small order of magnitude of the pitch-angle diffusion coefficient may essentially affects the phase space distribution of the radiation belt proton fluxes. It was also shown that for the purpose of the appropriate description of the protons behaviour at low altitude in the Earth magnetosphere the neutron albedo should be taken into account. Numerical modeling carried out clarifies that for the future predictions on the satellite measurements of proton distributions it is expedient to obtain the reliable theoretical pitch-angle quasilinear diffusion coefficients as well as to have the adequate physical model for the neutron albedo at low altitudes.

INTRODUCTION

Some problems of the protons radiation belt physics are still unsolved. The present report deals mainly with the modeling of the high-energy protons behaviour in the Earth magnetosphere taking into account the wave particle interaction and neutron albedo. This activity was invoked partially by the theoretical investigations [1] as well as the recent experimental observations. It was measured experimentally on board of SAMPEX [2] that the proton flux to the detector originally looked to the zenith observed to be equal after the board spinup to orientate the detector downward to the Earth. These experiments demonstrate that the important impact of the protons come from the "splash" energetic particle albedo. The theoretical problem of interest thus is the energy spectrum and altitude dependence of the neutrons produced by the cosmic ray albedo. At the same time it is obviously that the proton distribution in the radiation belt should be essentially affected by their interaction with the electromagnetic waves in the magnetosphere [3].

SIMULATION APPROACH

We start from the averaged Fokker-Planck equation for trapped protons distribution function in the Earth magnetosphere that will take into account stochastic distortion of the field lines, Coulomb scattering, wave-particle interaction as well as charge exchange with neutral atoms and the proton source due to neutron albedo. To formulate this problem we proceed from the Fokker-Planck type conservation equation in phase space

$$\frac{\partial f}{\partial t} = \frac{1}{\sqrt{g}} \frac{\partial}{\partial c_i} \sqrt{g} \left(d^i + D^{ij} \frac{\partial f}{\partial c_j} \right) + Q - S. \tag{1}$$

Here c_i are the constants of motion chosen as follows: c_1 is the proton magnetic moment, c_2 is the Mc'Ilvine parameter, defined as

$$c_2 = L = \frac{2\pi M}{R\Phi}, \tag{2}$$

where Φ is the magnetic flux through the proton drift trajectory, c_3 is the particle pitch-angle cosine at the equatorial mid plane.

The determinant of the metric tensor is

$$\sqrt{g} = c_3 \tau_b c_2^{-5/2}, \tag{3}$$

where τ_b is the bounce period of the proton drift motion. The value Q in Eq. (1) is the volume proton source due to the neutron albedo taken in the model form [4]

$$Q = Q_o(1-c_3^2)c_1^{-2}c_2^3\exp(-\gamma c_1/\sqrt{1-c_3^2}), \tag{4}$$

where γ corresponds to [4] and Q_o is a parameter for investigation. The value S presents in Eq. (1) is the proton loss due to charge exchange process.

Following [5] we take the boundary conditions as a proton flux energy spectrum at $L = 7$ in the form

$$j = \varepsilon\left(e^{-\varepsilon/60} + 3.5\cdot e^{-\varepsilon/10} + 100\cdot e^{-\varepsilon/1.1}\right). \tag{5}$$

We set natural boundary conditions for all other boundaries in phase space.

METHOD USED

To carry out the numerical simulation of the high energy protons behaviour in the Earth magnetosphere we simplify Eq. (1) as follows.

We treat a steady-state proton distribution function, *i.e.*, $\dfrac{\partial f}{\partial t} = 0$. Coulomb collisions is taken into account as a slowing down process only

$$d^1 = 8.8\cdot 10^{15}L^{9/2}c_1^{1/2}\begin{cases} 205\left(\dfrac{L}{4.1}\right)^{-4.64}, & L < 4.1,\\ 13.0\left(\dfrac{L}{4.1}\right)^{-4.64}, & L > 4.1.\end{cases} \tag{6}$$

Charge-exchange process of the neutral hydrogen with density n_{H_2} is considered in the "tau" approximation [5], with the effective process time τ_{cx}

$$\tau_{cx} = \sigma_\varepsilon\langle n_{H_2}\rangle. \tag{7}$$

Here < ... > denotes the bounce averaging over the proton drift trajectory,

$$\sigma_\varepsilon = \begin{cases} a_1 e^{-\varepsilon/\varepsilon_o}, & L < 2\\ a_2\varepsilon^{-\gamma}, & L > 2\end{cases} \tag{8}$$

with $a_1 = 9.48\cdot 10^{-16}$, $a_2 = 7.55\cdot 10^{-23}$, $\varepsilon_o = 0.0275\,\mathrm{MeV}$, $\gamma = 5.64$ [7], and neutrals assumed to be distributed as follows

$$n_{H_2} = n_o\cdot H^\alpha, \quad n_o = 62544.2, \quad \alpha = -3.7. \tag{9}$$

Exp. (7) fits the experimental data presented in [8].

In our simulation the radial diffusion coefficient is taken in the form [1]

$$D^{22} = D_o L^{10}, \quad D_o = 3\cdot 10^{-14} \tag{10}$$

that corresponds to the magnetic field stochastic distortion (it is suitable for the qualitative description presented here). Pitch-angle diffusion coefficient is taken in the model form [9]

$$D^{33} = \sigma\left(\frac{c_3}{c_{cone}}\right)^\delta \tag{11}$$

with $\sigma = 10^{-6}$ and $\delta = 1.5$ and pitch-angle cosine on the atmospheric loss cone

$$c_{cone} = \sqrt{1 - \frac{1}{L^3\sqrt{4-3/L}}}. \tag{12}$$

SIMULATION RESULTS

The numerical solution of Eq. (1) was made using the alternative direction implicit method for two cases, the first one is without the proton volume source, $Q = 0$, and the second one is with the model neutron albedo taken into account.

The model calculations with the proton flux equal to zero at the loss cone were carried out for the comparison with previous two-dimensional calculations in [8], where the pitch-angle scattering was omitted. The results of our calculations presented in Fig. 1a at least qualitatively reproduced that of [10]. Fig. 1b shows the calculated proton fluxes with proton distribution function equal to zero at the loss cone. From Fig. 1a and Fig. 1b one may see that for $L > 4$ the pitch-angle diffusion does not play the important role for protons distribution. On the other hand, for low values of L parameter the pitch-angle diffusion is significant and decries the omnidirectional proton flux more than to one-tenth of its former value.

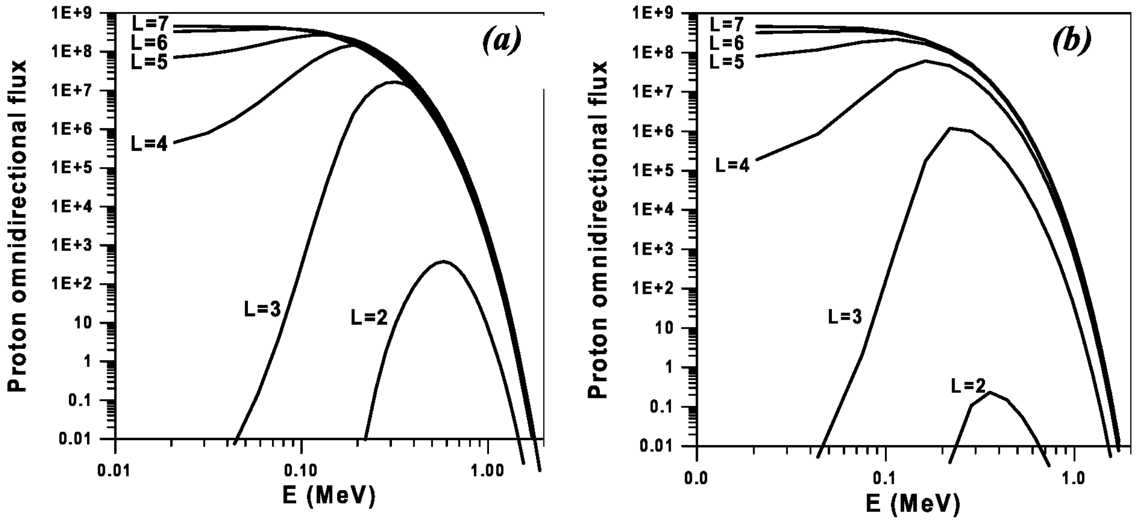

Figure 1: (a) proton flux versus energy for the model when atmospheric cone loss set to be absent; (b) atmospheric cone loss is taken into account

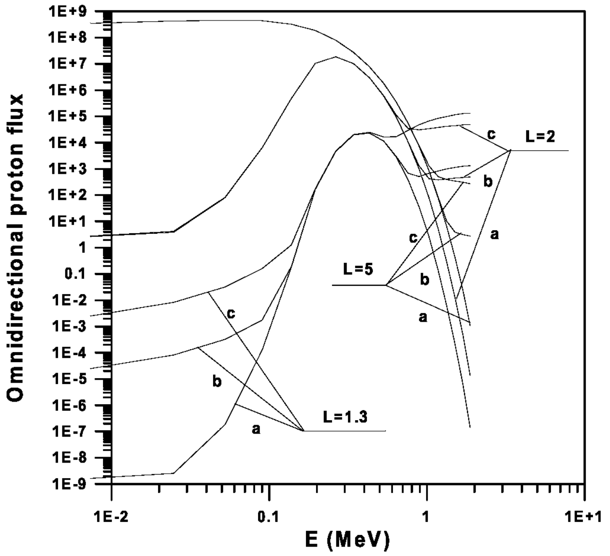

Figure 2: a) volume source is neglected; b) and c) volume source is taken into account, $Q_o(c)/Q_o(b) = 10^2$

Present calculations demonstrate that the pitch-angle scattering plays an important role for the proton flux distribution at low values of Mc'Ilvine parameter even without taking into account the volume source of protons. It should be pointed out that experimental observations show the higher level of the proton fluxes in the low energy region at low altitudes than the calculated ones. It may be explained with taking into account the neutron albedo in the numerical modeling. Numerical simulation results with the volume source in the model form of Eq. (4) are presented in Fig. 2. As the volume source amplitude is not well known, calculations were carried out for different source values. From Fig. 2 one may conclude that neutron albedo may be used to interpret the proton fluxes behaviour at low energies and low altitudes. At the same time, the energy spectrum of the volume source was taken in the model form. To carry out the comparative analysis of the calculation results and experimental observations this spectrum should be clarified.

CONCLUSIONS

The model and numerical calculations presented in the paper clarify the role of the pitch-angle scattering and neutron albedo for the proton distribution in the Earth plasmosphere. They demonstrate that even a small value of the pith-angle diffusion coefficient may strongly affect the proton distribution at least for small values of L and in the vicinity of the atmospheric loss cone. The modeling shows that neutron albedo may increase the proton omnidirectional flux at low energies and for low values of Mc'Ilvine parameter.

At the same time, the proposed approach was based on the assumption that proton distribution function is steady state. It is obviously that the time required for distribution function reaching to steady state is too long in comparison with the characteristic times of the solar wind variations. In this connection to obtain the reliable proton distribution function one should solve the nonstationary Fokker-Planck equation with taking into account the time variation of the proton source and Earth magnetic field geometry.

Proton volume source energy spectrum and altitude dependence affect essentially the proton fluxes, therefore, the theoretical investigations and comparison with experimental measurements are required to clarify the neutron albedo parameters.

Acknowledgements. This work was partially supported, in particular, by the National Academy of Sciences of Ukraine and Ministry for Education and Science of Ukraine.

REFERENCES

[1] *Jordanova V. K., et al.* // J. Geophys. Res.–1996.–**101**, N A1.–P. 111.

[2] *Looper M. D., et al.* // SAMPEX Observations of Energetic-Particle Albedo Over the Polar Caps.–1998, SH31B-02, sm98.

[3] *Albert J. M.* // J. Geophys. Res.–1999.–**104**, N A2.–P. 2429.

[4] *Jentsch V.* // J. Geophys. Res.–1981.–**86**, N A2.–P. 701.

[5] *Chen M. W., Lyons L. R.* // J. Geophys. Res.–1994.–**99**, N A4.–P. 5745.

[6] *Cornwall J. M.* // J. Geophys. Res.–1972.–**77**.–P. 1756.

[7] *Bashkirov V. F., et al.* // Space Res.–1998.–**36**, N 4.–P. 369.

[8] *Toivanen P. K., et al.* // J. Geophys. Res.–1999.–**104**, N A5.–P. 10205.

[9] *Cheng C. Z., Johnson J. R.* // J. Geophys. Res.–1999.–**104**, N A1.–P. 413.

[10] *Speldvik W.* // J. Geophys. Res.–1977.–**82**.–P. 2801.

THE INFLUENCE OF COSMIC RAYS ON TEMPERATURE IN LOW EARTH'S ATMOSPHERE

N. I. Lozitska[1], **V. V. Lozitsky**[2]

[1] *Astronomical Observatory, Taras Shevchenko National University*
3 Observatorna St., 04053 Kyiv-53, Ukraine
e-mail: lozitsky@aoku.freenet.kiev.ua

[2] *Taras Shevchenko National University*
6 Glushkova St., 03022 Kyiv, Ukraine

The correlation analysis shows the strong connection of the tropospheric temperature with vertical component of the geomagnetic field strength along geographical parallels. The correlation reaches –0.95 in winter on latitudes 65°–75°. The possible physical mechanism of this influence is discussed. Most likely, the falling of the ozone maximum altitude in the areas of the geomagnetic field decreasing leads to air warming near the tropopause followed by further spread of a heat to the sea level.

Until recently the connection between the temperature in the low atmosphere of the Earth and solar activity is not confirmed statistically. However, the 11-years solar cycle has been found in the indirect parameters of the atmosphere, *e.g.*, number of storms, frequency of droughts, *etc.*

We continued the research, initiated earlier by Mustel and co-authors [3], who found that after the penetration into the magnetosphere of solar corpuscular streams the region with strongest tropospheric depression was coincide with the regions of the anomalous geomagnetic field. This result adds to the observation [4] about ruptures in the tropopause by the heated stratospheric air after Forbush decreases caused by solar flares. From these results it follows that possible connection between the temperature and geomagnetic field needs a careful and detailed investigation.

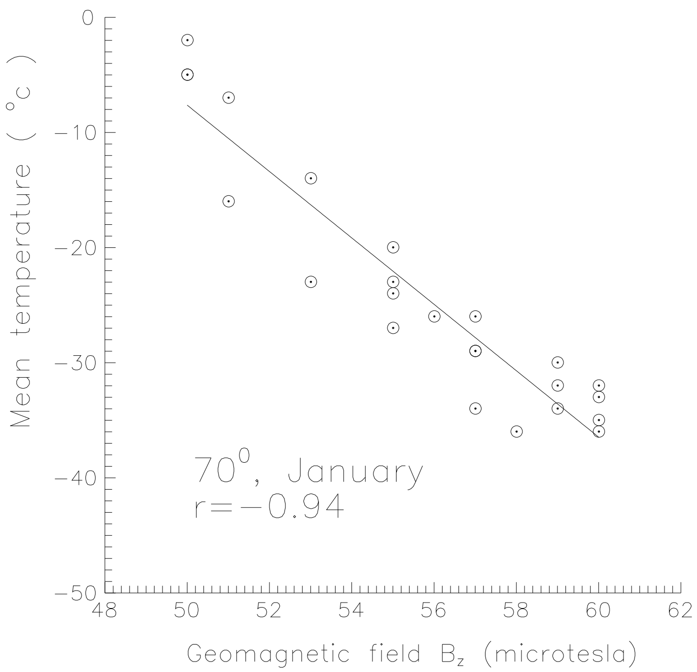

Figure 1: The regression dependence for January temperature versus geomagnetic field along 70° N latitude as an example of very strong dependence of T on B_z ($r = -0.94$)

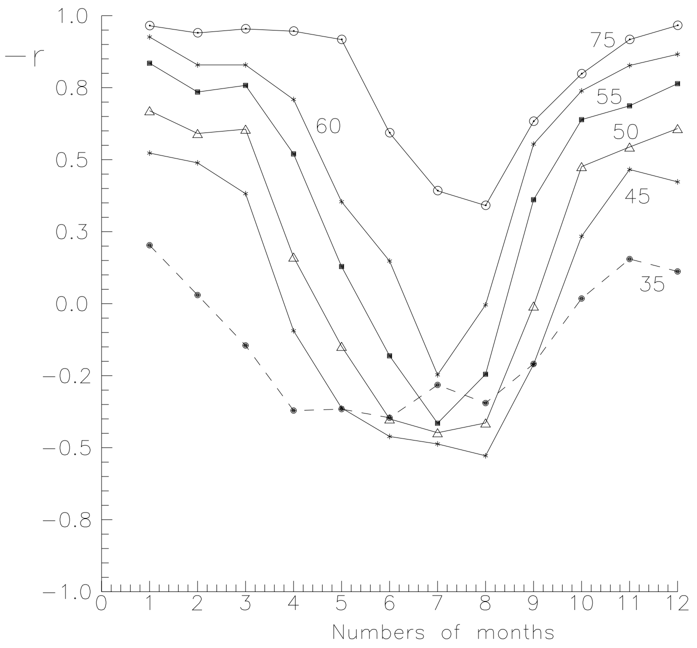

Figure 2: The correlation coefficient $r(T, B_z)$ for different north latitudes and months of a year. One can see the strong negative correlation at latitudes of 50°–75° in winter ($q \leq 0.01$) and reverse one in summer ($q \leq 0.05$)

We used the data [2] on the average monthly temperatures for 1891-1976. The magnetic field strengthes for the same period were used from [1]. Each of the geographical parallels was divided into 24 parts, and annual average values of T and B_z in 15° sections were compared to obtain the regression dependencies (Fig. 1). The same analysis was made for latitudes from 35° to 75° (Fig. 2). It was shown that the maximum of the correlation coefficient reaches –0.95 in winter on latitudes 65°–75°.

Our results confirm the following hypothesis. The solar corpuscular bursts cause the particles flow from radiation belts into the areas of minimum B_z, lowering the maximum ozone height. Stratospheric air near the tropopause is heated by ozone mechanism and heat transfered to the sea level. In summer the near-ground air masses are warmer than those arrived from the tropopause. Therefore, the correlation coefficient changes its sign.

REFERENCES

[1] *Golovkov V. P., Kolomijtzeva G. I., Konyashchenko L. P., Semyonova G. M.* The Summary of the annual mean values of magnetic elements at the world magnetic observatories // Publ. ISMIRAN, Moscow.–1983.–issue XYI.–342 p.

[2] *Gruza G. V., Ran'kova E. Y.* Data about climate structure and changeability. Air temperature at sea-level. North hemisphere.–Obninsk: GoskomHidroMet USSR, 1979.–203 p.

[3] *Markov M. N., Mustel E. R.* Space-time effects of solar terrestrial relations in the troposphere and thermosphere // Astron. Zh. AN SSSR.–1983.–**60**.–P. 417–421.

[4] *Reiter R.* Influence of Solar activity on exchange intensity between strato- and troposphere // Solar-Terrestrial Influences on Weather and Climate.–Moscow: Mir, 1982.–P. 323–332.

STABILITY OF BALLOONING MODES IN THE INNER MAGNETOSPHERE

O. S. Burdo[1], **O. K. Cheremnykh**[1], **O. P. Verkhoglyadova**[2]

[1] *Space Research Institute NASU & NSAU*
40 Acad. Glushkova Avenue, 03022 Kyiv, Ukraine

[2] *Taras Shevchenko National University*
6 Acad. Glushkova Avenue, 03022 Kyiv, Ukraine

In the present work the problem of ideal MHD pressure driven ballooning modes stability with finite compressibility plasma of the magnetosphere is studied. The set of equations described these modes is derived for the dipole model of magnetic field of the Earth. It is shown that the stability boundary of these modes is essentially affected by value and derivative of pressure. Numerical results are presented.

BASIC EQUATIONS

As starting point for formulation of problem we consider the following set of small oscillation equations

$$\rho \frac{d\vec{v}}{dt} = -\nabla\tilde{p} + \frac{1}{c}\left(\vec{j}\times\tilde{\vec{B}}\right), \quad \tilde{\vec{B}} = \mathrm{rot}\left(\vec{\xi}\times\vec{B}\right), \quad \tilde{p} = -\left(\vec{\xi}\nabla p\right) - \gamma p\,\mathrm{div}\,\vec{\xi}, \tag{1}$$

which describe arbitrary MHD perturbations of ideal compressible plasma. Here we use the generally accepted notations for all physical values. Tilde indicates the perturbed component of a corresponding value.

By taking into account the relations

$$\vec{j} = (c/4\pi)\,\mathrm{rot}\,\vec{B}, \quad \vec{v} = \partial\vec{\xi}\Big/\partial t \tag{2}$$

the system of Eqs. (1) can be reduced to the following vector equation for the displacement vector $\vec{\xi}$

$$\rho\frac{\partial^2\vec{\xi}}{\partial t^2} = \nabla\left(\vec{\xi}\cdot\nabla\right)p + \gamma\nabla\left(p\,\mathrm{div}\,\vec{\xi}\right) + \frac{1}{4\pi}\left(\mathrm{rot}\vec{B}\times\tilde{\vec{B}}\right). \tag{3}$$

The first and second right terms in this equation are important for existence of pressure driven modes.

With help of the relation

$$\vec{T} \equiv \tilde{\vec{B}} + \frac{\vec{j}\times\nabla\psi}{|\nabla\psi|^2}\left(\vec{\xi}\nabla\psi\right) = T_1\nabla\psi + T_2\frac{\vec{B}\times\nabla\psi}{|\nabla\psi|^2} - T_3\vec{B}, \tag{4}$$

$$\vec{\xi} = \xi\frac{\nabla\psi}{|\nabla\psi|^2} + \eta\frac{\vec{B}\times\nabla\psi}{\left|\vec{B}\right|^2} + \tau\frac{\vec{B}}{\left|\vec{B}\right|^2},$$

where ψ marks magnetic surfaces (see [1]), we rewrite Eq. (3) in the following useful forms

$$\frac{1}{\left|\vec{B}\right|^2|\nabla\psi|^2}\rho\frac{\partial^2\xi}{\partial t^2} = \frac{\nabla\psi\cdot\nabla T_3}{|\nabla\psi|^2} + \frac{1}{\left|\vec{B}\right|^2}\left[\frac{\nabla\psi\cdot\nabla T_0}{|\nabla\psi|^2} - 2p'T_3 + T_2\left(S-\gamma_s\right) + \vec{B}\cdot\nabla T_1 + K\xi\right], \tag{5}$$

$$\frac{|\nabla\psi|^2}{\left|\vec{B}\right|^2}\rho\frac{\partial^2\eta}{\partial t^2} = \frac{\vec{B}\times\nabla\psi}{\left|\vec{B}\right|^2}\nabla T_0 + \vec{B}\cdot\nabla T_2 + \left(\vec{B}\times\nabla\psi\right)\nabla T_3, \quad \rho\frac{\partial^2\tau}{\partial t^2} = \vec{B}\cdot\nabla T_0,$$

where the expressions T_i, S, α_s, γ_s, K and $(...)'$ are given by

$$T_1 \;=\; \frac{\vec{B}\cdot\nabla\xi}{|\nabla\psi|^2}, \quad T_2 \;=\; \frac{1}{\alpha_s}\left[\vec{B}\cdot\nabla\eta \,+\, (\gamma_s - S)\,\xi\right],$$

$$T_3 \;=\; \frac{\nabla\psi\cdot\nabla\xi}{|\nabla\psi|^2} \;+\; \frac{\vec{B}\times\nabla\psi}{\left|\vec{B}\right|^2}\nabla\eta \;+\; \frac{\xi}{\left|\vec{B}\right|^2}\left[\mathrm{div}\;(\alpha_s\,\nabla\psi) \,+\, 2\,p'\,\right], \quad S \;=\; \frac{\vec{B}\times\nabla\psi}{|\nabla\psi|^2}\,\mathrm{rot}\,\frac{\vec{B}\times\nabla\psi}{|\nabla\psi|^2}, \tag{6}$$

$$\alpha_s \;=\; \frac{\left|\vec{B}\right|^2}{|\nabla\psi|^2}, \quad \gamma_s \;=\; \frac{\vec{j}\cdot\vec{B}}{|\nabla\psi|^2}, \quad K \;=\; \frac{\alpha_s}{\gamma_s}\,(\gamma_s - S) \;+\; \frac{p\,'}{\left|\vec{B}\right|^2}\,\frac{\nabla\psi\cdot\nabla\left(2p + \left|\vec{B}\right|^2\right)}{|\nabla\psi|^2}, \quad (...)' \;\equiv\; d\,(...)/d\,\psi.$$

Eqs. (5), (6) describe the general structure of MHD perturbations and must satisfy equilibrium plasma configuration conditions.

MODEL

We consider magnetospheric plasma equilibrium

$$\nabla p \;=\; \vec{j}\times\vec{B}\Big/c \tag{7}$$

in right-handed spherical coordinate system $(r,\ \vartheta,\ \varphi)$ and use dipole model of the geomagnetic field, which can be presented in these coordinates in the form

$$\vec{B} \;=\; \nabla\varphi\times\nabla\Psi, \quad \Psi \;=\; M\,\cos^2\vartheta/r, \tag{8}$$

where M is the Earth magnetic dipole moment.

We also omit for simplicity the longitudinal current

$$\vec{j}\cdot\vec{B} \;=\; 0. \tag{9}$$

Then from condition of current closing we obtain the relation

$$\left(\vec{B}\times\nabla\psi\right)\nabla\left|\vec{B}\right| \;=\; 0. \tag{10}$$

REDUCTION OF THE EQUATIONS

To carry out the numerical calculation we reduce the Eqs. (5) as follows. At first we put in Eqs. (5)

$$\psi \;=\; \Psi, \tag{11}$$

and from Eqs. (9) and (10) we obtain

$$S \;=\; \gamma_s \;=\; 0. \tag{12}$$

Then we rewrite Eqs. (5) for ballooning perturbations

$$\frac{|\nabla\psi\cdot\nabla X|}{|\nabla\psi|^2}, \quad \frac{\left|\left(\vec{B}\times\nabla\psi\right)\cdot\nabla X\right|}{\left|\vec{B}\right|\,|\nabla\psi|} >> \frac{X}{b}, \quad \frac{\left|\vec{B}\cdot\nabla X\right|}{\left|\vec{B}\right|}, \tag{13}$$

where b is the spatial scale of problem $(b \sim R_E)$, R_E is the Earth radius, X is perturbed value.

The accurate calculations lead us to equations

$$\frac{\omega^2\rho}{|\nabla\psi|^2}\,\xi \,+\left(\vec{B}\cdot\nabla\right)\left[\frac{1}{|\nabla\psi|^2}\left(\vec{B}\cdot\nabla\right)\xi\right] \;-\; \frac{2\,r}{M\,a^2}\,(T_0 + p\,'\xi) \;=\; 0, \tag{14}$$

$$\frac{\omega^2 \left|\nabla\psi\right|^2 \rho}{\left|\vec{B}\right|^2}\,\eta + \left(\vec{B}\cdot\nabla\right)\left[\frac{\left|\nabla\psi\right|^2}{\left|\vec{B}\right|^2}\left(\vec{B}\cdot\nabla\right)\eta\right] = 0, \quad \rho\,\omega^2\tau + \vec{B}\cdot\nabla T_0 = 0,$$

where

$$T_0 = \frac{\gamma p \left|\vec{B}\right|^2}{\gamma p + \left|\vec{B}\right|^2}\left(\mathrm{div}\,\frac{\tau\vec{B}}{\left|\vec{B}\right|^2} - 2\,\vec{\kappa}\cdot\vec{\xi}\right), \quad \vec{\kappa} = \frac{\nabla\left(2p + \left|\vec{B}\right|^2\right)}{2\left|\vec{B}\right|^2} - \frac{\vec{B}}{\left|\vec{B}\right|^4}\left(\vec{B}\cdot\nabla\right)\frac{\left|\vec{B}\right|^2}{2}. \tag{15}$$

This system describes the coupled poloidal shear Alfvén and magnetosonic modes (the first and last equations) and the toroidal shear Alfvén modes (the second equation).

In terms of the dimensionless variables

$$\omega \to \omega/\omega_A = \Omega, \quad \left|\vec{B}\right| \to \left|\vec{B}\right|\big/B_0, \quad \psi \to \psi/\psi_0, \quad p \to p/B_0^2, \tag{16}$$

where

$$B_0 = M/L^3, \quad \psi_0 = M/L, \quad \omega_A = B_0/(L\sqrt{\rho}),$$

and with help of the relations

$$\left(\vec{B}\cdot\nabla\right) = \frac{M}{L^4\cos^7\vartheta}\,\frac{\partial}{\partial\vartheta}, \quad \left|\nabla\psi\right| = \frac{M\sqrt{a(\vartheta)}}{L^2\cos^2\vartheta}, \quad a(\vartheta) = 1 + 3\sin^2\vartheta,$$

which describe the step of going to the derivatives along the magnetic field line, the Eqs. (14) can be presented in the dimensionless form [2]

$$\Omega^2\xi + \frac{a(\vartheta)}{\cos^{13}\vartheta}\,\frac{\partial}{\partial\vartheta}\left[\frac{1}{a(\vartheta)\cos\vartheta}\,\frac{\partial\xi}{\partial\vartheta}\right] - \frac{4}{a(\vartheta)\cos^4\vartheta}\left(T_0 - \frac{\alpha\beta}{\gamma}\,\xi\right) = 0,$$

$$\Omega^2\eta + \frac{1}{\cos^{13}\vartheta}\,\frac{\partial}{\partial\vartheta}\left(\frac{1}{\cos\vartheta}\,\frac{\partial\eta}{\partial\vartheta}\right) = 0, \quad \Omega^2\tau + \frac{1}{\cos^7\vartheta}\,\frac{\partial T_0}{\partial\vartheta} = 0, \tag{17}$$

where

$$T_0 = \frac{\beta\left|\vec{B}\right|^2}{\beta + \left|\vec{B}\right|^2}\left[\frac{1}{\cos^7\vartheta}\,\frac{\partial}{\partial\vartheta}\left(\frac{\tau\cos^{12}\vartheta}{a(\vartheta)}\right) - \frac{4\cos^2\vartheta}{a^2(\vartheta)}\,\xi\right], \quad \alpha = -\frac{L}{p}\,\frac{dp}{dL}, \quad \beta = \frac{\gamma p}{B_0^2}. \tag{18}$$

The Eqs. (17) together with the first kind boundary conditions (Dirichlet) corresponding to the fixed magnetic line ends at the perfectly conducting ionosphere fully describe the ballooning modes eigenfrequency spectrum.

STABILITY BOUNDARY

The spectrum of Eqs. (17) for case of "cold" plasma ($\beta = 0$) was analysed previously [3]–[5]. Now we consider the stability of ballooning mode ($\beta > 0$), which can come into existence first of all in the radiation belts. The second of the Eqs. (17), for the perturbation $\eta(\vartheta)$, under the first kind boundary conditions, has a positive spectrum and can not introduce any instability. Therefore, for the needs of stability problem solving, it is necessary to investigate the eigenvalue problem for the other Eqs. (17), namely for perturbations $\xi(\vartheta)$ and $\tau(\vartheta)$, with the same boundary conditions. The stability boundary is determined by the equality $\Omega^2_{min} = 0$, where Ω^2_{min} is the lowest eigenvalue. The equation $\Omega^2_{min}(\alpha, \beta) = 0$ was solved numerically. Stability region for these perturbations in (α, β) plane is shown in Fig. 1. The set of curves for various geomagnetic latitude values ϑ_0 varying from 5° (upper right curve) over 15°, 30°, 45° till 72° (lower left one) is presented. The qualitative estimation $\alpha\beta\,\sin^2\vartheta_0 \sim 1$ for these curves takes place. It should be noted that all the eigenfunctions obtained are strongly ϑ-dependent, so the flute eigenmodes are absent in our case of the Dirichlet boundary conditions.

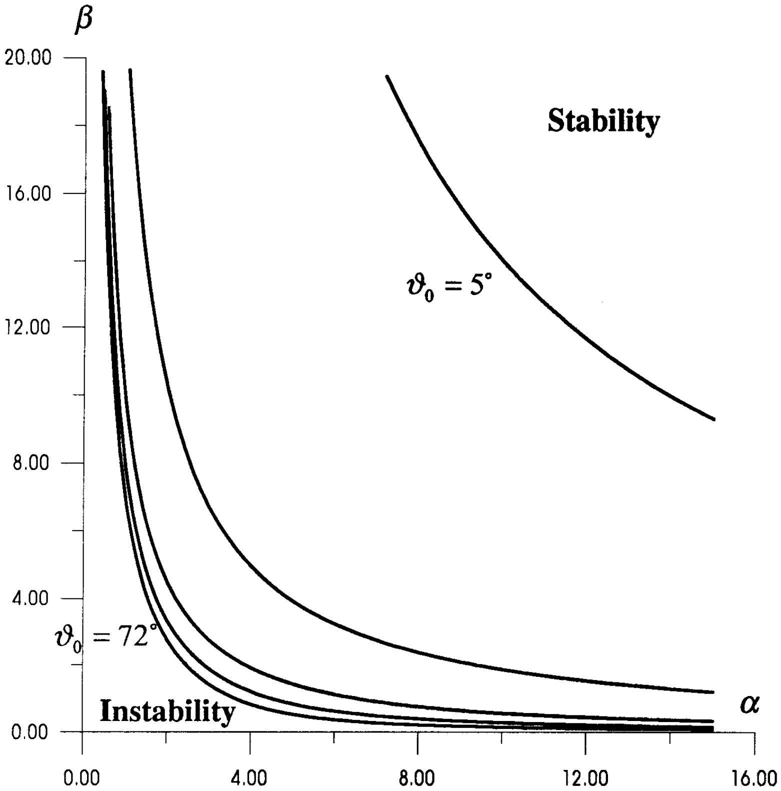

Figure 1: Stability boundaries in the (α, β) plane for different values of geomagnetic latitude ϑ_0 indicating field line ends on the ionosphere

THE MAIN RESULTS

– The system of Eqs. (5), which describes the pressure driven waves in the arbitrary magnetic field, was obtained.

– These equations are reduced to a set of scalar partial differential Eqs. (17)–(18) for ballooning modes in the dipole model of the geomagnetic field.

– The stability region of ballooning modes is obtained.

Acknowledgements. This work was partially supported by the theme 0197U015786 of the National Academy of Sciences of Ukraine and Ministry for Education and Science of Ukraine.

REFERENCES

[1] *Pustovitov V. D., Shafranov V. D.* Reviews of Plasma Physics / Ed. B. B. Kadomtsev.–New York: Consultants Bureau, 1990.–**15**.–P. 163.

[2] *Burdo O. S., Cheremnykh O. K., Verkhoglyadova O. P.* // Izvestiya Akad. Nauk. Ser. Fizicheskaya.–2000.–**64**, N 9b.–P. 1897. (in Russian).

[3] *Burdo O. S., Cheremnykh O. K., Verkhoglyadova O. P.* // Proc. Intern. Symp. "From solar corona through interplanetary space, into Earth's magnetosphere and ionosphere: Interball, ISTP satellites, and ground-based observation".–Kyiv, 2000.–P. 97.

[4] *Chen L., Hasegava A.* // J. Geophys. Res.–1974.–**79**.–P. 1024.

[5] *Cheng C. Z., Chang T. C., Lin C. A., Tsai W. H.* // J. Geophys. Res.–1993.-**18**.–P. 11339.

WAVE PROCESSES, GLOBAL– AND LARGE–SCALE DISTURBANCES IN THE NEAR–EARTH PLASMA

L. F. Chernogor and V. T. Rozumenko

Department of Space Radio Physics, V. Karazin Kharkiv National University
4 Svoboda Square, 61077 Kharkiv, Ukraine
e-mail: Leonid.F.Chernogor@univer.kharkov.ua

INTRODUCTION

Particular attention has been recently paid to physical processes originating in geospace from natural and anthropogenic sources of energy (see CEDAR and Space Weather Plan). Results from these investigations contributed enormously to understanding of how different geospheres are coupled, or, in other words, how the lithosphere, atmosphere, ionosphere, and magnetosphere exchange mass, momentum, energy, and information. This means that geospace is an open nonlinear system, and the mechanisms for coupling the above subsystems are studied insufficiently. The coupling processes include linear and nonlinear waves, and the aim of this study is to determine the apparent velocities of the perturbations, using observations, and to find out the types of waves responsible for perturbation propagation.

MODEL SPECIFICATIONS AND CALCULATIONS

Detailed calculations of energetics during disturbances on the sun, in the magnetosphere, ionosphere, atmosphere, and lithosphere have been made (Chernogor, 1998). The starting point for the development of the model is the following: the intensity of solar emissions in the ultraviolet, gamma ray, soft, and hard X-ray wavelengths, as well as solar wind characteristics under quiet and disturbed conditions. For the magnetosphere, the following parameters have been obtained: geomagnetic micropulsation energy, plasma thermal energy, nonthermal particle energy, geomagnetic storm power and energy, energy of the electric fields of magnetospheric origin. The energetics of the ionosphere is estimated taking into account the power and energy inputs from the sun, the plasma thermal particles, and the winds at ionospheric heights, electric currents, particle precipitation at high and middle latitudes. The energetics of the atmosphere is suggested to be determined by the balance between energy inputs and outputs, and by processes in the medium. The latter include thermal motion, the moving solar terminators, winds, large- and small-scale turbulence, atmospheric electricity, the entries of large space bodies into the atmosphere, *etc.* The energetics of seismic processes includes the potential and elastic energy in the lithosphere, the energy and power of volcanic processes and tsunami. The energetics of earthquake acoustic, electric, and magnetic effects on the near-earth environment is separately studied. Estimates of the energy of optical, radon, and other emissions produced by earthquakes are made. Particular attention is given to the energetics of such anthropogenic effects as explosions, space vehicle launches and re-entries into the earth's atmosphere, beams of particles and plasma, high-power radio transmissions, harmonics in the kHz range radiated by electrical power transmission lines, MHD generators, and meteotrons.

The estimates made suggest that energy deposition into the environment from various natural and anthropogenic processes can be significant. Energy estimates are just the first stage in estimating the detectability of the effects of a particular disturbance. Further, it is necessary to make comparisons between specific characteristics of the signal and noise (interference). These may include the energy or power of the process per unit volume. Because the process under study is spatially and time discrete, its specific characteristics relatively increase. Moreover, it is necessary to take into account that the source of energy, say a cyclone, may not cause significant ionospheric or magnetospheric disturbances, and the conversion factors can significantly differ depending on the nature of the energy of the disturbance, the coordinates and the timing of energy release, and the condition in the system and its subsystems, although it is sure enough that there are feedbacks in the near-earth system, which is sometimes called geospace sphere consisting of the well-known geospheres: the lithosphere, the atmosphere, the ionosphere, the magnetosphere, *etc.* On the other hand, the system, and, moreover, the subsystems, are open systems, and, therefore, a release of energy may be triggered. For instance, E-region heating by relatively low-energy HF amplitude-modulated waves changes the ionospheric (direct current) conductivity, which results in modulating the strength of high-energy electric currents in space. Particle precipitation from the magnetosphere triggered by a low-energy source can significantly change the energetics of the lower ionosphere ($\sim 50-100$ km) as well (Chernogor *et al.*, 1998).

The nomenclature of manifestations of the triggering mechanism may be continued. The variations in parameters of the near-earth medium caused by different disturbances in principle differ a little. To detect the display of a particular disturbance, the variations in parameters of the medium caused by different disturbances should undergo an in-depth examination by a cluster of independent methods, and mathematical models of the signal and interference should be developed. Only after this, the problem of disturbance detection can be set and practically solved.

MECHANISMS OF THE PERTURBATIONS TRANSFER AT LARGE– AND GLOBAL–SCALE DISTANCES

Possible causative mechanisms for the transfer of perturbation at large- and global-scale distances from a localized ionospheric disturbance have been analyzed in order to identify the role of various physical processes. Acoustic (infrasound) waves (Gossard and Hooke, 1975; Francis, 1975; Chernogor, 1997), MHD waves (Jacobs, 1970; Guglielmi and Pokhotelov, 1996; Kelley, 1989), slow MHD waves (Sorokin and Fedorovich, 1982), gyrotropic waves (Sorokin and Fedorovich, 1982; Sorokin, 1986; Sorokin, 1987), seismic waves (Pasechnik, 1970), as well as nonlinear waves (Whitman, 1974; Nonlinear waves, 1974; Scott, 1970; Lamb, 1980; Petviashvili and Pokhotelov, 1992; Guglielmi and Pokhotelov, 1996; Pokhotelov *et al.*, 1996; Gurevich, 1978) and structures are considered to be important processes in transferring perturbations from discrete disturbances to sites at global-scale distances. The data on observations of perturbations at global-scale distances from initial disturbances exhibit several groups of propagation speeds of $\sim 0.3-0.8$ km/s, $2-3$ km/s, $3-5$ km/s, and $10-100$ km/s. They correspond to different types of waves which we have analyzed in detail.

CONCLUSIONS

1. The lithosphere, atmosphere, ionosphere, and magnetosphere are a single open system. Energy is incoming into the system from the sun and space. The exchange of energy, matter, and governing influences takes place between the subsystems; feedbacks through the system appear at different directions.
2. Estimates of the energetics of the solar processes affecting the earth, as well as of the main processes in the lithosphere-atmosphere-ionosphere-magnetosphere system, are made.
3. Estimates of the energetics of a few processes linking the subsystems (disturbances in the geomagnetic and geoelectric fields, ionospheric electric currents, winds, turbulence, energetic particle fluxes, *etc.*) are made.
4. Perturbations in the near-earth medium are transferred via acoustic waves ($v \sim 0.3-0.7$ km/s), slow MHD waves ($v \sim 1-10$ km/s), seismic waves ($v \sim 3-8$ km/s), gyrotropic waves ($v \sim 10-8\times10^2$ km/s), and MHD waves ($v \sim 10^3$ km/s). The role of nonlinear waves is to be studied.

Acknowledgements. The study has been supported by Science and Technology Center in Ukraine, Grants 1772 and 1773.

REFERENCES

[1] Coupling, energetic and dynamics of atmospheric regions, CEDAR Phase III. Executive summary. Bolder, CO: Philip Tobias Enterprises, 1996.–40 p.

[2] *Chernogor L. F.* Energetics of Processes on the Earth, in the Atmosphere, and Space // Space Science and Technology.–1998.–**4**, N 1.–P. 10. (in Russian)

[3] *Chernogor L. F.* Infrasound effects of earthquakes and their precursors on parameters of near-earth space // Radio Physics and Radio Astronomy.–1997.–**2**.–P. 463–472. (in Russian).

[4] *Chernogor L. F., Garmash K. P., Rozumenko V. T.* Flux parameters of energetic particles affecting the middle latitude lower ionosphere // Radio Physics and Radio Astronomy.–1998.–**3**.–P. 191–197.

[5] *Davies K.* Ionospheric Radio.–London: Peter Peregrinus Ltd., 1990.–XX.–580 p.

[6] *Francis S. N.* Global propagation of atmospheric gravity waves: a review // J. Atmos. Terr. Phys.–1975.–**37**.–P. 1011.

[7] *Garmash K. P., Gokov A. M. , Kostrov L. S., Rozumenko V. T., Tyrnov O. F., Fedorenko Yu. P., Tsymbal A. M., Chernogor L. F.* Radio Wave investigations and modeling the processes in the ionosphere disturbed by sources of various nature. 1. Instrumentation and processes in the naturally disturbed ionosphere // Bull. Kharkiv State Univ. Radio Physics and Electronics.–1998.–N 405.–P. 157–176. (in Russian).

[8] *Gossard E. E., Hooke W. H.* Waves in the Atmosphere.–New York: Elsevier Publishing Co., Inc., 1975.

[9] *Gubkin K. E.* The propagation of waves from explosions // Mechanics in the USSR during 50 years, Moscow, Nauka, 1970.–**2**.–P. 269–311. (in Russian).

[10] *Guglielmi A. V., Pokhotelov O. A.* Geoelectomagnetic waves.–Bristol: Adam Hilger, 1996.

[11] *Gurevich A. V.* Nonlinear phenomena in the ionosphere.–N. Y.: Springer Verlag, 1978.–360 p.

[12] *Jacobs J. A.* Geomagnetic micropulsations.–Berlin: Springer-Verlag, 1970.

[13] *Kalitkin N. N.* Numerical Methods.–Moscow: Nauka, 1978.–512 p.

[14] *Kelley M. C.* The Earth's ionosphere: Plasma physics and electrodynamics.–San Diego, Calif.: Academic Press, 1989.–487 p.

[15] *Lamb G. L. Jr.* Elements of soliton theory.–New York – Chichester – Brisbane – Toronto: Wiley – Interscience Publ. John Wiley & Sons, 1980.

[16] Nonlinear waves / Eds S. Leibovich and A. K. Scebass.–CUP, Ithaka and London, 1974.

[17] *Pasechnik I. P.* The behavior of seismic waves during nuclear explosions and earthquakes.–Moscow: Nauka, 1970.–193 p. (in Russian).

[18] *Petviashvili V. I., Pokhotelov O. A.* Solitary waves in plasmas and the atmosphere.–London-Reading: Gordon and Breach, 1992.

[19] *Pokhotelov O. A., Stenfo L., Shukla P. K.* Nonlinear structures in the magnetosphere and ionosphere // Plasma Physics.–1996.–**22**.–P. 941–953. (in Russian)

[20] *Scott A.* Active and nonlinear wave propagation in electronics.–N. Y., London, Sidney, Toronto: Wiley – Interscience Publ. John Wiley & Sons, 1970.

[21] *Sorokin V. M.* Midlatitudinal long-period geomagnetic oscillations and their relation to wave disturbances in the ionosphere // Geomagnetism and Aeronomy.–1987.–**27**.–P. 104–108. (in Russian).

[22] *Sorokin V. M.* On the role of the ionosphere in geomagnetic pulsation propagation // Geomagnetism and Aeronomy.–1986.–**26**.–P. 640–646. (in Russian).

[23] *Sorokin V. M., Fedorovich G. V.* Physics of Slow MHD Waves in the Ionospheric Plasma.–Moscow: Energoatomizdat, 1982.–136 p. (in Russian).

[24] Space Weather Plan. National Space Weather Program. Implementation Plan. Draft 5/13/96

[25] *Whitman G. B.* Linear and nonlinear waves.–N. Y., London, Sidney, Toronto: Wiley-Interscience Publ. John Wiley & Sons, 1974.